Effects of Impurity Doping at ppm Level in Organic Semiconductors

OHASHI CHIKA

Doctor of Philosophy

Department of Functional Molecular Science
School of Physical Sciences
SOKENDAI (The Graduate University for Advanced Studies)

Effects of Impurity Doping at ppm Level in Organic Semiconductors

Chika Ohashi

SOKENDAI (The Graduate University for Advanced Studies)

School of Physical Sciences

Dept. of Functional Molecular Science

Preface

The author carried out the experiments and wrote the doctoral thesis under the guidance of Professor Masahiro Hiramoto at Department of Functional Molecular Science, School of Physical Sciences, SOKENDAI. This thesis indicates the effects of impurity doping at ppm level in organic semiconductors.

The author believes that the work described in this thesis will lead to the clarification of detailed doping mechanism and the new types of organic device using doped organic single crystals.

Chika Ohashi

Dept. of Functional Molecular Science

School of Physical Sciences

SOKENDAI

10th January 2017

Contents

Chapter 1: General Introduction 1

1.1. Background to Inorganic Semiconductors 1

1.2. Introduction to Organic Semiconductors 3

1.2.1 History 3

1.2.2 Materials 4

1.2.2.1 Organic Semiconductors 4

1.2.2.2 Dopants 6

1.3. Impurity Doping for Organic Semiconductor 7

1.3.1 Control of Carrier Concentration 7

1.3.2 Mechanism of Impurity Doping 8

1.3.3 Doped Organic Photovoltaic Cells 11

1.4. Measurement Techniques for Doped Organic Semiconductors 13

1.4.1. Energy Band Mapping 13

1.4.2. Hall effect Measurements 15

1.4.3. Organic Field-Effect Transistors 17

1.4.4. Organic Photovoltaic Cells 19

1.5. Motivation for This Doctoral Thesis 21

1.6. Overview for This Doctoral Thesis 22

1.7. References 25

Chapter 2: Experimental Equipment and Methods 29

2.1. Purification of Organic Semiconductors 29

2.2. Extremely Low Concentration Doping for Organic Semiconductors 31
2.3. Measurements of Doped Organic Semiconductors 34
2.3.1. Hall effect Measurements 34
2.3.2. Kelvin Probe Measurements 36
2.3.3. Organic Field-Effect Transistors 38
2.3.4. Organic Photovoltaic Cells 39
2.3.5. Thin-film Structures 42
2.4. References 44

Chapter 3: Hall effects for Doped Organic Single Crystals 46
3.1. Introduction 47
3.2. Experimental 49
3.2.1. Homoepitaxial Cells 49
3.2.2. Hall effect Measurements 50
3.2.3. Single Crystal Doping 51
3.3. Results and Discussion 52
3.3.1. Doped Homoepitaxial Layer 52
3.3.2. Hall Signal 54
3.3.3. Hole Concentration and Hall Mobility 59
3.3.4. AFM and GIXD for Doped Single Crystals 62
3.3.5. Contact Size Effect 65
3.3.6 Doped Amorphous Films 68
3.4. Conclusion 70
3.5. References 71

Chapter 4: Field-Effect Mobility of Doped Organic Single Crystals 74
4.1. Introduction 75
4.2. Experimental 76
4.3. Results and Discussion 78
4.3.1. FET Characteristics 78
4.3.2. Activation Energy of Hole Traps 80
4.3.3. Concentration of Hole Traps 83
4.4. Conclusion 88
4.5. References 89

Chapter 5: Effects of Impurity Doping in Simple $n^{+}p$-Homojunction Organic Photovoltaic Cells 91
5.1. Introduction 92
5.2. Experimental 93
5.3. Results and Discussion 95
5.3.1. Formation of $n^{+}p$-homojunction 95
5.3.2. Photovoltaic Characteristics 97
5.3.3. Energy Structures 99
5.3.4. Doping Concentration Dependence of Photovoltaic Characteristics 102
5.4. Conclusion 106
5.5. References 107

Chapter 6: Summary and Future Prospects 110

List of Publications 111

Acknowledgement 115

Chapter 1:

General Introduction

1.1. Background to Inorganic Semiconductors

Inorganic semiconductors such as silicon (Si), germanium (Ge), and gallium nitride (GaN), etc. have been part of our daily lives since the middle of the 20th century. One of the most familiar semiconductor devices is the blue light-emitting diode (LED) (Fig. 1.1(a)).[1] Three Japanese researchers (I. Akasaki, H. Amano, and S. Nakamura) were awarded the Nobel Prize in 2014 for their work on developing efficient blue light LEDs. Impurity doping is essential in order to fabricate the various semiconductor devices such as LEDs, transistors and solar cells, etc. The material to be doped is a highly purified inorganic semiconductor material grown by the Czochralski (CZ) method with which crystals with a purity of eleven nines (11N) (99.999999999%) are produced.[2] In intrinsic (i-) type material, the hole and electron concentrations are equal. Impurity dopants are introduced into the inorganic semiconductor lattice by ion implantation.

For example, in the case of silicon (Si), boron (B) and phosphorus (P) are used for acceptor and donor dopants, respectively. When ionized boron (B^-) is introduced into the Si lattice, free holes (h^+) are created (Fig. 1.1(b)). In B-doped Si the hole concentration increases and the Si changes from i-type to positive (*p*-) type. On the other hand, when ionized phosphorus (P^+) is introduced into the Si lattice, free electrons (e^-) are created (Fig. 1.1(c)). In P-doped Si the electron concentration increases and changes the Si from i-type to negative (*n*-) type. Controlling the doping in inorganic

semiconductors has become well established. However, this technique has a high cost due to the use of thermal processes in excess of 1000 °C.[2] Thus, new materials need to be developed in order to reduce cost and also reduce the impact on the environment.

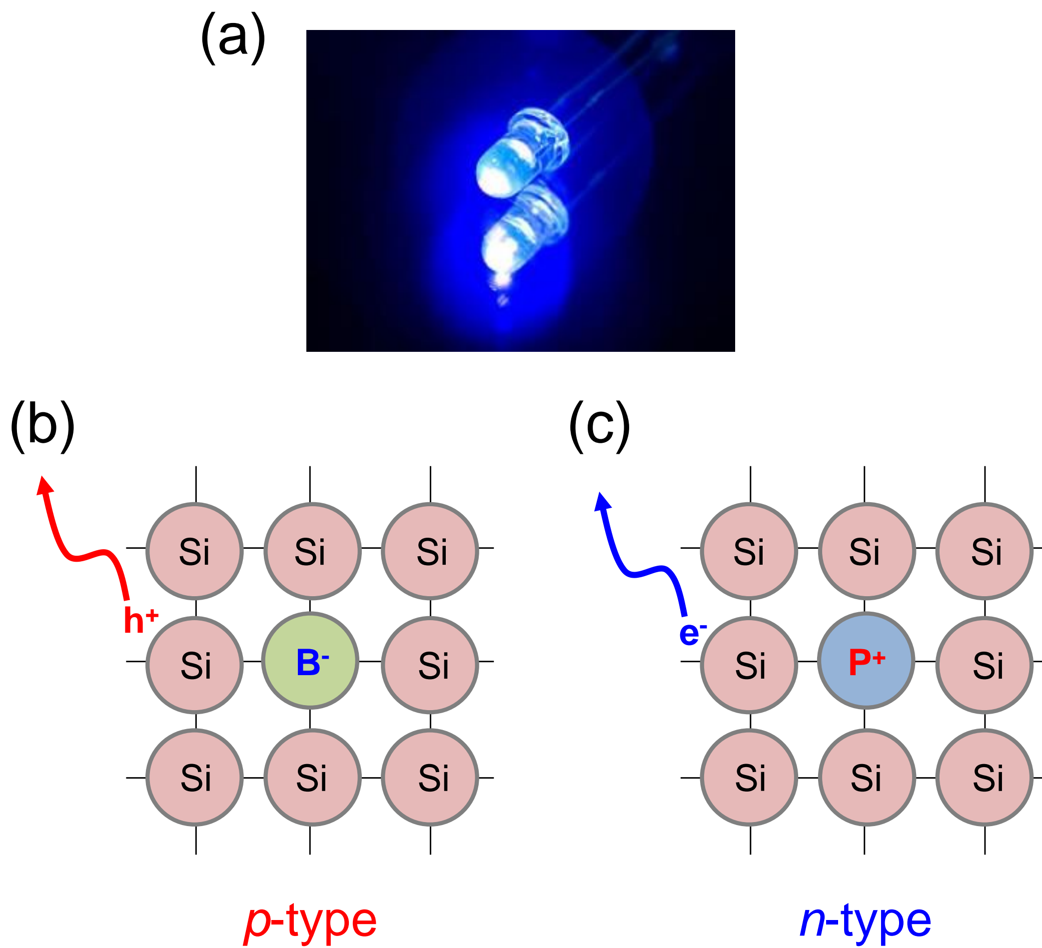

Fig. 1.1 (a) Photograph of a blue LED. Schematic illustrations of (b) B-doped and (c) P-doped Si.

1.2. Introduction to Organic Semiconductors

1.2.1. History

In 1954, H. Akamatsu and H. Inokuchi successfully measured the conductivity (σ) of the perylene-bromine complex for the first time.[3) In the 1980s, Tang et al. reported on an organic LED (OLED)[4) and organic photovoltaic cell (OPV)[5). Kudo et al. also reported on an organic field-effect transistor (OFET).[6) Since then, organic semiconductors have been studied for device applications. Organic semiconductors have a number of benefits. Firstly, they are low cost. Other potential benefits are that they are both flexible and printable, since the molecules are aggregated by low intermolecular interactions based on Van der Waals forces.[7) The Sony Corporation demonstrated the first example of a flexible display using OLEDs in 2007 (Fig. 1.2.1).[8) In addition, to control the carrier concentration (N), impurity doping is the standard technique.[9,10) However, the range of applications has been still limited to cellular phone and television. Recently, organic single crystals possessing band transport have been discovered (see chapter 1.2.2.1). They have a potential to provide the new types of organic device in our daily life. Thus, a precise impurity doping technique must be developed in order to fabricate the doped organic single crystals.

Fig. 1.2.1 Photograph of flexible display using an OLED.

1.2.2. Materials

1.2.2.1. Organic Semiconductors

Fig. 1.2.2.1 shows organic semiconductor materials used in this doctoral thesis. Rubrene (Fig. 1.2.2.1(a)) single crystals used in chapters 3 and 4 exhibit the band transport similar to inorganic semiconductors.[11-13] In the case of band transport, the carriers are delocalized in the molecules. The carrier mobility (μ) for band transport can be expressed by the following equations.[14]

$$\mu = \frac{e\tau_c}{m^*} \qquad (1.2.2.1.1)$$

$$\frac{1}{\tau_c} = \frac{1}{\tau_L} + \frac{1}{\tau_I} \qquad (1.2.2.1.2)$$

where τ_c is the mean free time, e is the elementary charge, and m^* is the effective mass. τ_L and τ_I are the mean free times for lattice scattering and impurity scattering, respectively. As the temperature increases, lattice scattering increases and μ decreases. τ_L is proportional to temperature raised to the power of minus three halves ($\tau_L \propto T^{-3/2}$). On the other hand, as the temperature decreases, the impurity scattering increases and μ decreases. τ_I is proportional to temperature raised to the power of three halves ($\tau_I \propto T^{3/2}$).

α-sexithiophene (6T)[15] (Fig. 1.2.2.1(b)) and fullerene (C_{60})[16] (Fig. 1.2.2.1(c)) used in chapter 5 exhibit the hopping transport. In the case of hopping transport, the carriers are localized in the molecule. μ for hopping transport can be expressed by the following equation:

$$\mu = \mu_0 \exp\left(-\frac{E_a}{kT}\right) \qquad (1.2.2.1.3)$$

Here, μ_0 is the intrinsic mobility, E_a is the activation energy, k is the Boltzmann constant and T is the temperature. As the temperature increases, μ is thermally activated and increases. This means that the temperature dependence of μ is strongly different between band transport and hopping transport.

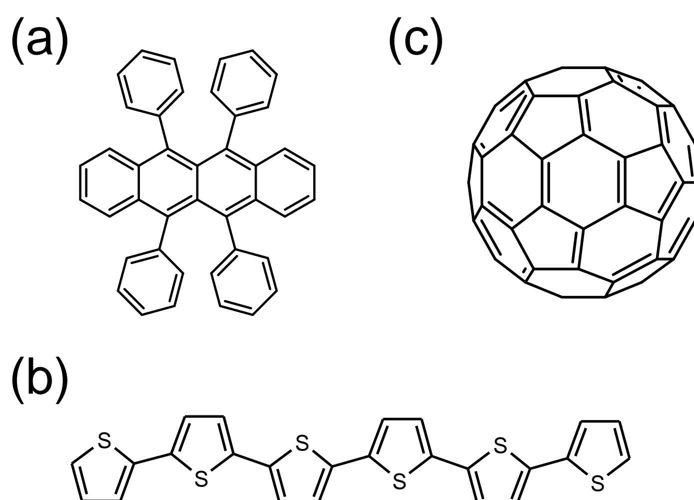

Fig. 1.2.2.1 Organic semiconductor materials used in this doctoral thesis. (a) Rubrene, (b) α-sexithiophene (6T), and (c) fullerene (C_{60}).

1.2.2.2. Dopants

Table 1.2.2.2 shows the dopant materials used for organic semiconductors.[3,17-31] In order to reduce the driving voltage, the interfacial layer between the electrodes and the organic semiconductors is doped. Yang et al. reported on using cesium carbonate (Cs_2O_3) as a donor dopant.[30,31] Cs_2CO_3 can donate an electron to the organic semiconductor due to its low work function (3.0 eV). On the other hand, Endo et al. reported on iron(III) chloride ($FeCl_3$) as an acceptor dopant (Fig. 1.2.2.2).[23,24] $FeCl_3$ can withdraw an electron from the organic semiconductor due to its high work function (5.5 eV). In early studies, halogens[3] etc. were used for the dopants. However, these dopants are difficult to handle due to them being unstable in air. Thus, irrespective of the acceptor or donor used, air-stable inorganic and organic compounds have been used.

Table 1.2.2.2 Dopant materials for organic semiconductors.

	Accepter dopant		Donor dopant
Halogen	Br_2[3], I_2[17]	Alkali metal	Li[25], Na[26], K[27]
Organic compound	TCNQ[18], DDQ[19], $C_{60}F_{36}$[20]	Alkali earth metal	Mg[28], Ca[29]
Inorganic compound	MoO_3[21], V_2O_5[22], $FeCl_3$[23,24]	Inorganic compound	Cs_2CO_3[30,31]

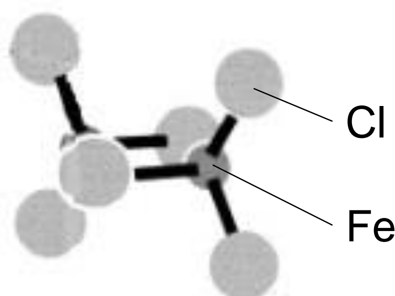

Fig. 1.2.2.2 Illustration of three-dimensional molecular structure of Fe_2Cl_6.[24]

1.3. Impurity Doping for Organic Semiconductor

1.3.1. Control of Carrier Concentration

Impurity doping is an important technique to enhance the carrier concentration (N) and the Fermi energy (E_F). In accepter-doped organic semiconductors the hole concentration increase and the organic semiconductors change from i-type to *p*-type. On the other hand, in donor-doped organic semiconductors the electron concentration increase and the organic semiconductors change from i-type to *n*- type. However, the essential properties of organic semiconductors have been limited by the low purity. For example, undoped phthalocyanine (H_2Pc) exhibited *p*-type characteristics because oxygen (O_2) from the air acted as an acceptor dopant. Thus, organic semiconductors need to be prevented from exposure to air at any time by using nitrogen (N_2) glove box. In this work, in order to purify the organic semiconductors, the physical vapor transport method was used (see chapter 2.1), and impurity doping was performed by a 'multi-component co-evaporation' technique (see chapter 2.2).

Previously, a crude determination of the carrier type of organic semiconductors was made from the ease with which carriers could be injected[32-34)] or the value of carrier mobility (μ)[35)]. However, more recently, the standard technique used to measure the values of N and E_F of doped organic semiconductors utilizes a Kelvin probe in our group (see chapter 1.4.1). So, the author precisely determined the carrier type by using the carrier concentration (N). This measurement is employed in chapters 3 and 5.

1.3.2. Mechanism of Impurity Doping

Fig. 1.3.2(a) shows schematic energy diagrams of cceptor and donor doped organic semiconductor. In the case of acceptor doping, the lowest unoccupied molecular orbital (LUMO) level of the dopant (red solid line) needs to be located below the highest occupied molecular orbital (HOMO) level of the organic semiconductor. The acceptor can withdraw an electron from the HOMO level of the organic semiconductor (black solid curve). On the other hand, in the case of donor doping, the HOMO level of the dopant (blue solid line) needs to be located above the LUMO level of the organic semiconductor. The donor can donate an electron to the LUMO level of the organic semiconductor (black solid curve). Thus, charge transport (CT) between the dopant and the organic semiconductor occurs due to the impurity doping.

Kubo et al. has confirmed that CT complexes form between fullerene (C_{60}) and various dopants.[36,37] It was found that two types of CT complex, i.e., C_{60}^{+}--- MoO_3^{-} and C_{60}^{-}--- $Cs_2CO_3^{+}$, were formed in C_{60} films with acceptor (MoO_3) and donor (Cs_2CO_3) dopants (Figs. 1.3.2(b) and (c)). These doped C_{60} films exhibited color changes and CT absorption. In addition, in the case of MoO_3 doping, the Fermi energy (E_F) shifted to the HOMO level. This suggests that the MoO_3-doped C_{60} film was *p*-type. On the other hand, in the case of Cs_2CO_3 doping, E_F shifted to the LUMO level, suggesting that the Cs_2CO_3-doped C_{60} film was *n*-type. Recently, Hiramoto et al. has reported on similar shifts in E_F for various organic semiconductor films with impurity doping at a concentration of 3000 ppm.[9] Thus, the mechanism of impurity doping can be explained by the CT model.

Moreover, the doping efficiency (I) can be calculated as the ratio of the number of carriers ($N_{free\ carrier}$) created to that of the dopant molecule (N_{dopant}) by the following equation.

$$I = \frac{N_{free\,carrier}}{N_{dopant}} \qquad (1.3.2.1)$$

In the case of inorganic semiconductors, due to the high permittivity such as 12[2], the doping efficiency reached 100%. However, in the case of organic semiconductors, due to the low permittivity such as 4[9], the doping efficiency was below 10% (Table. 1.3.2)[39] and must be increased to 100%.

Table. 1.3.2 Doping efficiency for organic semiconductors

	H_2Pc	C_{60}
Accepter doping ($FeCl_3$)	2	0.2
Donor doping (Cs_2CO_3)	10	10

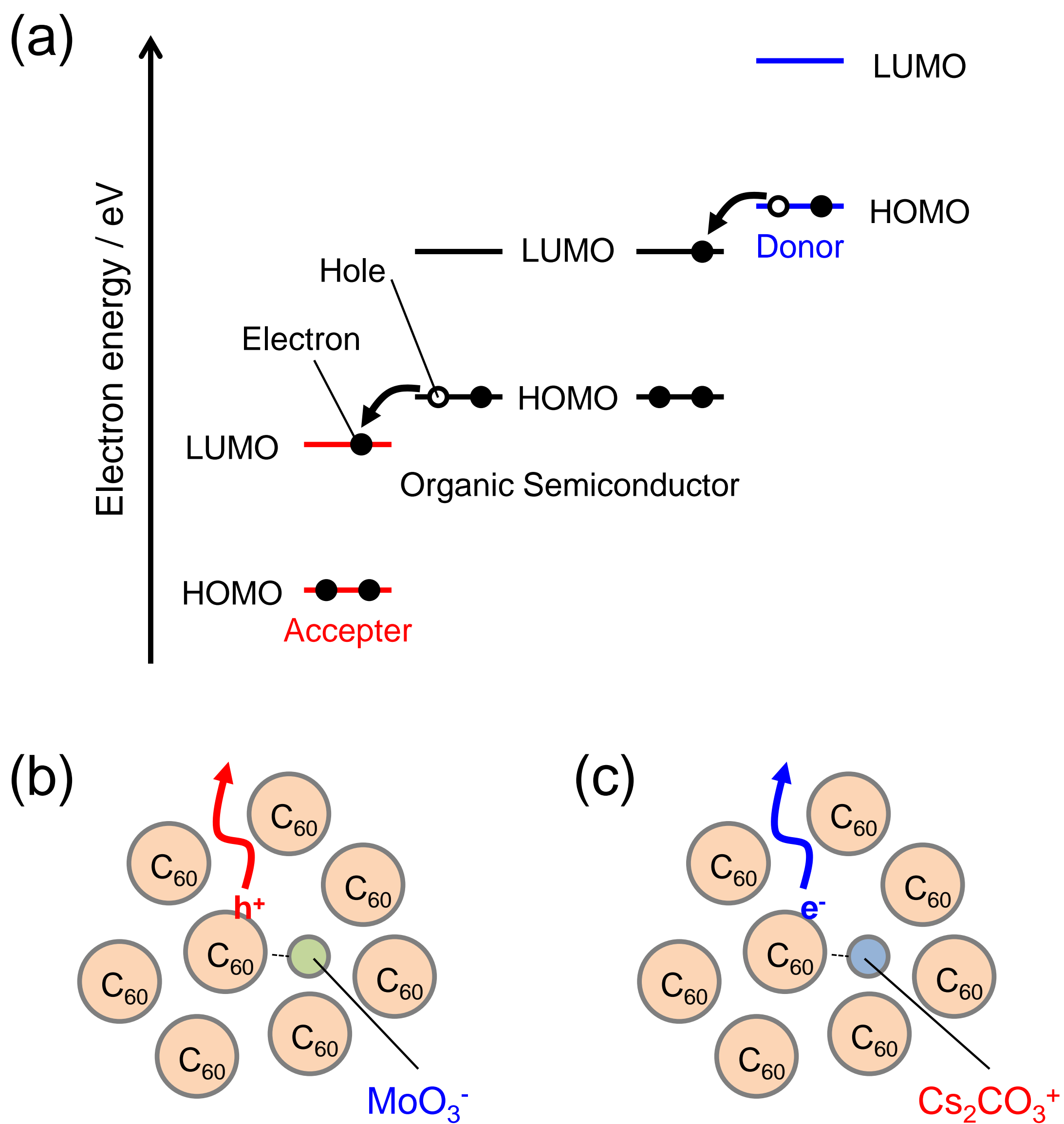

Fig. 1.3.2 (a) Schematic energy band diagram of acceptor and donor doping in organic semiconductor. Schematic illustrations of (b) MoO_3-doped and (c) Cs_2CO_3-doped C_{60} films.

1.3.3. Doped Organic Photovoltaic Cells

Organic photovoltaic cell (OPV) has been actively studied for next generation of solar cells. However, in an individual organic semiconductor film, the thickness of the photoactive layer and the photocurrent are limited by the exciton diffusion length of 10 nm.[40,41] In order to improve photovoltaic performance, co-deposited films, i.e., blends of two types of organic semiconductor, have been developed (Fig. 1.3.3(a)).[9,42] The photocurrent can be generated in the whole of the co-deposited film since charge transfer (CT) excitons dissociate at the interfaces between the acceptors (A) and donors (D) (Figs. 1.3.3(b), (c)) and then the electrons and holes are transported to the electrodes. Co-deposited films have been fabricated by the co-evaporation technique. This film structure can be optimized by the blend ratio, the evaporation rate and the heating temperature.[43] For example, Sakai et al. has reported that the best blend ratio for fullerene and α-sexithiophene (C_{60}:6T) in a co-deposited film is 10:1 due to it having a high open-circuit voltage (V_{oc}) of 0.80 V.[44]

Moreover, to further increase the power conversion efficiency (η_p), Ishiyama et al. reported on a tandem OPV.[45-47] This cell was fabricated using only C_{60}:6T films connected in series with two p^+in^+-homojunctions. Here, + means heavily doped. The values of J_{sc}, V_{oc} and η_p increased from 4.5 mAcm^{-2}, 0.85 V and 1.6% (for a single OPV) to 3.0 mAcm^{-2}, 1.69 V and 2.4% (for a tandem OPV), respectively. Thus, impurity doping is an essential technique for enhancing photovoltaic performance.

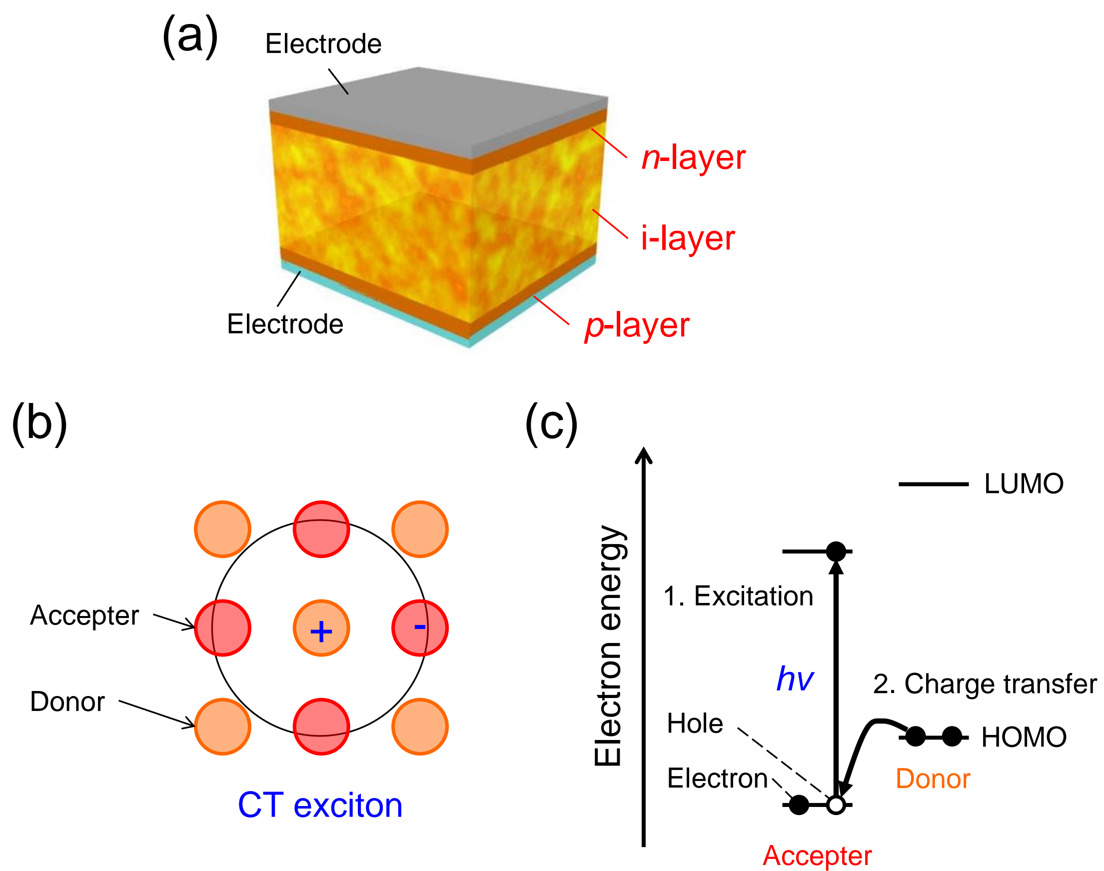

Fig. 1.3.3 (a) Schematic diagram of a *pin* cell using a co-deposited film. (b) Charge transfer (CT) exciton model. (c) Mechanism of carrier generation in an organic photovoltaic cell.

1.4. Measurement Techniques for Doped Organic Semiconductors

1.4.1. Energy Band Mapping

Energy band mapping was used to measure carrier concentration (N) and was demonstrated using the thickness dependence of the work function (Φ). The work function of doped organic semiconductors can be measured by ultraviolet photoelectron spectroscopy (UPS)[48)] or by Kelvin probe (see chapter 2.3.2)[49,50)].

Fig. 1.4.1 shows the principle of energy band mapping utilizing a *p*-type Schottky junction.[50)] When an organic semiconductor is formed on an ITO substrate, the Fermi level (E_F) of the *p*-layer is aligned with that of the ITO. Band bending occurs in the *p*-layer (black solid line). The thickness dependence of the work function directly shows the band bending because the work function is defined as the difference between the vacuum level and E_F. The width of the depletion layer (W_{dep}) and the built-in potential (V_{bi}) are determined by the point at which the bands are no longer bent (black arrow). N can be calculated using equation 1.4.1.1.

$$N = \frac{2\varepsilon\varepsilon_0 V_{bi}}{eW_{dep}^2} \qquad (1.4.1.1)$$

where ε is the dielectric constant of the organic semiconductor, which is about 4. ε_0 is the permittivity of free space, which is 8.85 x 10^{-12} Fm^{-1}. In addition, the energy band structure of the *p*-type Schottky junction was found by turning the curves in Fig. 1.4.1 upside down. This principle is used in chapters 3 and 5.

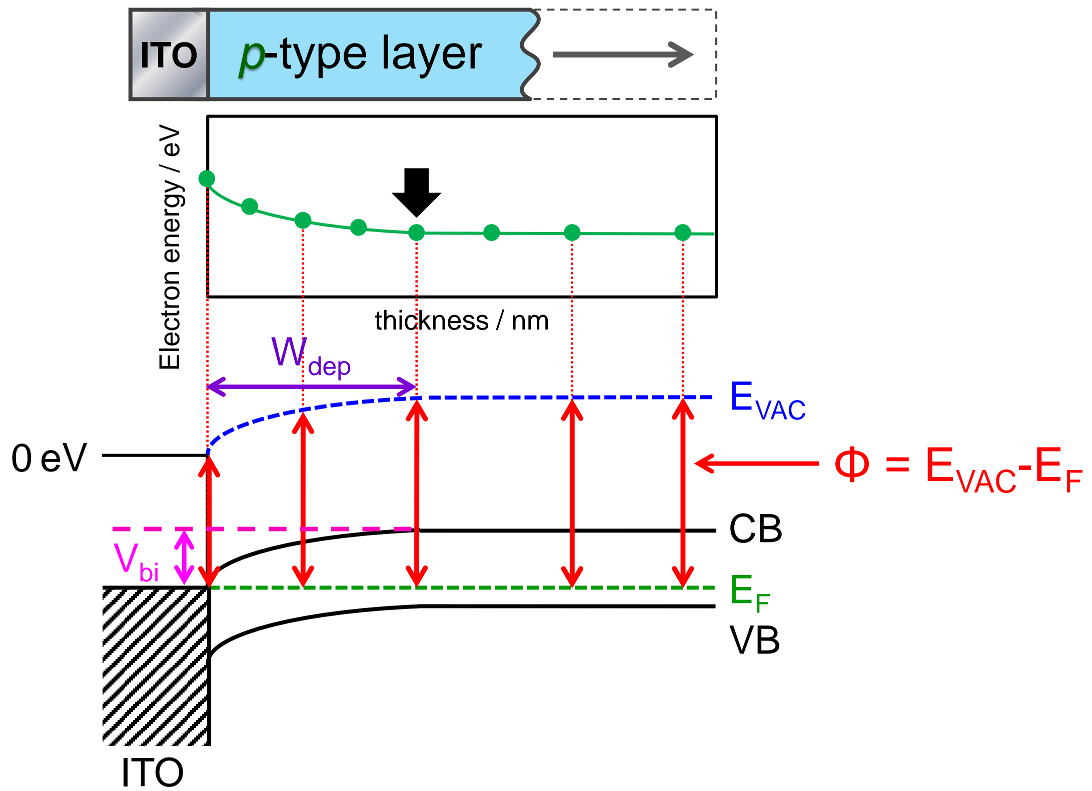

Fig. 1.4.1 Typical principle of energy band mapping in a *p*-type Schottky junction.

1.4.2. Hall Effect Measurements

The phenomenon of the Hall effect was discovered by Edwin Herbert Hall in 1879.[51)] Fig. 1.4.2 (a) shows schematic diagrams illustrating Hall effect measurements in a *p*-type organic semiconductor. When a magnetic field (B) (black mark) is applied perpendicular to the current (I) (blue solid line), the potential difference generated between the two electrodes by Lorentz force (green solid curve) as a result of this is called the Hall voltage (V_H). The carrier concentration per unit volume (N, cm^{-3}) can be determined from the following equation:

$$N = \frac{1}{R_H \cdot e} \qquad (1.4.2.1)$$

Here, d is the thickness and R_H is the Hall coefficient.

Positive and negative R_H correspond to positive (*p*) and negative (*n*) type materials, respectively. In addition, not only N but also the Hall mobility (μ_H) can be determined using the Hall effect using the following equation:

$$\mu_H = \sigma R_H \qquad (1.4.2.2)$$

where the carrier conductivity (σ) can be measured using the van der Pauw method. Trapped carriers make no contribution to μ_H since they cannot move under the influence of the Lorentz force (Fig. 1.4.2 (b)). Thus, μ_H is regarded as the intrinsic mobility without trap effect.

The standard method for separately and simultaneously determining N and μ in doped inorganic semiconductors is by making Hall effect measurements.[51)]

Fortunately, the Hall voltage of undoped rubrene single crystal, which possesses band-like transport properties, has been measured with the assistance of trap-healing[11)] and gate bias using a FET.[12,13)] The hole concentration per square centimeter ($N_{\square}$, cm^{-2}) and μ_H were determined to be 10^{11} cm^{-2} and 10 $cm^2V^{-1}s^{-1}$, respectively.[13)] However, the use of this method for doped organic single crystals without an FET has not, so far, been reported.

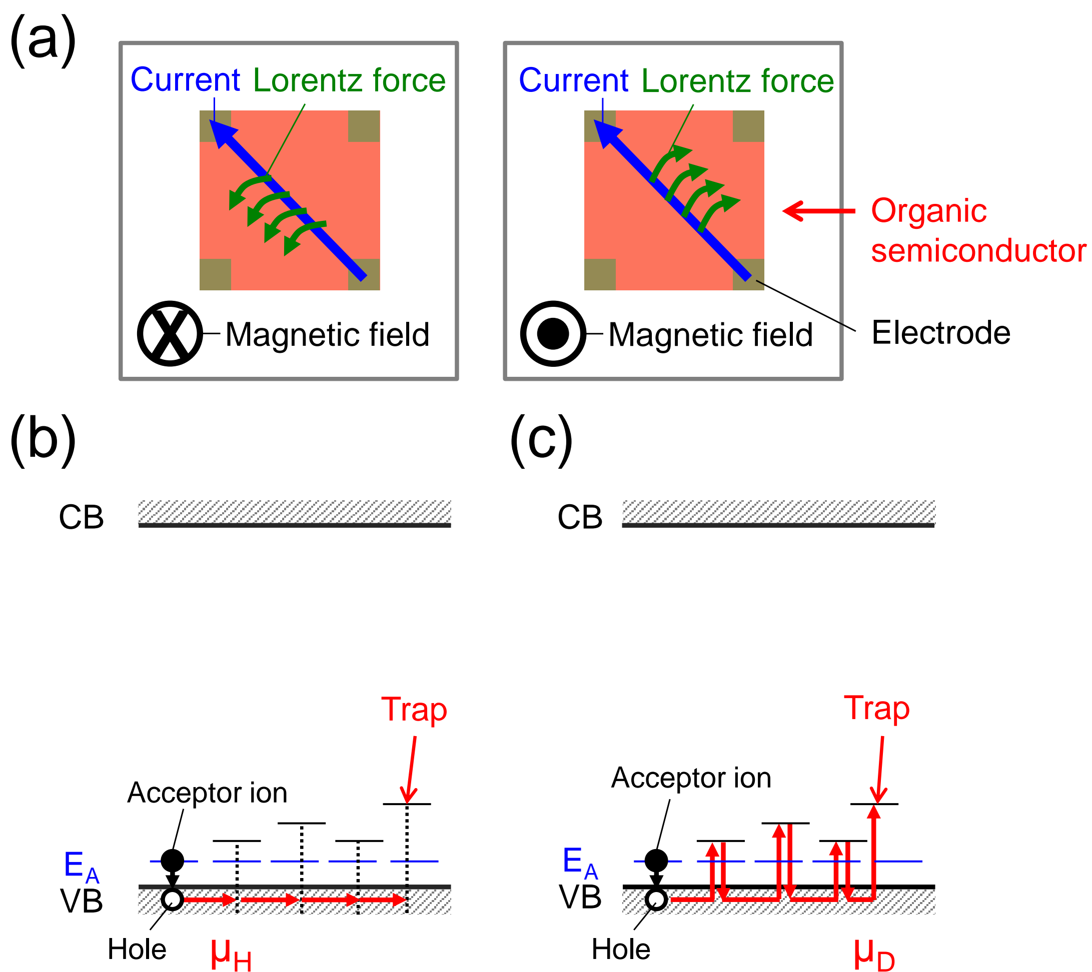

Fig. 1.4.2 (a) Schematic diagram illustrating Hall effect measurements. Models of (b) μ_H and (c) μ_D.

1.4.3. Organic Field-Effect Transistors

An organic field-effect transistor (OFET) comprises three electrodes (gate (G), source (S) and drain (D)), a gate insulator and a channel layer. As shown in Fig. 1.4.3, there are four types of device structure for OFETs; (a) bottom-gate/top-contact, (b) bottom-gate/bottom-contact, (c) top-gate/top-contact, and (d) top-gate/bottom-contact. In particular, the bottom-gate and top-contact OFET ((a)) has been well employed because the fabrication process is simple to use the silicon substrate. When a gate-source voltage (V_{GS}) is applied to an OFET, a source-drain current (I_{SD}) flows (Figs. 1.4.3(e), (f)). The FET mobility (μ_{FET}) can be determined from equations 1.4.3.1 and 1.4.3.2. In the linear region,

$$\mathrm{I_{DS}} = \frac{\mathrm{W}}{\mathrm{L}}\mu_{FET}\mathrm{C_i}\left\{(\mathrm{V_{GS}} - \mathrm{V_{th}})V_{DS} - \frac{1}{2}V_{DS}^2\right\} \quad (1.4.3.1)$$

In the saturation region,

$$\mathrm{I_{DS}} = \frac{\mathrm{W}}{2\mathrm{L}}\mu_{FET}\mathrm{C_i}(\mathrm{V_{GS}} - \mathrm{V_{th}})^2 \quad (1.4.3.2)$$

where W and L are the channel width and length, respectively. C_i is the capacitance per unit area of the gate dielectric layer and V_{th} is the threshold voltage.
μ_{FET} can be regarded as the drift mobility (μ_D). μ_D includes the effect of traps unlike the Hall mobility (μ_H) (Fig. 1.4.2(c)).

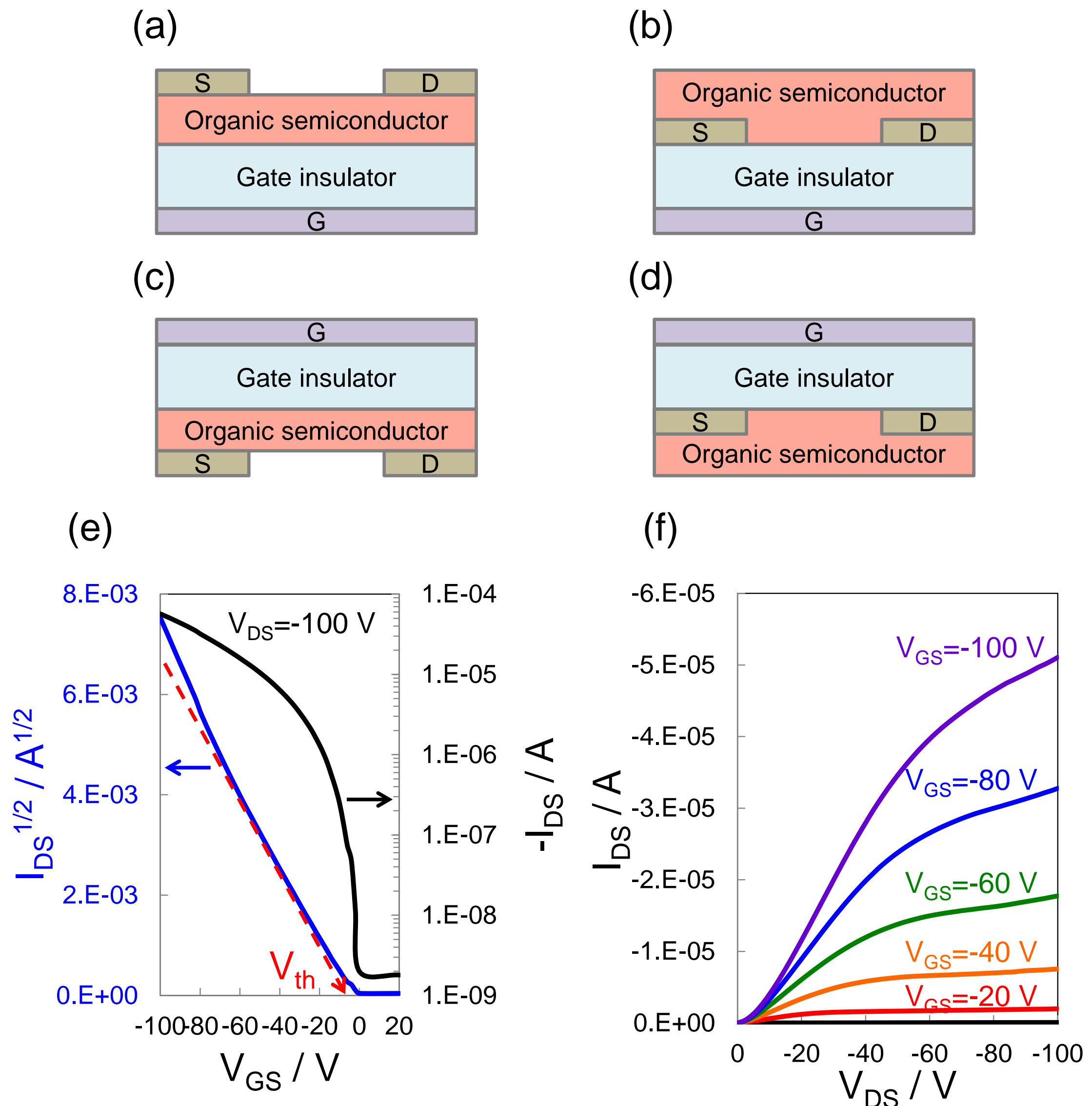

Fig. 1.4.3 (a), (b), (c), (d) Device structures of OFETs. (e) Transfer (I_{DS}-V_{GS}) and (f) output (I_{DS}-V_{DS}) characteristics.

1.4.4. Organic Photovoltaic Cells

An organic photovoltaic cell (OPV) comprises two electrodes (anode and cathode) and a photoactive layer. When the photoactive layer is irradiated with solar light, a photocurrent is generated in the OPV. Fig. 1.4.4(a) shows typical J-V characteristics in the dark and under irradiation with simulated solar light. The power conversion efficiency (η_p) can be calculated using the following equation:

$$\eta_P = \frac{P_{max}}{P_{in}} = \frac{J_{sc} \cdot V_{oc} \cdot FF}{P_{in}} \quad (1.4.4.1)$$

Here, J_{sc} is the short-circuit photocurrent density, which is obtained from the value of J at V = 0V, and V_{oc} is the open-circuit voltage, which is obtained from the value of V at J = 0 $mAcm^{-2}$. The fill factor (FF) can be calculated from the following equation:

$$FF = \frac{P_{max}}{J_{sc} \cdot V_{oc}} = \frac{J_{max} \cdot V_{max}}{J_{sc} \cdot V_{oc}} \quad (1.4.4.2)$$

where P_{max} is the maximum power output, which is obtained from the values of the current and voltage (J_{max} and V_{max}). P_{in} is the incident light intensity, which is usually used for AM 1.5G (100 $mWcm^{-2}$).

Fig. 1.5.2(b) shows typical external quantum efficiency (EQE) of OPV. EQE can be calculated from the ratio of the number of carriers collected to the number of incident photons under the short-circuit condition as the following equation.

$$EQE = \frac{N_{collected\ carrier}}{N_{photons}} \quad (1.4.4.3)$$

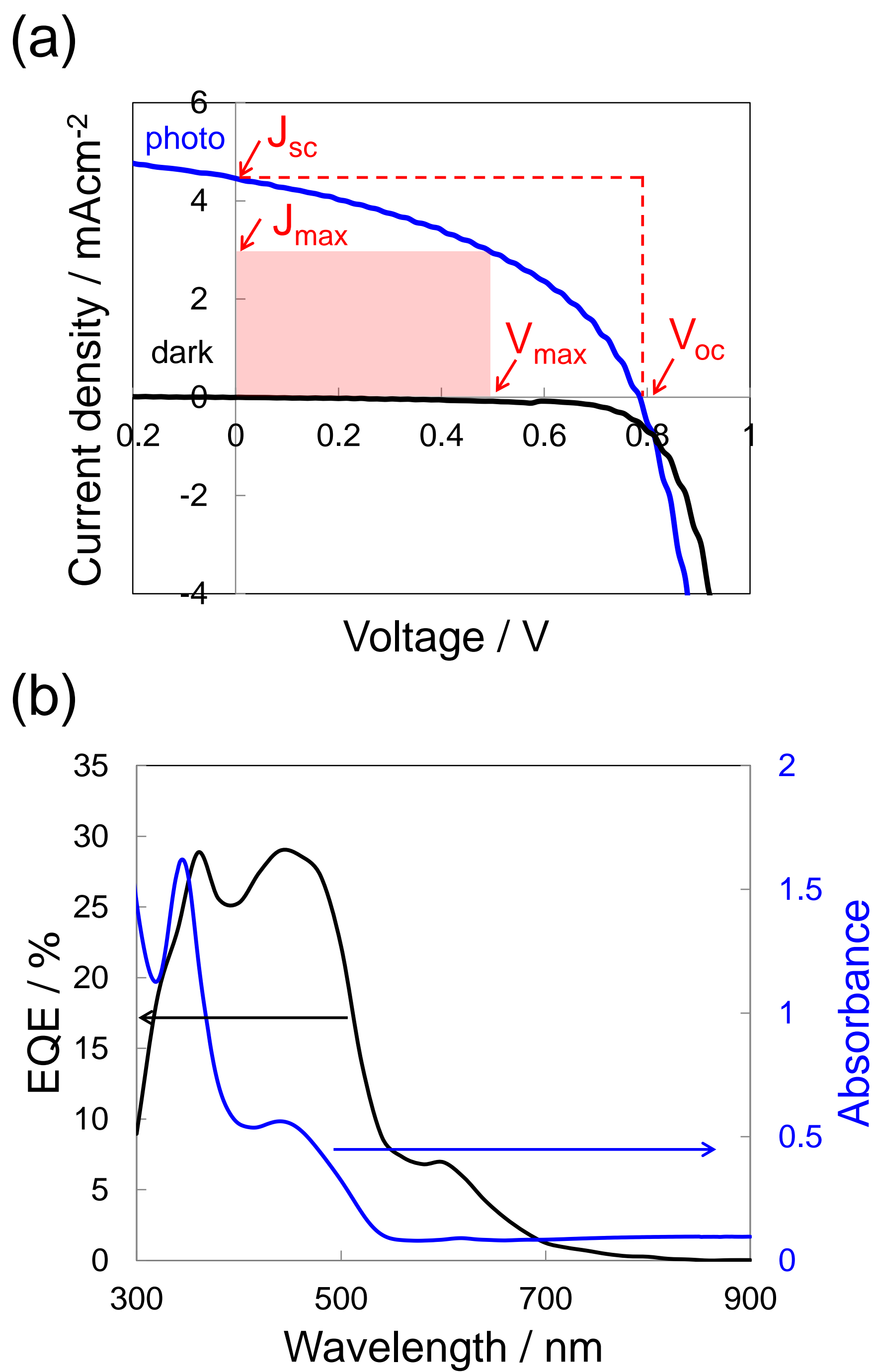

Fig. 1.4.4 (a) Typical J-V characteristics in the dark and under irradiation with simulated solar light. (b) EQE of typical OPV.

1.5. Motivation for This Doctoral Thesis

In this doctoral thesis, the author has focused on the development of a precise impurity doping technique at the ppm level both for organic thin films and organic single crystals. The main tasks undertaken were as follows.

(i) Effects of impurity doping in organic single crystals (chapters 3 and 4)

Doping to organic semiconductors have been performed in the amorphous and the polycrystalline films so far. However, the author believes that in order to precisely clarify the nature of the doping effects, doping organic single crystal without grain boundaries is necessary. When the impurity doping is applied to the single crystalline layers, the deposition rates of both the organic semiconductor and the dopant need to be minimized in order to suppress the structural defect. Thus, firstly, the author attempted to fabricate doped organic single crystals by means of an ultra-slow co-deposition technique. Secondly, the author attempted to demonstrate Hall effect measurements and organic field-effect transistors in doped organic single crystals for the first time.

(ii) Effects of impurity doping in organic photovoltaic cells (chapter 5)

In order to achieve a specific energy band structure, impurity doping is the standard technique for organic photovoltaic cells (see chapter 1.3.3). However, in conventional cells, the photocurrent is generated in an undoped co-deposited layer, i.e., the *i*-layer. The author believes that direct doping of a photoactive co-deposited layer provides us with the potential to enhance the photovoltaic performance. Thus, the author attempted to confirm this by using extremely low doping concentrations of 1 ppm for the first time.

1.6. Overview for This Doctoral Thesis

This thesis consists of six chapters.

In chapter 1, the background to the impurity doping of both inorganic and organic semiconductors and the motivation for carrying out the research work described in this thesis are presented.

In chapter 2, the experimental equipment and methods are described. Rubrene single crystals possessing band-like transport properties were employed for the Hall effect measurements. Co-deposited films of fullerene and α-sexithiophene (C_{60}:6T) were used for the organic photovoltaic cells. Iron chloride ($FeCl_3$) and cesium carbonate (Cs_2CO_3) were used for the accepter and donor dopants, respectively. Doped organic semiconductors were fabricated using a 'multi-component co-evaporation' technique. The deposition rates of the dopants were monitored using a quartz crystal microbalance equipped with a computer monitoring system. These rates were controlled using rotating shutters with aperture ratios of 1/10, 1/100, and 1/1000, which enabled us to control the doping concentration to as low as 1 ppm.

In chapter 3, the Hall effect measurements made on the doped organic single crystals is described. Also, the first successful achievement of the fabrication of a doped homoepitaxial single crystal layer on rubrene single crystal by an ultra-slow co-deposition technique is described. The minimum deposition rate for 1 ppm doping with $FeCl_3$ was 10^{-9} nm s^{-1}. A systematic study of both the hole concentration per unit volume (N, cm^{-3}) and the Hall mobility (μ_H) of $FeCl_3$-doped homoepitaxial rubrene single crystal was carried out using Hall effect measurements. With 100 ppm doping, $N = 2.6 \times 10^{17}$ cm^{-3} and $\mu_H = 1.4$ $cm^2V^{-1}s^{-1}$ were obtained. It was found that (i) the doping efficiency, i.e. the ionization rate of the acceptor dopant, of the rubrene single

crystal (24%) was higher than that of a rubrene vacuum deposited film (1.2%), which can be attributed to the lower concentration of hole traps and that (ii) there was a decrease in μ_H from 4.6 to 0.13 $cm^2V^{-1}s^{-1}$ as the doping concentration was increased from 10 to 1000 ppm, which can be attributed to scattering effects due to lattice disturbances. These results are a first example of Hall effect measurements made on doped organic single crystals.

In chapter 4, the field-effect mobility of doped organic single crystals are described. FET mobility (μ_{FET}) can be regarded as the drift mobility (μ_D), which is dominated by hole traps. μ_D was about two-orders of magnitude less than the Hall mobility (μ_H). Since holes captured by traps cannot move under the influence of the Lorentz force, μ_H contains no contribution from the trapped holes. So, we concluded that the lower μ_D values can be attributed to the effect of hole traps formed by lattice disturbances, which decrease the velocity of the holes by capturing them. The activation energy of the hole traps was determined to be 0.37 eV by measuring the temperature dependence of μ_D.

In chapter 5, the effects of impurity doping in simple n^+p-homojunction organic photovoltaic cells are described. Here, + means heavily doped. The n^+p-homojunctions were formed in C_{60}:6T co-deposited films with acceptor ($FeCl_3$) and donor (Cs_2CO_3) dopants. The doping concentration of $FeCl_3$ in the *p*-layer was varied from 1 to 1000 ppm. The doping effects can be divided into three regions. Firstly, from 0 to 10 ppm, the fill factor (FF) increased due to the appearance of majority carriers (holes). Secondly, from 10 to 100 ppm, the photocurrent density (J_{sc}) increased due to an increase in the built-in potential, i.e., the formation of an n^+p-homojunction. Thirdly, above 100 ppm, FF and J_{sc} decreased due to the decrease in hole mobility and

depletion layer width, respectively. Thus, we confirmed that the photovoltaic cell performance could be enhanced by the extremely low doping concentration of 1 ppm.

In chapter 6, the conclusion to this thesis and prospects for the future are presented.

1.7. References

1) The Royal Swedish Academy of Sciences in the Nobel Prize in Physics 2014.
2) Physics of Semiconductor Devices, S. M. Sze, published by WILEY-INTERSCEINCE, Chapter 2 (1969).
3) H. Akamatsu, H. Inokuchi, and Y. Mastunaga, *Nature*., **173**, 168 (1954).
4) C. W. Tang, S. A. Vanslyke, *Appl. Phys. Lett.*, **51** 913 (1987).
5) C. W. Tang, *Appl. Phys. Lett.*, **48** 183 (1986).
6) K. Kudo, M. Yamashina, and T. Morizumi, *Jpn. J. Appl. Phys*., **23**, 130 (1984).
7) Physics of Organic Semiconductors, W. Brutting, edited by WILEY-VCH Verlag GmbH & Co. KGaA, Chapter 1 (2005).
8) Sony corporation in 2007.
9) M. Hiramoto, M. Kubo, Y. Shinmura, N. Ishiyama, T. Kaji, K. Sakai, T. Ohno, and M. Izaki, *Electronics.*, **3**, 351 (2014).
10) B. Luussem, C.M. Keum, D. Kasemann, B. Naab, Z. Bao, and Karl Leo, *Chem. Rev*.,**116**, 13714 (2016).
11) B. Lee, Y. Chen, D. Fu, H. T.Yi, K. Czelen, H. Najafov, and V. Podzorov, *Nat. Mater.*, **12**, 1125 (2013).
12) V. Podzorov, E. Menard, J. A. Rogers, and M. E. Gershenson, *Phys. Rev. Lett*., **95,** 226602 (2005).
13) J. Takeya, J. Kato, K. Hara, M. Yamagishi, R. Hirahara, K. Yamada, Y. Nakazawa, S. Ikehata, K. Tsukagoshi, Y. Aoyagi, T. Takenobu, and Y. Iwasa, *Phys. Rev. Lett*., **98**, 196804 (2007).
14) Physics of Semiconductor Devices, S. M. Sze, published by WILEY-INTERSCEINCE, Chapter 3 (1969).

15) Ge. R. Hutchison, M. A. Ratner, and T. J. Marks, *J. Am. Chem. Soc*., **127**, 2339 (2005).

16) T. Kanbara, K. Shibata, S. Fujiki, Y. Kubozono, S. Kashino, T. Urisu, M. Sakai, A. Fujiwara, R. Kumashiro, and K. Tanigaki, *Chem Phys Lett.*, **379**, 223 (2003).

17) M. Hiramoto, K. Ihara, H. Fukusumi, and M. Yokoyama, *J. Appl. Phys*., **78**, 7153 (1995).

18) M. Maitrot, G. Guilland, and B. Boudjema, J. J. Andre, and J. Simon, *J. Appl. Phys*., **60**, 2396 (1986).

19) E. J. Lous, P. W. M. Blom, L. W. Molenkamp, and D. M. Leeuw, *Phys. Rev. B.*, **51**, 17251 (1995).

20) M. L. Tietze, P. Pahner, K. Schmidt, K. Leo, and B. Lussem, *Adv. Funct. Mater.,* **25,** 2701 (2015).

21) M. Kroger, S. Hamwi, J. Meyer, T. Riedl, W. Kowalsky, and A. Kahn, *Org. Electron.,* **10**, 932 (2009).

22) M. Kubo, Y. Shinmura, N. Ishiyama, T. Kaji, and M. Hiramoto, *Mol. Cryst. Liq. Cryst*., **581** 13 (2013).

23) J. Endo, T. Matsumoto, and J. Kido, *Jpn. J. Appl. Phys*., **41**, 358 (2002).

24) D. L. Price, M. L. Saboungi, and Y. S. Badyal, *Phys. Rev. B.*, **57**, 10496 (1998).

25) G. Parthasarathy, C. Shen, A. Kahn, and S. R. Forrest, *J. Appl. Phys*., **89**, 4986 (2001).

26) C. K. Chiang, S.C. Gau, C. R. Fincher, Jr,, Y. W. Park, A. G. MacDiarmid, and A. J. Heeger, *Appl. Phys. Lett*., **33**, 18 (1978).

27) T. Takenobu, T, Takano, M, Shiraishi, Y, Murakami, M, Ata, H, Kataura, Y, Achiba and Y. Iwasa, *Nat. Mater.*, **2**, 68 (2003).

28) M. Chikamatsu, T. Taima, Y. Yoshida, K. Saito, and K. Yase, *Appl. Phys. Lett.*, **84**, 128 (2004).

29) M. Kubo, T. Kaji, and M. Hiramoto, AIP Advances., 1, 032177 (2011).

30) H. H. Liao, L. M. Chen, Z. Xu, G. Li, and Y. Yang, *Appl. Phys. Lett.*, **92,** 173303 (2008).

31) N. Ishiyama, M. Kubo, T. Kaji, and M. Hiramoto, *Appl. Phys. Lett.*, **101**, 233303 (2012).

32) E. J. Meijer, D. M. Deleeuw, S. Setayesh, E. V. Veenendaal, B. H. Huisman, P. W. Blom, J. C. Hummelen, U. Scherf, and T. M. Klapwijk, *Nat. Mater.*, **2**, 678 (2003).

33) R. W. I. deBoer, A. F. Stassen, M. F. Craciun, C. L. Mulder, A. Molinari, S. Rogge, and A. F. Morpurgoa, *Appl. Phys. Lett.*, **86,** 262109 (2005).

34) Y. Takahashi, T. Hasegawa, Y. Abe, Y. Tokura, and G. Saito, *Appl. Phys. Lett.*, **88,** 073504 (2006).

35) A. Dodabalapur, H. E. Katz, L. Torsi and R. C. Haddon, *Appl. Phys. Lett.*, **68,** 1108 (1996).

36) M. Kubo, K. Iketaki, T. Kaji, and M. Hiramoto, *Appl. Phys. Lett.*, **98**, 073311 (2011).

37) M. Kubo, T. Kaji, and M. Hiramoto, *AIP Advances.,* **1**, 032177 (2011).

38) D. L. Price, M. L. Saboungi, and Y. S. Badyal, *Phys. Rev. B.*, **57**, 10496 (1998).

39) Y. Shinmura, Y. Yamashina, T. Kaji, and M. Hiramoto, *Appl. Phys. Lett.*, **105**, 183306 (2014).

40) P.Peumans, A. Yakimov, and S.R. Forrest, *J. Appl. Phys*., 93, 3693 (2003).

41) M. Hiramoto, T. Yamaga, M. Danno, K. Suemori, Y. Matsumura, and M. Yokoyama, *Appl. Phys. Lett*., **88**, 213105 (2006).

42) M. Hiramoto, H. Fujiwara1 and M. Yokoyama, *J. Appl. Phys*., **72**, 3781 (1992).

43) T. Kaji , M. Zhang , S. Nakao , K. Iketaki , K. Yokoyama , C. W. Tang , and M. Hiramoto, *Adv. Mater*., **23**, 3320 (2011).

44) J. Sakai, T. Taima, and K. Satio, *Organic Electronics*, **9**, 582 (2008).

45) N. Ishiyama, M. Kubo, T. Kaji, and M. Hiramoto, *Appl. Phys. Lett.*, **101,** 233303 (2012).

46) N. Ishiyama, T. Yoshioka, T. Kaji, and M. Hiramoto, *Appl. Phys. Express.*, **6**, 012301 (2013).

47) N. Ishiyama, M. Kubo, T. Kaji, and M. Hiramoto, *Org. Electron*., **14**, 1793 (2013).

48) J. Blochwitz, T. Fritz, M. Pfeiffer, K. Leo, D.M. Alloway, P.A. Lee, and N.R. Armstrong, *Org. Electron*., **2**, 97 (2001).

49) Y. Shinmura, T. Yoshioka, T. Kaji, and M. Hiramoto, *Appl. Phys Express.*, **7**, 071601 (2014).

50) Y. Yamashina, Y. Shinmura, N. Ishiyama, T. Kaji, and M. Hiramoto, *J. Appl. Phys.,* **117**, 125501 (2015).

51) Physics of Semiconductor Devices, S. M. Sze, published by WILEY-INTERSCEINCE, Chapter 3 (1969).

Chapter 2:

Experimental Equipment and Methods

2.1. Purification of Organic Semiconductors

α-sexithiophene (6T) (Tokyo Chemical Industry), rubrene (Tokyo Chemical Industry) and fullerene (C_{60}) (Frontier Carbon, nanom purple TL) were purified by single crystal sublimation (Fig. 2.1) (EpiTech Inc).[1,2] The sublimation purifier had three temperature zones, high (green) at one end, low (blue) at the other end, and moderate (red) in between. The samples were put into the high temperature end near the heat source and were evaporated in the quartz tube under N_2 flow. Highly purified single crystals (99.99999%) were separated from the impurities in the moderate and low temperature zones utilizing the difference in deposition temperatures. Organic single crystals several millimeters in size were grown. Details of the sublimation conditions used to prepare these highly purified organic semiconductors are given in Table 2.1.

The acceptor dopants, iron(III) chloride ($FeCl_3$) (Sigma-Aldrich, 99.99%)[3,4], and the donor dopant, cesium carbonate (Cs_2CO_3) (Sigma-Aldrich, 99.995%)[5,6], were used without further purification. Aluminum (Al) (New Metals & Chemicals Ltd, 99.999%) and gold (Au) (Nilaco, 99.95%) were used for the electrodes.

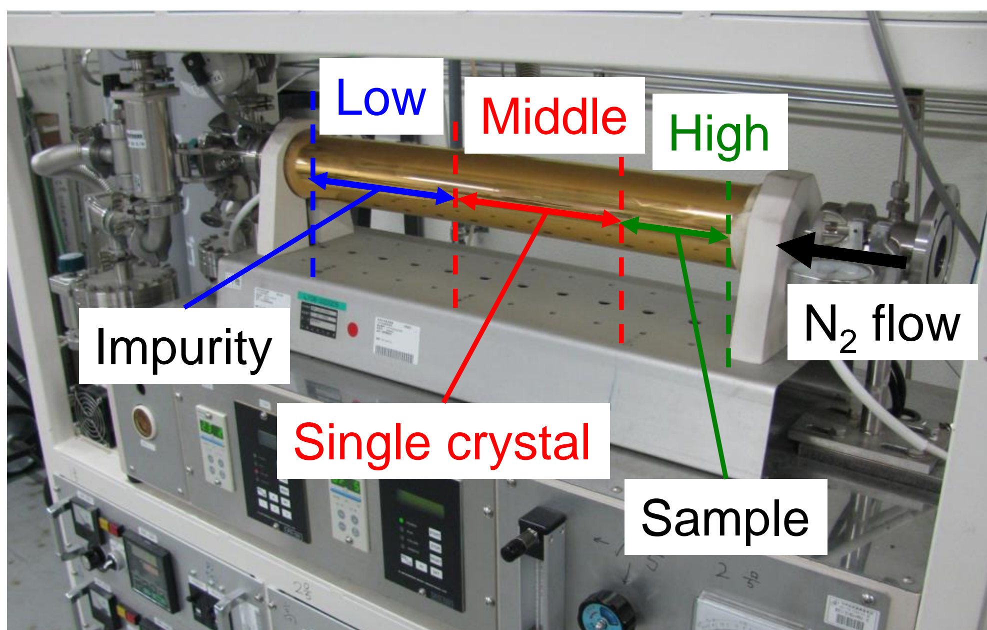

Fig. 2.1 Single crystal sublimation of highly purified organic semiconductors.

Table 2.1 Sublimation conditions.

Sample	Temperature / °C			Heating time / h
	High	Middle	Low	
6T	320	250	170	1
Rubrene	320	250	170	1
C_{60}	745	580	310	36

2.2. Extremely Low Concentration Doping for Organic Semiconductors

Doping for the organic semiconductors was performed using a multi-component co-evaporation technique as shown in Fig. 2.2.1.[2] The evaporation sources were prepared in melting pots of aluminum oxide (Al_2O_3) (Nilaco, C-1). All materials were independently evaporated using tungsten basket resistance heaters (Nilaco, BH-1) under vacuum (> 10^{-5} Pa). The deposition rates were controlled using quartz crystal microbalances (QCMs) (INFICON, 750-1050-G10) connected to a computer monitoring system (ULVAC, CRTM-9000G/Depoview). The thicknesses of the deposited films were measured by a surface profiler (Fig. 2.2.3) (Veeco, Dektak150). The actual thicknesses were determined using a tooling factor.

Fig. 2.2.2 shows a typical example of the dependence of the dopant thickness on the deposition time at a deposition rate of 1.0 x 10^{-5} nm s^{-1}. The observed cyclic fluctuations were caused by temperature variations in the coolant water for the QCMs. The deposition rate can be estimated from the gradient of the baseline (red). As the deposition rates of the organic semiconductor and the dopant were 1.0 and 1.0 x 10^{-5} nm s^{-1}, respectively, the doping concentration was 100 ppm. Extremely low doping concentrations of 10 and 1 ppm were realized by reducing the dopant evaporation rate using rotating disks containing slits with aperture ratios of 1:10 and 1:100, respectively (Fig. 2.2.4). In addition, in order to grow homoepitaxial films on the single crystal substrate, rubrene was deposited at a low evaporation rate of 3.3 x 10^{-3} nm s^{-1} at room temperature (Fig. 2.2.1 (a)).[7] The minimum deposition rate for 1 ppm doping with dopant ($FeCl_3$) was 3.3 x 10^{-9} nm s^{-1}.

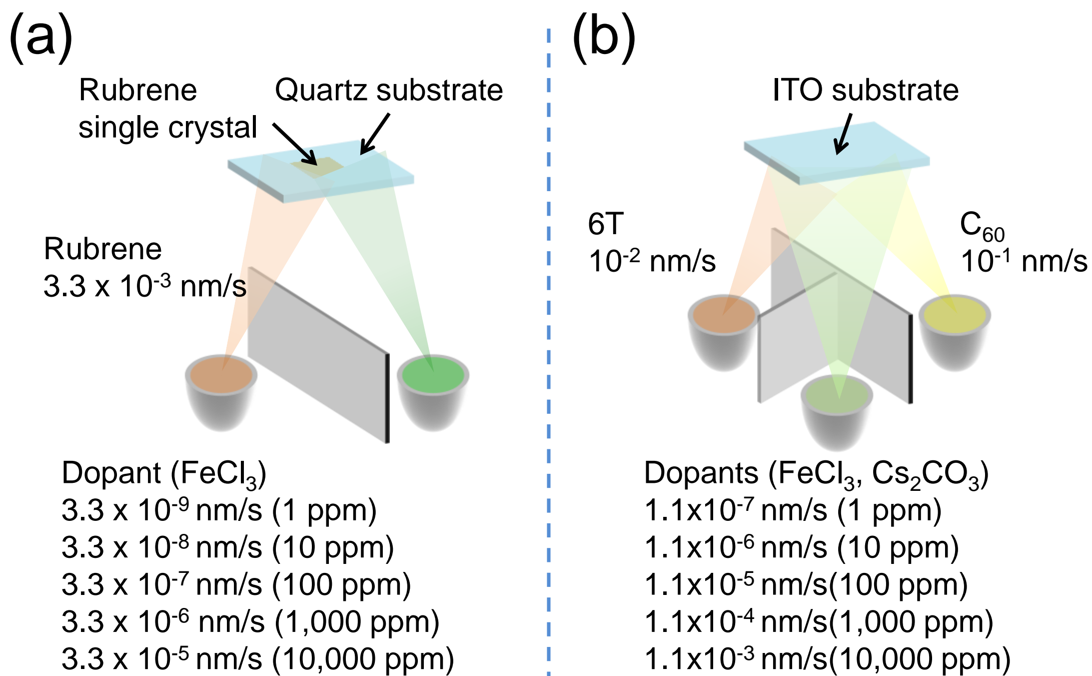

Fig. 2.2.1 Illustration showing (a) 'Two-component co-evaporation technique' and (b) 'Three-component co-evaporation technique'.

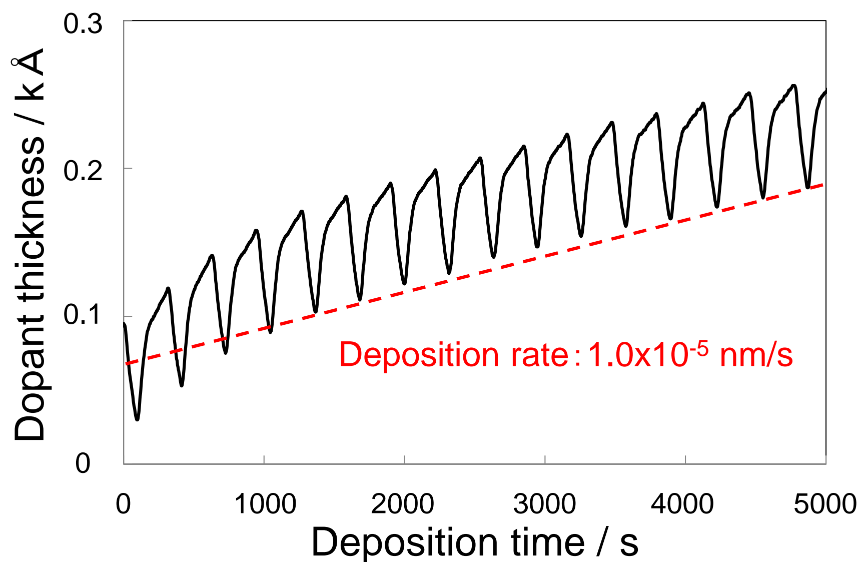

Fig. 2.2.2 Typical dependence of dopant thickness on deposition time at a rate of 1.0 x 10^{-5} nm s^{-1}.

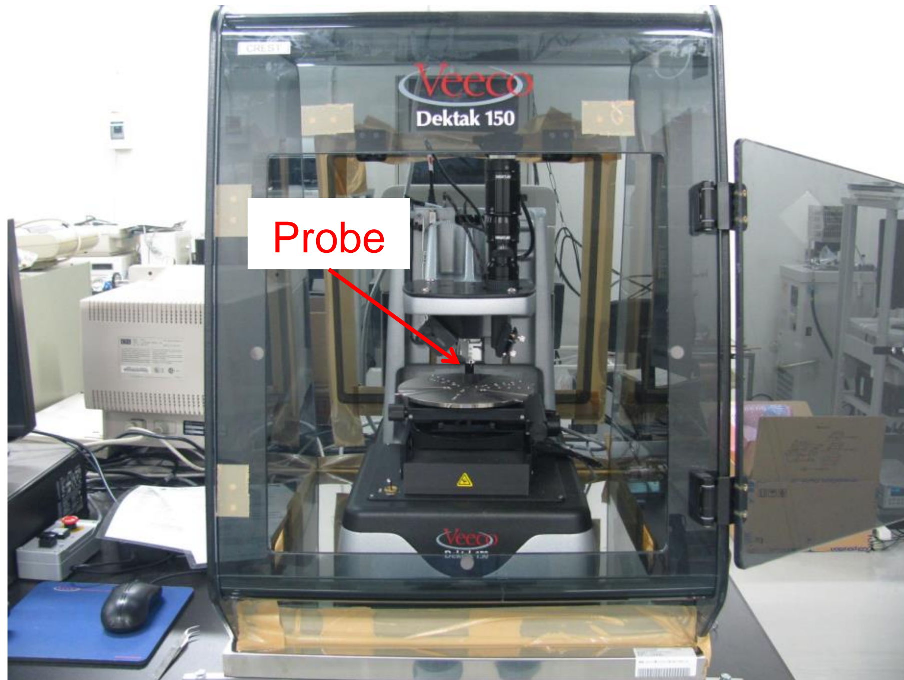

Fig. 2.2.3 Surface profiler for measuring thickness.

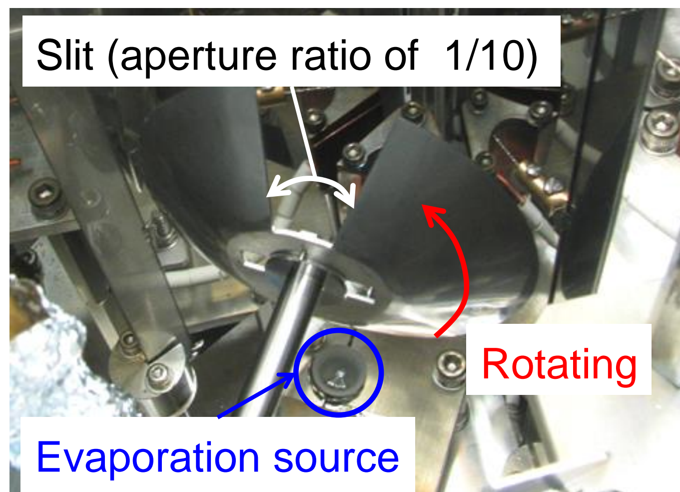

Fig. 2.2.4 Rotating disk containing slits with an aperture ratio of 1:10 for extremely low concentration doping.

2.3. Measurements of Doped Organic Semiconductors

2.3.1. Hall effect Measurements

Hall effect measurements[8-10] were performed as shown in Fig. 2.3.1.1. The samples were fabricated on quartz substrates. Doping for the organic semiconductors was performed using the multi-component co-evaporation technique (see section 2.2), and electrodes were evaporated onto the organic thin films through a metal mask. The distance between the electrodes (L) was 50 μm. To prepare ohmic contacts, heavily doped layers were fabricated beneath the electrodes.[11]

Fig. 2.3.1.2 shows a typical example of the variation of the Hall voltage with the magnetic field. The Hall voltage (V_H) is obtained from the amplitude, as shown in the figure. The Hall coefficient (R_H) can be determined from the following equation:

$$R_H = \frac{V_H \cdot d}{I \cdot B} \qquad (2.3.1.1)$$

where d is the film thickness, and I and B are the current and magnetic flux density, which were usually 1.0 x 10^{-7} A and ±1 T, respectively.

The carrier concentration per unit volume (N, cm^{-3}) and mobility ($cm^2V^{-1}s^{-1}$) were determined by the observed R_H (detail in chapter 1.4.2).

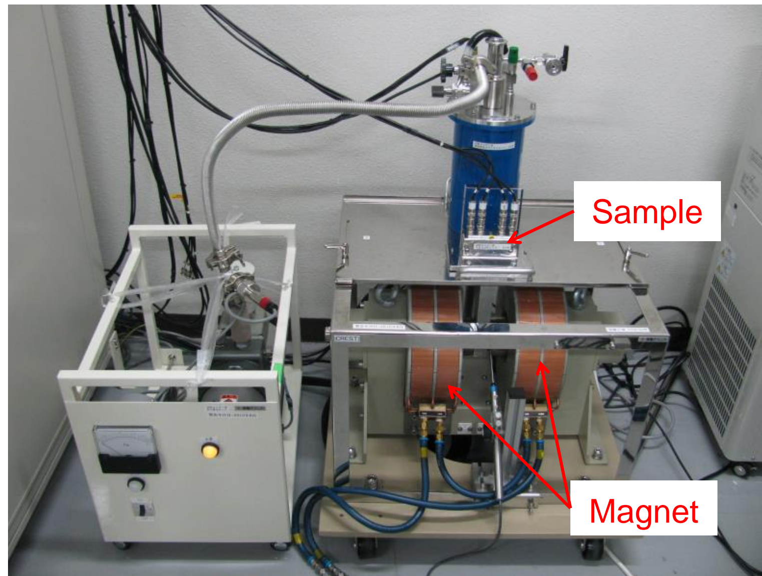

Fig. 2.3.1.1 Hall-effect measurement using the van der Pauw method

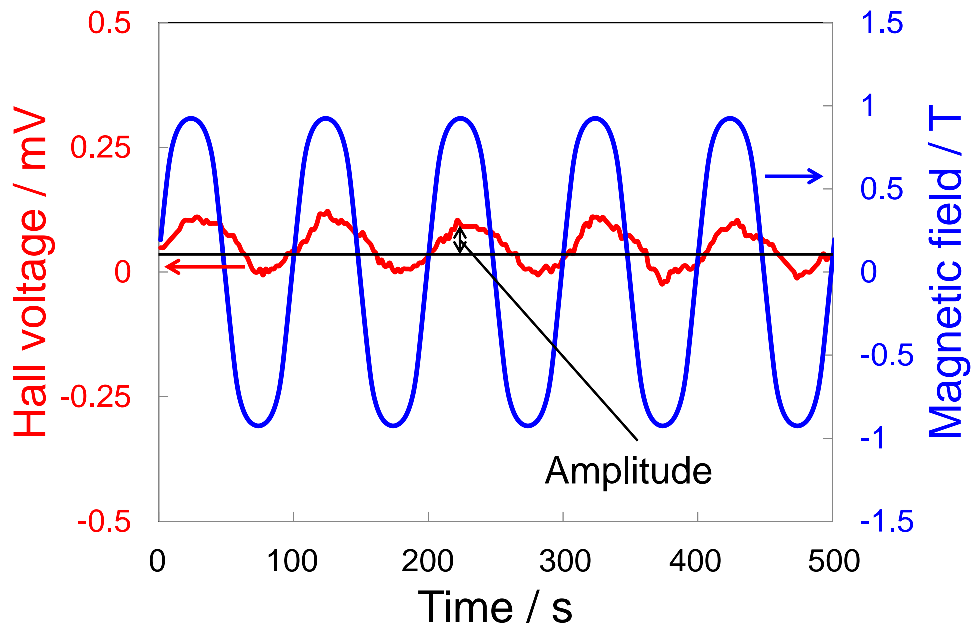

Fig. 2.3.1.2 Typical variation of the Hall voltage with the magnetic field.

2.3.2. Kelvin Probe Measurements

The Fermi energy (E_F) for undoped and doped organic semiconductors was observed using the Kelvin Probe method (Riken Keiki, FAC-1).[12] Since the value of E_F is sensitive to air, all the samples were fabricated in a glove box (Fig. 2.3.2.1), in which the concentrations of water (H_2O) and oxygen (O_2) were kept to 0.5 and 0.2 ppm, respectively. Fig. 2.3.2.2(a) shows the setup for this measurement.[13] When the film is brought into contact with a standard gold (Au) plate, the Fermi levels shift to become aligned (Fig. 2.3.2.2(b)), and a potential difference ($\Delta\Phi$), equivalent to the metal work function difference, forms at the interface between the organic semiconductor and the gold. To make the measurement, an alternating current (AC) is generated in the circuit by vibrating the plate. The value of $\Delta\Phi$ is measured from the voltage required to cancel the alternating current ($Q = 0$) (Fig. 2.3.2.2(c)). Since the work function of Au is known to be 4.40 eV, the position of E_F in the organic semiconductor can be simply determined from $\Delta\Phi$.

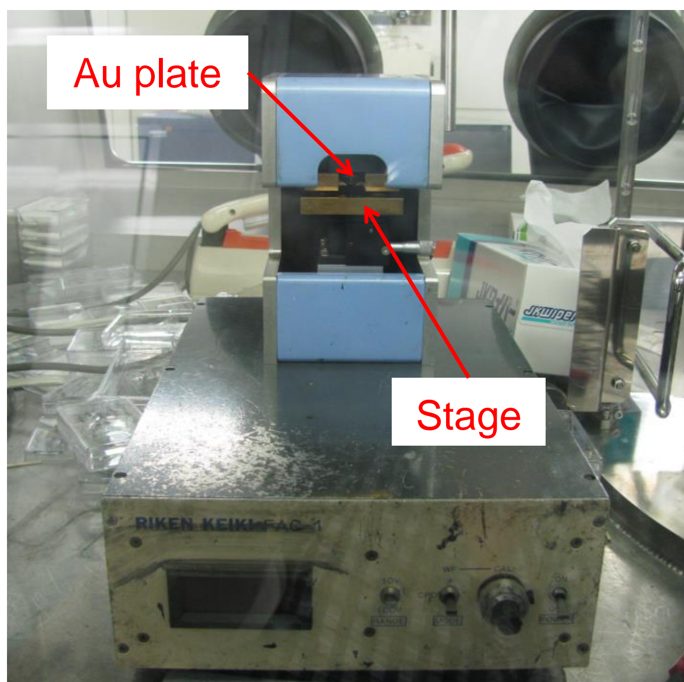

Fig. 2.3.2.1 Kelvin probe measurements in a glove box.

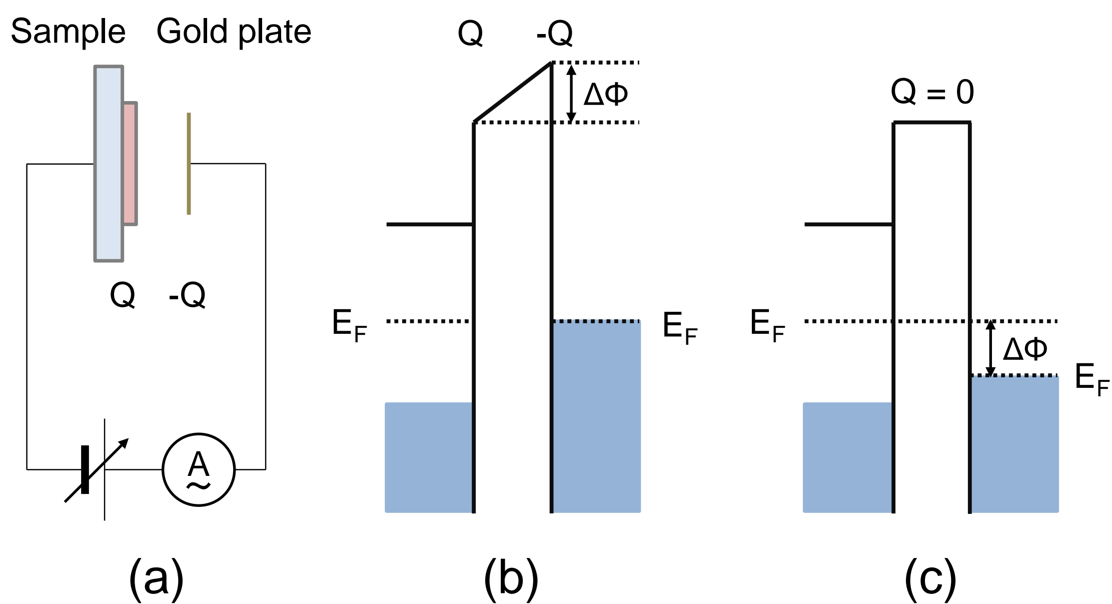

Fig. 2.3.2.2 (a) Setup for the Kelvin probe measurements. (b) Energy band diagram with Fermi levels aligned. (c) Energy band diagram with Q = 0.

2.3.3. Organic Field-Effect Transistors

The transfer (I_{DS}-V_{GS}) and output (I_{DS}-V_{DS}) characteristics of a Field-Effect Transistor (FET) were measured using a semiconductor characterization system (KEITHLEY, 4200-SCS) as shown in Fig. 2.3.3.

Bottom gate and top contact Field-Effect Transistors (FET) were fabricated on heavily n-doped silicon substrates. Electrodes were evaporated onto the organic thin films through a metal mask. The channel width (W) and length (L) were 1.0 mm and 50 μm, respectively. To prepare ohmic contacts, heavily doped layers were fabricated beneath the electrodes.[11)]

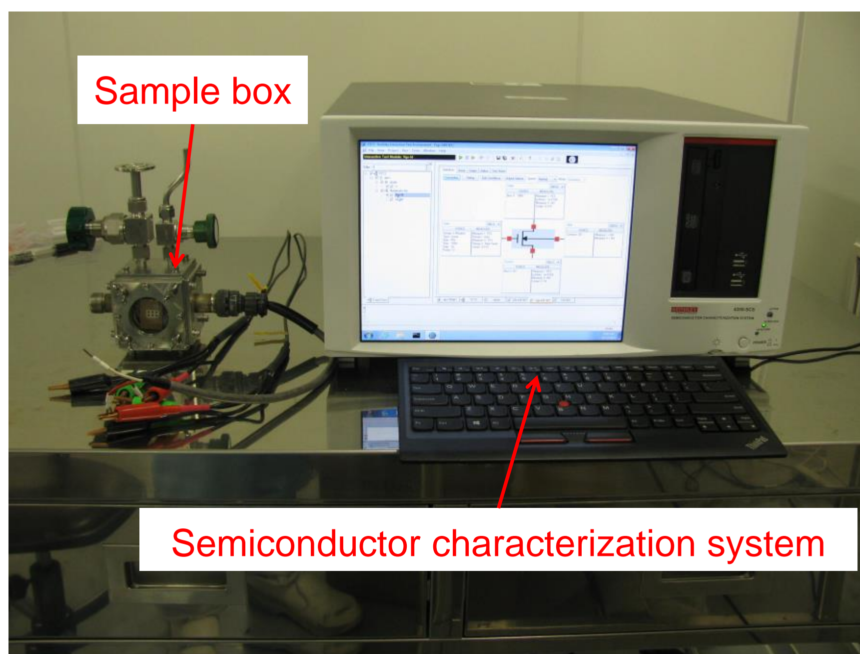

Fig. 2.3.3 Semiconductor characterization system for FET measurements.

2.3.4. Organic Photovoltaic Cells

In the case of the photovoltaic properties, the cells were firstly fabricated on patterned indium tin oxide (ITO) substrates. Electrodes were evaporated onto the organic thin films through a metal mask with an aperture area of 0.06 cm^2. To measure the photovoltaic properties, all the cells were set into a sample container with a quartz glass window and electrical connecting ports (EpiTech Inc) as shown in Fig. 2.3.4.1. The container was evacuated to 10^{-3} Pa during the measurements. The photo-irradiated area was precisely defined by a photomask with an aperture area of 0.04 cm^2.

Current density-voltage (J-V) measurements with a solar simulator (AM1.5, 100 $mWcm^{-2}$) (USHIO INC, MS110AAA), as shown in Fig. 2.3.4.2, were made in order to determine some of the photovoltaic properties. Other photovoltaic properties were observed using the action spectrum measurement system shown in Fig. 2.3.4.3. The external quantum efficiency (EQE) can be calculated from the ratio of the number of carriers collected to the number of incident photons under the short-circuit condition. The number of carriers was measured by irradiating the cells with a Xe-lamp through a monochromator (Shimadzu, SPG-3ST). The number of incident photons was measured by the same method using a silicon photodiode (Hamamatsu Photonics, S1337-66BQ).

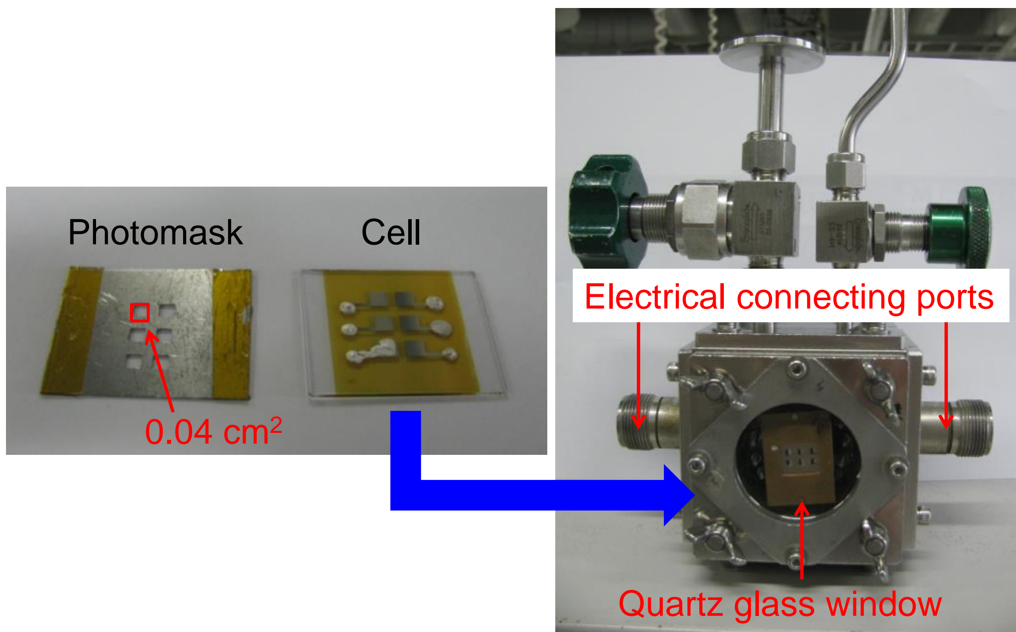

Fig. 2.3.4.1 Setting the cells into the sample container for measurement of the photovoltaic properties.

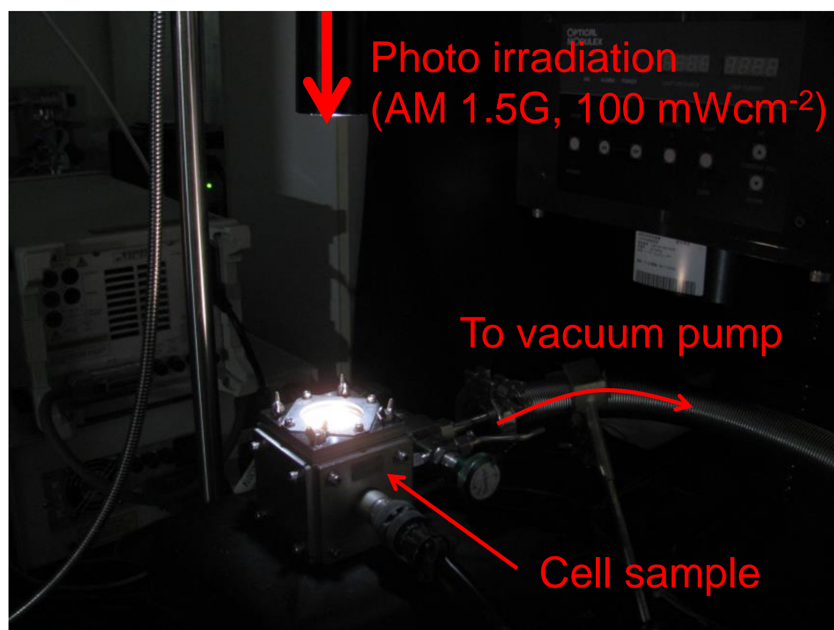

Fig. 2.3.4.2 J-V measurement with a solar simulator.

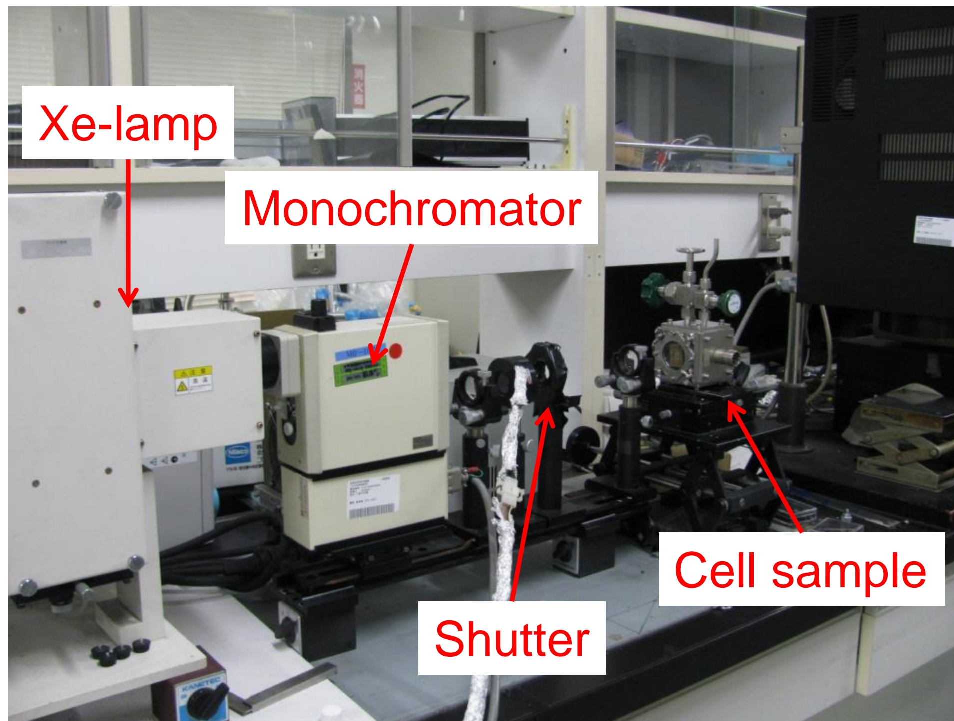

Fig. 2.3.4.3 Action spectrum measurement system.

2.3.5. Thin-film Structures

Thin film structures were observed using an optical microscope (Nikon, ECLIPSE ME600) and an Atomic Force Microscope (AFM) (Seiko Instruments, SPI3800) as shown in Fig. 2.3.5.1. The AFM images were measured using a rhodium micro cantilever (EpoLead, SI-DF3-R) in dynamic mode with a resonant frequency of 25 kHz. In addition, the crystal structures were characterized by Grazing Incidence X-ray Diffraction (GIXD) (Rigaku, D/MAX RAPID II) using CuKα radiation generated by a voltage of 40 KV with a current of 30 mA as shown in Fig. 2.3.5.2.[14] Most of the samples for this were prepared on quartz substrates without electrodes.

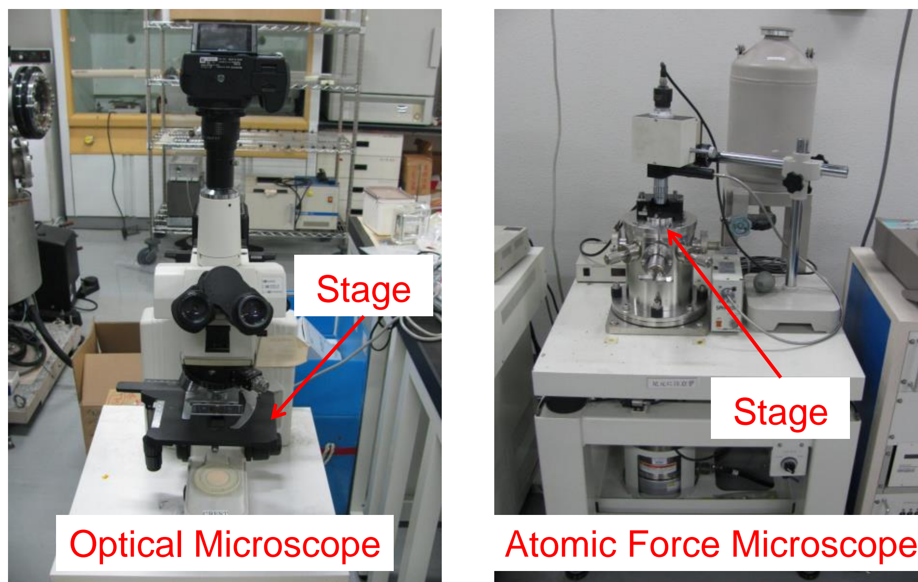

Fig. 2.3.5.1 Optical Microscope and AFM used for the measurements.

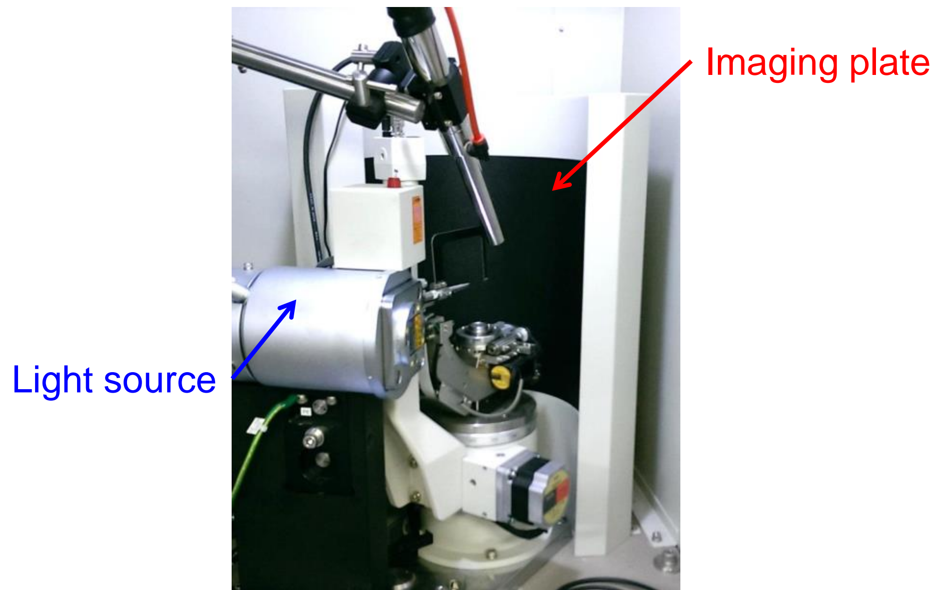

Fig. 2.3.5.2 GIXD measurement system.

2.4. References

1) R.A. Laudise, Ch. Kloc, P.G. Simpkins, and T. Siegrist, *J. Cryst. Growth.*, **187**, 449 (1998).

2) M. Hiramoto, M. Kubo, Y. Shinmura, N. Ishiyama, T. Kaji, K. Sakai, T. Ohno, and M. Izaki, *Electronics.*, **3**, 351 (2014).

3) J. Endo, T. Matsumoto, and J. Kido, *Jpn. J. Appl. Phys.*, **41**, 358 (2002).

4) Y. Shinmura, Y. Yamashina, T. Kaji, and M. Hiramoto, *Appl. Phys. Lett.*, **105**, 183306 (2014).

5) M. Kubo, Y. Shinmura, N. Ishiyama, T. Kaji, and M. Hiramoto, *Mol. Cryst. Liq. Cryst.*, **581**, 13 (2013).

6) M. Kubo, T. Kaji, and M. Hiramoto, *Appl. Phys. Lett.*, **103**, 263303 (2013).

7) X. Zeng, L. Wang, L. Duan, and Y. Qiu, *Crystal Growth & Design.,* **8**, 1617 (2008).

8) V. Podzorov, E. Menard, J. A. Rogers, and M. E. Gershenson1, *Phys. Rev. Lett.*, **95**, 226601 (2005).

9) J. Takeya, K. Tsukagoshi, Y. Aoyagi, T. Takenobu and Y. Iwasa, *Jpn. J. Appl. Phys.*, **44**, 1393 (2005).

10) K. Noda, A. Sugawara, T. Wakahiki, K. Okamoto, T. Kiyosu, K. Matsushige, and Y. Wada, *IEEJ Trans. EIS.*, **132**, 1398 (2012).

11) M. Kubo, Y. Shinmura, N. Ishiyama, T. Kaji, and M. Hiramoto, *Appl. Phys Express.*, **5**, 092302 (2012).

12) Y. Shinmura, T. Yoshioka, T. Kaji, and M. Hiramoto, *Appl. Phys Express.*, **7**, 071601 (2014).

13) Physics of Organic Semiconductors, W. Brutting, edited by WILEY-VCH Verlag

GmbH & Co. KGaA, Chapter 3 (2005).

14) M. Izaki, T. Saito, T. Ohata, K, Murata, B. M. Fariza, J. Sasano, T. Shinagawa, and S. Watase, *ACS Appl. Mater.*, **4**, 3558 (2012).

Chapter 3:

Hall effect in Doped Organic Single Crystals

"Hall effect in doped organic single crystals", Chika Ohashi, Yusuke Shinmura, Seiji Watase, Masanobu Izaki, Hiroyoshi Naito, Seiichiro Izawa, and Masahiro Hiramoto, *Adv. Mater.,* DOI: 10.1002/adma.201605619.

Abstract

The standard technique to separately and simultaneously determine the carrier concentration per unit volume (N, cm^{-3}) and the mobility (μ) of doped inorganic single crystal is to measure the Hall effect. However, this has not been reported for doped organic single crystal. Here, we report on the Hall effect measurements in doped single crystal organic semiconductors. A key feature of this work is the ultra-slow co-deposition technique reaching as low as 10^{-9} nm s^{-1}, which enables us to dope homoepitaxial organic single crystal with acceptors at extremely low concentrations down to 1 ppm. Both the hole concentration per unit volume (N, cm^{-3}) and the Hall mobility (μ_H) of doped rubrene single crystal, which has a band-like nature, were systematically observed. We found that the rubrene single crystal had (i) a high ionization rate and (ii) scattering effects due to lattice disturbances, which are peculiar to this organic single crystal.

3.1. Introduction

Doping is indispensable for organic semiconductor devices such as photovoltaic cells[1-3] and field-effect transistors (FET)[4-6]. Recently, the effects of ultralow doping of vacuum deposited organic semiconductor films have been reported.[7-9] We previously reported the effects of doping at concentrations down to 1 ppm in organic photovoltaic cells with simple *pn*-homojunctions.[10] We think that in order to precisely clarify the nature of the doping effects, doping organic single crystal without grain boundaries is necessary.

A key feature of this work is an ultra-slow co-deposition technique reaching 10^{-9} nm s^{-1}, which allows the successful doping of acceptors at extremely low concentrations down to 1 ppm in organic single crystal.

For doped inorganic single crystal, making Hall effect measurements is a standard technique, and is used to separately and simultaneously determine the carrier concentration per unit volume (N, cm^{-3}) and the mobility (μ).[11] However, there haven't been any reports of these measurements being made on doped organic single crystal. Fortunately, the Hall voltage of undoped rubrene single crystal, which possesses band-like transport properties, has been measured with the assistance of trap-healing[12] and gate bias using a FET.[13,14] We expected that if doped rubrene single crystal could be fabricated, the Hall voltage could be measured. It should be noted that, in the case of doped organic single crystal, the carrier concentration per unit volume (N, cm^{-3}) should be determined, though, so far, attention has been paid only to the carrier concentration per unit square ($N_{\square}$, cm^{-2}).

In this chapter, we report on a demonstration of Hall effect measurements in doped homoepitaxial rubrene single crystal. This sample was fabricated by

homoepitaxial growth on rubrene single crystal substrates. The homoepitaxial layer can be grown at a slow evaporation rate[15] and can be doped by means of the co-deposition technique.[3] For the lowest doping concentration of 1 ppm, we developed an extremely slow evaporation rate of 10^{-9} nm s^{-1}. Iron chloride ($FeCl_3$) was used as the acceptor dopant.

3.2. Experimental

3.2.1. Homoepitaxial Cells

Rubrene single crystal (Tokyo Chemical Industry) was grown by physical vapor transport in N_2 (0.1 atm) using train sublimation apparatus (EpiTech Inc.).[16,17] The typical thickness of the samples was around 5 μm. Fig. 3.3.1(a) shows an optical microscope image of a device used for Hall effect measurements. Four square 50 nm-thick Au electrodes in a van der Pauw configuration were deposited on the rubrene single crystal. The gaps between the electrodes are 50 μm.[18] The electrodes are arranged parallel to the a- and b-axes at the (001) surface.[19]

Fig. 3.3.1(c) shows a cross section of the device. In order to grow homoepitaxial films on the single crystal substrate, rubrene was deposited at a low evaporation rate of 3.3×10^{-3} nm s^{-1} at room temperature[15] using an oil-free vacuum evaporator (EpiTech Inc., ETVP-VG 100-SP) housed in a glove box (EpiTech Inc., 12ET12007). The typical thickness was 20 nm. 10 nm thick vacuum deposited p^+-rubrene films heavily doped with $FeCl_3$ at a concentration of 10000 ppm were inserted between the Au electrodes and the crystal (Fig. 3.3.1(c)).

3.2.2. Hall effect Measurements

A Hall effect / specific resistance measurement system (Toyo Corp., ResiTest 8300) was employed. The Hall voltage (V_H) was measured (Solartron S1 1253 Gain-phase-analyzer) while supplying a constant current of 0.10 μA (Keithley 6514). An AC magnetic field with an amplitude of ±1 T and a frequency of 10 mHz, generated by an electromagnet (Kepco Power Supply BOP36-28MG), was applied perpendicularly to the device surface. Based on the contact size effect for van der Pauw method (Reference 20), the correction factor for Hall voltage of 1.10 was obtained and used for N value calculation (Fig. 3.3.5(b)). Conductivity measurements using van der Pauw configuration were performed by supplying a constant current (Keithley 6514) while measuring the voltage (Keithley 2000). Independently, observed conductivity values were double checked by using the device in Fig. 3.3.5(b). All the measurements were performed in the dark at room temperature. The doped rubrene films were prevented from exposure to air at any time, both during fabrication and Hall measurements.

3.2.3. Single Crystal Doping

A 'Two component co-evaporation' technique was employed to dope the rubrene films. $FeCl_3$ (Sigma-Aldrich, 99.99%)[21,22] was used for the acceptor dopant. The $FeCl_3$ doping concentrations were varied, i.e., 0, 1, 10, 50, 100, 500 and 1000 ppm. A doping concentration of 1000 ppm corresponds to a molecular doping ratio (MR) of 8 x 10^{-3}. Due to the low evaporation rate of rubrene (3.3 x 10^{-3} nm s^{-1}), sophisticated evaporation techniques needed to be adopted for the ppm $FeCl_3$ doping levels. Precise monitoring of the deposition rate using a quartz crystal microbalance equipped with a computer monitoring system (ULVAC, CRTM-9000G/Depoview) allowed us to introduce dopants down to very low concentrations of 1000 ppm by volume, which corresponds to a $FeCl_3$ deposition rate of 3.3 x 10^{-6} nm s^{-1}. Doping concentrations of 500, 100, 50, 10 and 1 ppm were realized by reducing the dopant evaporation rate using rotating disks with slits with aperture ratios of 1:2, 1:10, 1:20, 1:100 and 1:1000, respectively. Since the acceptor molecule (iron chloride) has the structure of $Cl_2(Fe)Cl_2(Fe)Cl_2$ (Fe_2Cl_6), the doping efficiency was calculated as the ratio of the number of carriers (N) created to that of the Fe_2Cl_6 molecule.[23] The morphologies of the doped rubrene films were observed by Atomic Force Microscopy (AFM) (Seiko Instruments, SPI3800) using a rhodium micro cantilever (EpoLead, SI-DF3-R) in dynamic mode with a resonant frequency of 25 kHz. The crystal structures of the films were characterized by Grazing Incidence X-ray Diffraction (GIXD) (Rigaku, D/MAX RAPID II)[24] using CuKα radiation operated at 40 kV and 30 mA.

3.3. Results and Discussion

3.3.1. Doped Homoepitaxial Layer

Fig. 3.3.1(b) shows an AFM image of a 100 ppm $FeCl_3$ doped rubrene film on a rubrene single crystal substrate. The slow deposition rate of 3.3 x 10^{-3} nm s^{-1} gave rise to homoepitaxial rubrene. That is, the morphology of the deposited film showed many hexagonal structures oriented in the same direction. These tiny hexagonal structures have identical shapes to those of (001) rubrene single crystal with angles of 116° and 127° (Fig. 3.3.1(a), blue lines). The observed step height of 1.3 nm from the cross sectional profile (Fig. 3.3.1(b)) corresponds to a monomolecular step.[15,19) These observations made on doped rubrene films match those made on undoped films. Irrespective of whether they were doped or not, the single crystalline films were formed on single crystal. Observation of the thickness dependence revealed that, beneath these structures there were homoepitaxial single crystal monomolecular films of linked hexagons oriented in the same direction. Grazing Incidence X-ray Diffraction (GIXD) showed that clear out-of-plane and in-plane diffraction spots appeared at the same positions both for the rubrene layer with $FeCl_3$ doping (1000 ppm) and for that without doping (Figure 3.3.4.2). These results suggest that dopant molecules are present in the rubrene single crystal lattice. Thus, we conclude that $FeCl_3$-doped homoepitaxial rubrene single crystal was formed.

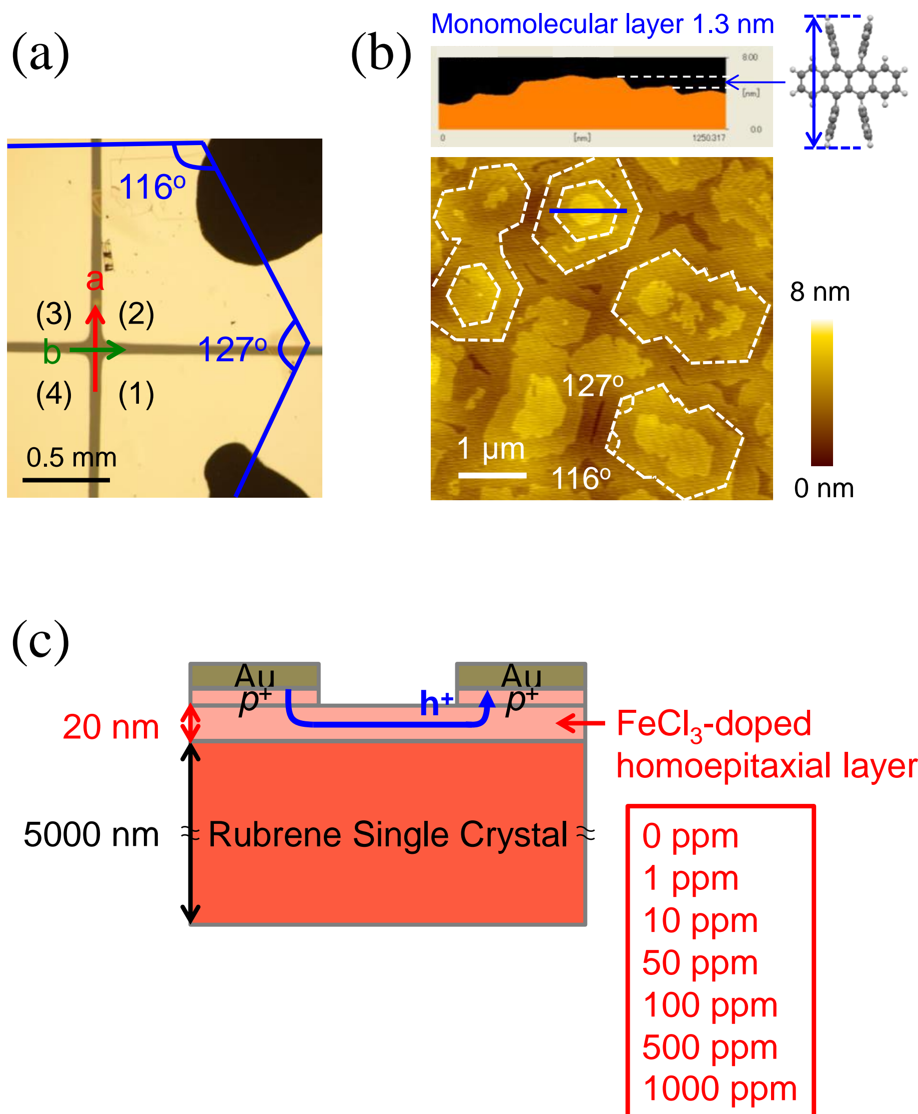

Fig. 3.3.1 (a) Photograph of a device with four van der Pauw electrodes aligned to the a- and b-axes on the (001) surface of the rubrene single crystal. The gaps between the electrodes are 50 μm wide. The (001) surface is characterized by two angles of 127° and 116°. (b) AFM image and profile of a cross section through the 100 ppm-$FeCl_3$ doped homoepitaxial rubrene layer. (c) Cross sectional structure of the device. The homoepitaxial layer (20 nm) grown on the rubrene single crystal was doped with various concentrations of acceptors ($FeCl_3$).

3.3.2. Hall Signal

On applying a magnetic field to the $FeCl_3$-doped homoepitaxial layer, voltage signals were detected, as shown in Fig. 3.3.2(a). Though the magnitudes of the voltage signals are only 0.059 and 0.065 mV for undoped and 1 ppm doped devices, respectively, there is a sharp increase by a factor of 40 to 2.5 mV for the 10 ppm doped device. Then, there is a systematic decrease to 0.37, 0.11, 0.092 and 0.073 mV for the 50, 100, 500 and 1000 ppm doped devices, respectively. The sine waves of the AC magnetic field (blue curves) and the voltage signals (red curves) are clearly synchronized. Moreover, the polarity of the voltage is inverted when the magnetic field is inverted. As shown in the inset on the upper left in Fig. 3.3.2(a), when the direction of the magnetic field is perpendicular to the plane, directed into the paper (positive magnetic field) and the direction of the current (blue line) is from electrode (1) to electrode (3), positive charge is deflected to the left due to the Lorentz force (green curves) and a transverse Hall voltage with negative polarity at electrode (4) and positive polarity at electrode (2) appears in the equilibrium state. As shown in the lower left inset in Fig. 3.3.2(a), when the direction of the magnetic field is reversed (negative magnetic field) without changing the direction of current, the Hall voltage changes direction. Thus, the AC magnetic field and AC Hall voltage are in-phase. On the other hand, as shown in the lower and upper right insets in Fig. 3.3.2(a), when the direction of the current is reversed, the AC Hall voltage is out-of-phase. The observed V_H is in proportion to B for all doping concentrations and the four combinations of magnetic field and current direction are shown in the insets (i) - (iv) in Fig. 3.3.2(a), which correspond to the quadrants (i) - (iv) in Fig. 3.3.2(b). When current was applied between electrodes (2) and (4), transverse voltage signals appeared between electrodes

(1) and (3), and fundamentally the same results were observed. These observations clearly prove that the observed voltage signals are caused by the Hall effect. In addition, all the results can be explained consistently only when the charge responsible for the current is positive, that is, the carriers in these devices are recognized as being holes. This correlates with the fact that $FeCl_3$ is an acceptor dopant. *p*-type character for undoped sample is originated from the rubrene single crystal substrate itself (Fig. 3.3.5 (c)).

The Hall coefficient for a unit volume (R_H, cm^3C^{-1}) can be expressed by the following equation;

$$R_H = V_H d / IB \qquad (3.3.2.1)$$

where d is the effective thickness of the device. R_H is directly related to the hole concentration per unit volume (N, cm^{-3}) as in the following equation;

$$N = 1 / R_H e \qquad (3.3.2.2)$$

Combining equations (3.3.2.1) and (3.3.2.2), we obtain the following expression for V_H;

$$V_H = IB / Ned \qquad (3.3.2.3)$$

The magnitude of the Hall voltage (V_H) increases substantially from 0.059 to 2.5 mV by introducing a 10 ppm doped layer (Fig. 3.3.2(a)). Since the magnitude of V_H should decrease by increasing the hole concentration (N), the observed enormous

increase in V_H can't be attributed to the introduction of holes, i.e., the increase in N. Thus, we concluded that it must be due to a decrease in d.

In the case of 0 ppm (undoped), the carriers (holes) clearly can't distinguish between the homoepitaxial layer and the rubrene substrate since they are both single crystal. Since the position of the Fermi level (E_F) measured by Kelvin probe for the 1 ppm doped rubrene film (4.73 eV) was confirmed as being close to that of the undoped (0 ppm) one (4.69 eV), holes also can't distinguish between these. In these cases, the carriers can diffuse throughout the bulk of the crystal. At 10 ppm, since E_F has shifted positively to 5.02 eV, an energy barrier was formed at the interface between the homoepitaxial layer and the rubrene substrate due to the significant energy difference (0.33 eV). Thus, holes can distinguish between these and are confined to the 20 nm thick doped homoepitaxial layer. The effective thickness for the Hall measurements (d) can be regarded as the thickness of the material where carriers are present. Thus, we conclude that d is equal to the thickness of the doped layer (20 nm). The sudden decrease of d from the total crystal thickness (5 μm) to 20 nm induces the jump in V_H at 10 ppm.

V_H systematically decreases with increasing doping concentration above 10 ppm. This can be explained by the increase in hole concentration (N) in equation (3). So, the values of N can be calculated exactly. For example, in the case of 10 ppm doping, $R_H = 5.6 \times 10^2$ cm^3C^{-1} and $N = 1.1 \times 10^{16}$ cm^{-3} were obtained when using $I = 1.0 \times 10^{-7}$ A, B = 1 T and d = 20 nm.

It should be noted that in previous studies on Hall effect measurements for organic single crystal combined with a field-effect transistor[13,14], the carrier concentration per unit square ($N_{\square}$, cm^{-2}) together with the Hall coefficient per unit

square ($R_{H\square}$, cm^2C^{-1}) were discussed. However, from the standpoint of the chemical doping, by taking account of the effective thickness of the active layer (d) in making the Hall measurement, it is the number of holes per unit volume (N, cm^{-3}) together with the Hall coefficient per unit volume (R_H, cm^3C^{-1}) that should be considered.

The Hall mobility (μ_H) can be calculated from the following equation;

$$\mu_H = \sigma R_H \qquad (3.3.2.4)$$

where σ is the carrier conductivity. For example, $\mu_H = 4.6$ $cm^2V^{-1}s^{-1}$ and $\sigma = 6.0 \times 10^{-2}$ Scm^{-1} were determined at 10 ppm doping. It should be noted that although the effective thickness of the devices (d) isn't needed to obtain the Hall mobility (μ_H), we should know where the current flows. In the present system, since the current is through the doped layer, it is expected that μ_H will be influenced by the dopant ions.

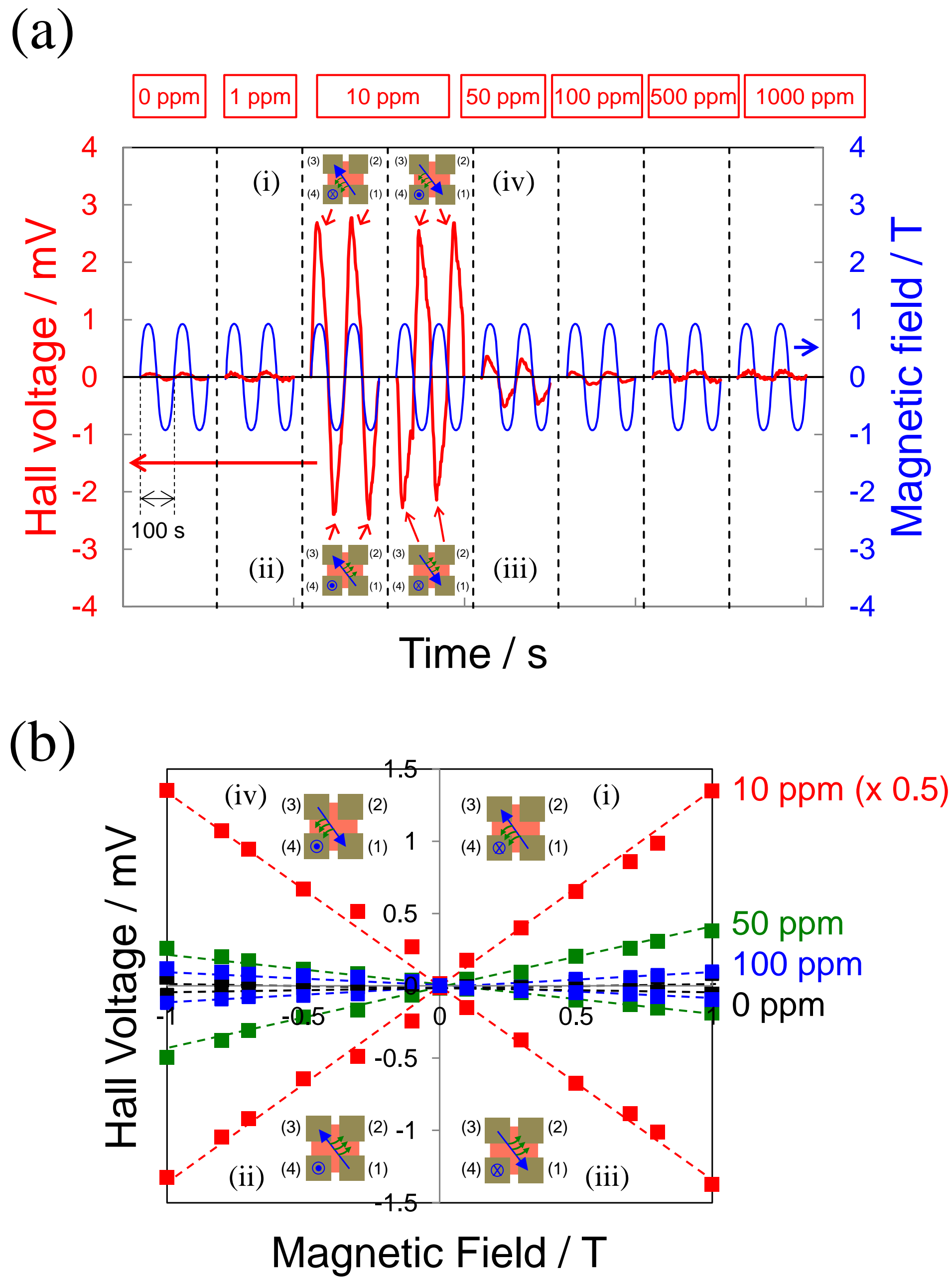

Figure 3.3.2 (a) Hall voltage signals when applying an AC magnetic field for doping concentrations of 0, 1, 10, 50, 100, 500, and 1000 ppm. (b) Dependence of the Hall voltage on the magnetic field. The black, red, green, and blue squares correspond to 0, 10, 50, and 100 ppm, respectively.

3.3.3. Hole Concentration and Hall Mobility

Thus, we succeeded in simultaneously measuring the hole concentration per unit volume (N, cm^{-3}) and the Hall mobility (μ_H) in a doped organic single crystal by means of the Hall effect. The effects of doping on N and μ_H for organic single crystal possessing inherent band-like features haven't previously been observed. Two unique observations peculiar to the single crystal were observed. These were (i) a high ionization rate, and (ii) scattering effects due to lattice disturbances.

(i) High ionization rate : The doping efficiencies of single crystal and amorphous films of rubrene were compared. The rubrene single crystal reached a maximum value of 24% at 100 ppm (Fig. 3.3.3(b), red solid curve) which is significantly larger than that of 1.2% for the amorphous film formed by vacuum deposition (Fig. 3.3.3(b), blue solid curve) (Figure 3.3.4). We presume that the ionization rate is dominated by the density of hole traps. Since there are a vast number of gap states in amorphous film, most of the holes created by doping are captured. On the other hand, the high ionization rate of 24% was obtained because fewer holes are captured by the relatively small number of hole traps present in the single crystal. The increase in ionization rate from 1 to 100 ppm can be attributed to trap-filling[7-9], i.e., the filling of traps by the holes created, which gives a similar effect to trap-healing[12] and decreases the effective trap concentration. On the other hand, the increase in trap density above 100 ppm due to the lattice disturbance mentioned below causes a decrease in the ionization rate.

(ii) Scattering effects due to lattice disturbance : A decrease in Hall mobility (μ_H) above 10 ppm was observed. Since holes captured by traps can not move under the

influence of the Lorentz force, μ_H contains no contribution from the trapped holes. So, the decrease in μ_H can be directly assigned to the scattering effects. The homoepitaxial hexagonal structures (Fig. 3.3.1(b)) became gradually more disordered above 100 ppm as shown in the AFM images (Figs 3.3.4.1(b) and (c)). The GIXD results also suggest that, for doped homoepitaxial layers, there seem to be plural states of the dopant molecule in the distorted homoepitaxial rubrene phases with slightly different lattice constants (Figure 3.3.4.2). Thus, we speculate that the gradual decrease in μ_H can be attributed to hole scattering by doping induced lattice disturbances such as lattice distortion due to the substitution of rubrene molecules with ionized and neutral dopant molecules and the formation of various types of defects such as dopant inserted at interstitial positons, the formation of doping induced vacancies, etc.

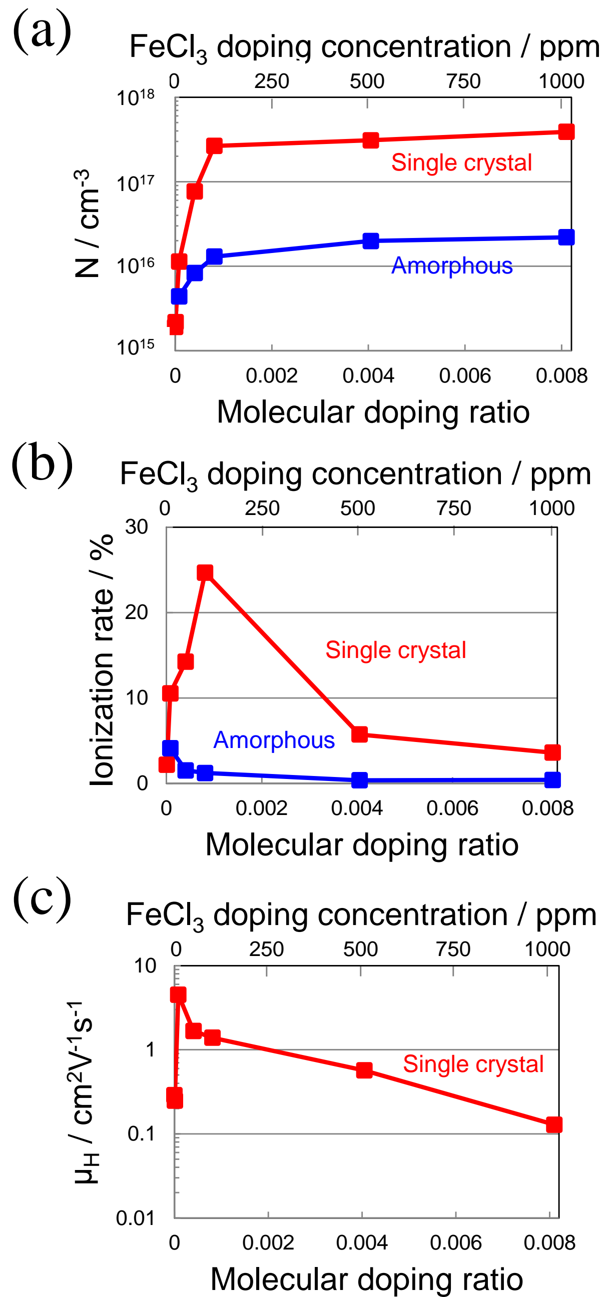

Figure 3.3.3 Dependences of (a) the hole concentration per unit volume (N, cm^{-3}), (b) the ionization rate, and (c) the Hall mobility (μ_H) on the molecular doping ratio (MR) and the $FeCl_3$ doping concentration by volume for doped single crystal (red curves). For comparison, the results for N and the ionization rate for vacuum deposited amorphous films are also shown (blue curves).

3.3.4. AFM and GIXD for Doped Single Crystals

The hexagonal structures of homoepitaxial rubrene layer were not affected so much by 100 ppm doping. On the other hand, the homoepitaxial hexagonal structures (Figure 3.3.4.1 (a)) became to be disordered gradually from 100 to 1,000 ppm.

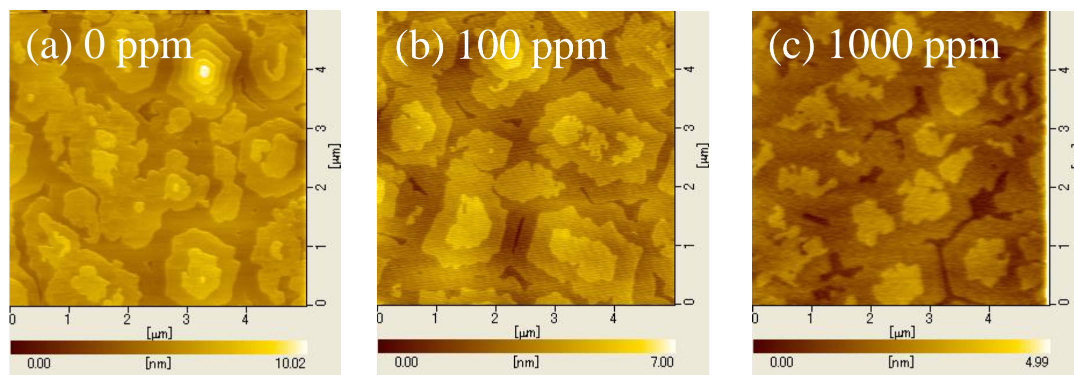

Figure 3.3.4.1 AFM images for homoepitaxial rubrene layer under the various doping concentration. (a), (b), and (c) correspond to the doping concentrations of 0, 100, and 1,000 ppm, respectively.

The angle of incidence of the X-rays was 3° to the crystal surface. The transmitted X-ray diffraction pattern for the undoped (0 ppm, (a)) sample is also shown. The angle of incidence of the X-rays was 90° to the crystal surface.

Clear transmitted X-ray diffraction spots were observed for the undoped rubrene layer on rubrene single crystal (Figure 3.3.4.2 (a)). In the case of the GIXD measurements, clear out-of-plane (θ direction) and in-plane (β direction) diffraction spots appeared at the same positions both for the rubrene layer with $FeCl_3$ doping (1000 ppm) and for that without doping although there was a halo due to the quartz substrate (Figure 3.3.4.2 (b) and (c)). Enlarged images of each spot revealed that they split into four only for the doped layer (see the enlarged rectangular blue area). For the undoped rubrene layer, such splitting was not observed. These results suggest that the diffraction spots come from the 20 nm thick rubrene layer. Thus, we concluded that the doped rubrene layers were homoepitaxially grown on the single crystal substrates, i.e., the doped vacuum deposited rubrene layers are single crystal. In addition, there appears to be a plurality of states of the dopant molecule in distorted homoepitaxial rubrene phases with slightly different lattice constants. For the various states of the dopant molecule, substitution of rubrene molecules, insertion at interstitial positions, the formation of doping induced vacancies, etc. might be considered.

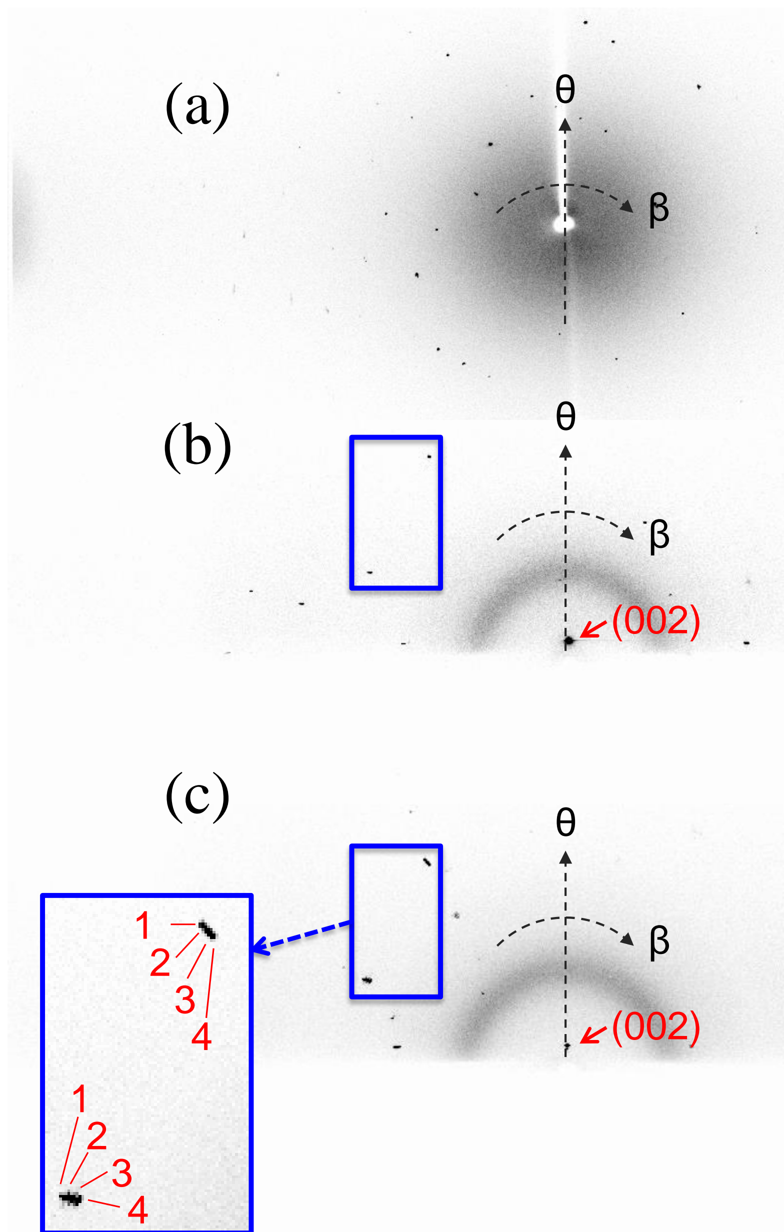

Figure 3.3.4.2 Grazing Incidence X-ray Diffraction (GIXD) for undoped (0 ppm, (b)) and $FeCl_3$-doped (1000 ppm, (c)) homoepitaxial rubrene layers on rubrene single crystal.

3.3.5. Contact Size Effect

Sheet conductivity ($\sigma_{\square}$) was independently measured by using the device of Fig. 3.3.5(a). Under the application of the constant current (I) of 10^{-7} A, voltage (V) was measured in the order between electrodes (1)-(2), (2)-(3), (3)-(4), and (4)-(1). $\sigma_{\square}$ was calculated by the equation (3.3.5.1).

$$\sigma_{\square} = (I/V)(L/W) \qquad (3.3.5.1)$$

Averaged values of $\sigma_{\square}$ for samples having different doping concentrations are shown in Table 3.3.5.1 together with the values measured by the van der Pauw method. Calculated values of mobility were confirmed to be little difference irrespective of the measuring methods of $\sigma_{\square}$.

We estimated the active contact size by means of device simulation (Atlas, Silvaco).[25] Electric field is only distributed within 10 μm from the edge of electrodes ((2)-(4) or (1)-(3)) (Fig. 3.3.5(b)). Since the electrode size (δ) can be regarded 10 μm (Fig. 3.3.6(b) inset), contact size ratio (δ/l) is 10 μm/90 μm = 0.11. Based on the contact size effect for van der Pauw method (Reference 20), the correction factor for Hall voltage of 1.10 was obtained and used for N value calculation.

We confirmed that without the excitation current, no Hall voltage was observed. So, the possibility of the induction effect[26] can be excluded.

Rubrene single crystals without and with undoped rubrene homoepitaxial layer (20 nm) homoepitaxial layer showed the Hall voltages of 0.052 mV and 0.059 mV, respectively (Fig. 3.3.5(c)). Since the magnitude of Hall voltage was not changed irrespective of the existence of homoepitaxial layer, we assume that the observed *p*-type

character is originated from the rubrene single crystal substrate itself. We suspect the quality of single crystal is not perfect, such as the existence of molecular defects at the surface or in the bulk and adsorbed oxygen at the crystal substrate surface before depositing homoepitaxial layer, etc, which may act as the acceptor impurities. We expect that the N value for undoped organic single crystals would be decreased by developing the method to make perfect organic crystals. In the present study, *p*-type character of crystal substrate is very weak, therefore, the doped homoepitaxial rubrene layers dominate the experimental results.

Table 3.3.5.1 Comparison between $\sigma_{Fig.\ S5(a)}$ and $\sigma_{van\ der\ Pauw}$

Doping concentration / ppm	Sheet conductivity ($\sigma_{\square}$, Scm^{-2})	
	$\sigma_{Fig.\ S5(a)}$	$\sigma_{van\ der\ Pauw}$
0	2.6 x 10^{-8}	3.6 x 10^{-8}
1	3.0 x 10^{-8}	4.3 x 10^{-8}
10	1.4 x 10^{-8}	1.6 x 10^{-8}
50	3.9 x 10^{-8}	4.1 x 10^{-8}
100	1.1 x 10^{-7}	1.2 x 10^{-7}
500	3.6 x 10^{-8}	5.6 x 10^{-8}
1000	1.4 x 10^{-8}	1.6 x 10^{-8}

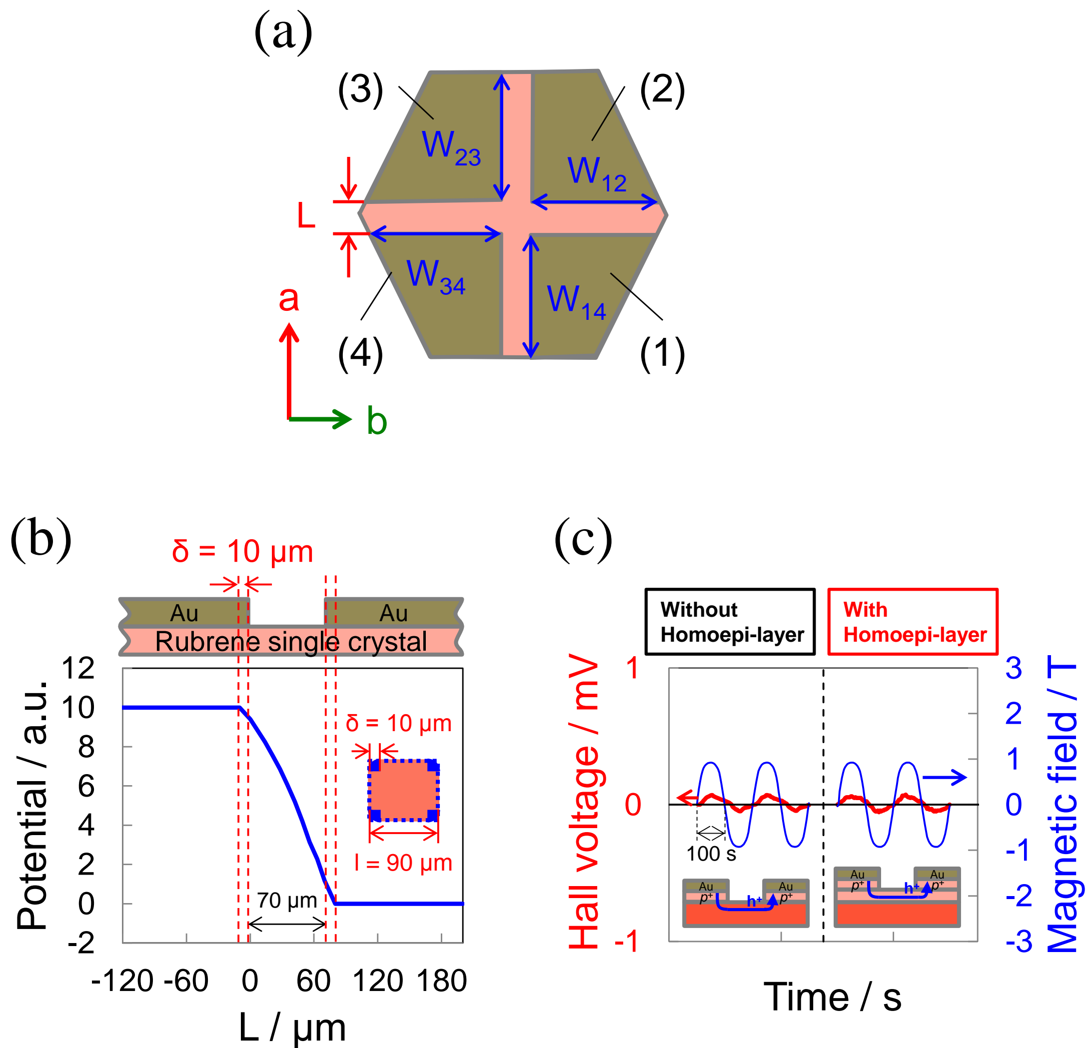

Fig. 3.3.5 Device configuration for the sheet conductivity ($\sigma_{\square}$) measurements. Obtained $\sigma_{\square}$ values are also shown in Table with those obtained by van der Pauw method. (b) Distribution of potential appeared between two electrodes ((2)-(4) or (1)-(3)) calculated by device simulation. Configuration of van der Pauw electrodes by taking account of the active electrode size. (c) Hall signals for rubrene single crystal without homoepitaxial layer and for rubrene single crystal with undoped rubrene homoepitaxial layer (20 nm).

3.3.6. Doped Amorphous Films

Since Hall effect measurements can not be applied to $FeCl_3$-doped vacuum deposited rubrene films due to the hopping nature of its carrier transport, the hole concentration was determined by Kelvin band-mapping. The vacuum deposited rubrene film was confirmed to be amorphous because no diffraction peaks were observed by XRD (Fig. 3.3.6(c)). The vacuum deposited rubrene film was confirmed to be amorphous because no diffraction peaks were observed by XRD. $FeCl_3$-doped amorphous rubrene films were deposited on ITO electrodes and the dependence of the work function on the film thickness was measured by Kelvin probe.

The black, red, orange, yellow, green, blue and purple curves correspond to the change of work function with film thickness for 0, 1, 10, 50, 100, 500, and 1000 ppm doped films, respectively. The width of the depletion layer (W_{dep}) and the built-in potential (V_{bi}) can be determined from the point (shown by arrows) at which band bending ends. For example, W_{dep} = 200 nm and V_{bi} = 0.4 V were obtained at a doping concentration of 10 ppm. N can be calculated using the following equation;

$$N = 2\varepsilon\varepsilon_0 V_{bi}/eW_{dep}^2 \qquad (3.3.6.1)$$

where, ε, ε_0 and e are the relative dielectric constant, the dielectric constant in vacuum, and the elementary charge, respectively. For 10, 50, 100, 500, and 1000 ppm, N and the ionization rate were calculated to be 4.4×10^{15} (4.1%), 8.3×10^{15} (1.5%), 1.3×10^{16} (1.2%), 2.0×10^{16} (0.37%), and 2.2×10^{16} cm^{-3} (0.42%), respectively.

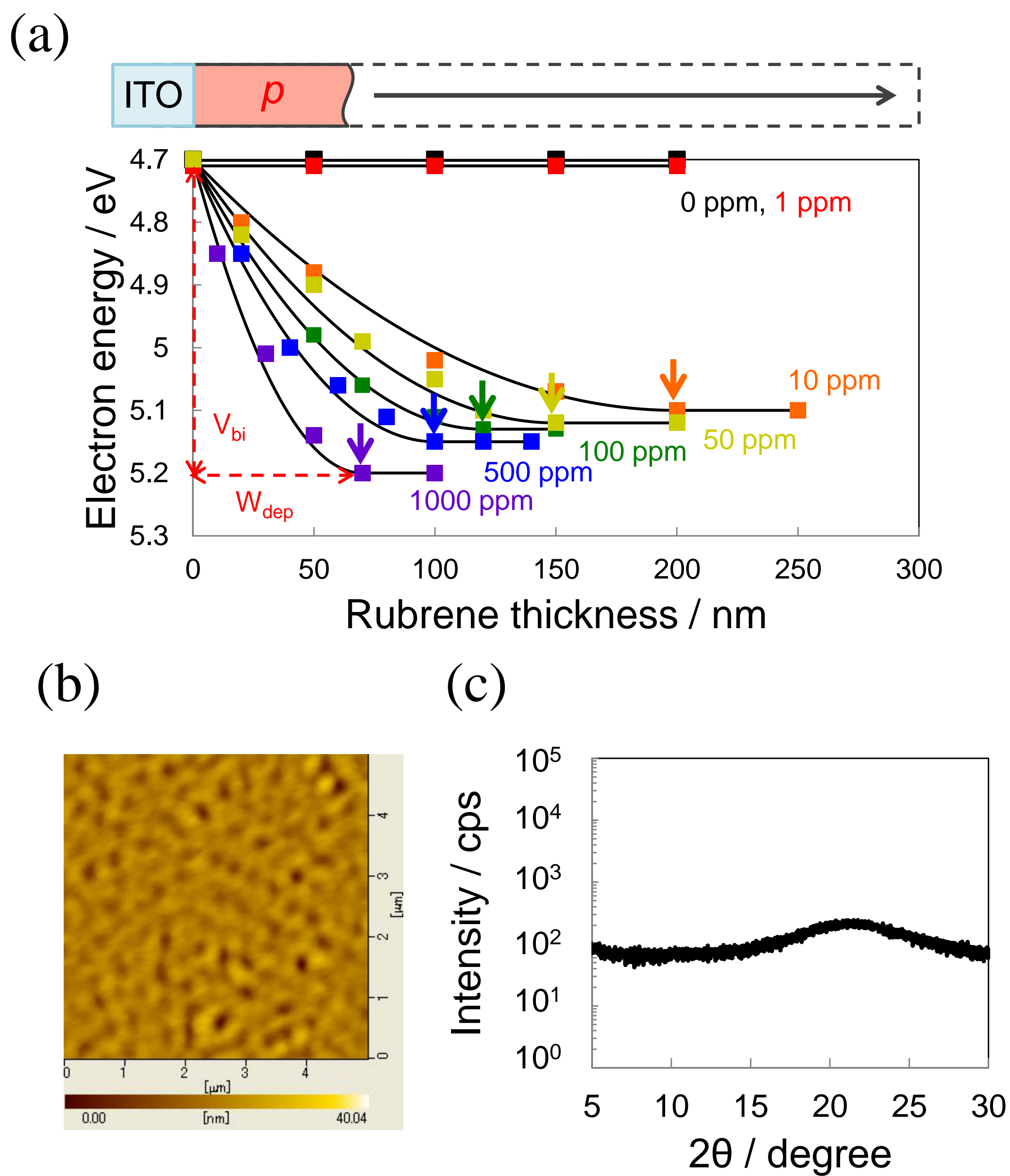

Figure 3.3.6. (a) Kelvin band-mapping for $FeCl_3$-doped amorphous rubrene films which were vacuum-deposited on ITO glass substrate. (b) AFM image and (c) XRD pattern for the 100 ppm $FeCl_3$-doped amorphous rubrene films.

3.4. Conclusion

In this chapter, homoepitaxial rubrene single crystal doped with acceptor impurities of extremely low concentration (1~1,000 ppm) was fabricated by developing an ultra-slow co-deposition technique reaching 10^{-9} nm s^{-1}. Systematic measurements of both the hole concentration (N) and the Hall mobility (μ_H) in this material were made by making Hall effect measurements. High ionization rates and scattering effects due to lattice disturbances, which are peculiar to organic single crystal, were observed.

3.5. References

1) E. S. Henze, V. G. Lyssenko, J. Fischer, M. Tietze, R. Brueckner, T. Menke, K. Leo, and M. Riede, *Org. Electron.*, **15**, 563 (2014).
2) Y. Zhang, H. Zhou, J. Seifter, L. Ying, A. Mikhailovsky, A. J. Heerger, G. C. Bazan, and T. Q. Nguyen, *Adv. Mater.*, **25**, 7038 (2013).
3) M. Hiramoto, M. Kubo, Y. Shinmura, N. Ishiyama, T. Kaji, K. Sakai, T. Ohno, and M. Izaki, *Electronics.*, **3**, 351 (2014).
4) B. Lussem, M. L. Tietze, H. Kleemann, C. Hobach, J. W. Bartha, A. Zakhidov, and K. Leo, *Nat. Commun.*, **4**, 2775 (2013).
5) X. Liu, D. Kasemann, and K. Leo, *Appl. Phys. Lett.*, **106,** 103301 (2015).
6) B. D. Naab, S. Himmelberger, Y. Diao, K. Vandewal, P. Wei, B. Lussem, A. Salleo, and Z. Bao, *Adv. Mater.*, **25**, 4663 (2013).
7) S. Olthof, S. Mehraeen, S. K. Mohapatra, S. Barlow, V. Coropceanu, J. L. Bredas, S. R. Marder, and A. Kahn, *Phys. Rev. Lett.*, **109**, 176601 (2012).
8) M. L. Tietze, L. Burtone, M. Riede, B. Lussem, and K. Leo, *Phys. Rev. B.*, **86**, 035320 (2012).
9) M. L. Tietze, P. Pahner, K. Schmidt, K. Leo, and B. Lussem, *Adv. Funct. Mater.,* **25,** 2701 (2015).
10) C. Ohashi, Y. Shinmura, M. Kubo, and M. Hiramoto, *Org. Electron.*, **27**, 151 (2015).
11) S. M. Sze, Physics of Semiconductor Devices, published by WILEY-INTERSCEINCE, Chapter 3 (1969).
12) B. Lee, Y. Chen, D. Fu, H. T. Yi, K. Czelen, H. Najafov, and V. Podzorov, *Nat. Mater.*, **12**, 1125 (2013).

13) V. Podzorov, E. Menard, J. A., Rogers, and M. E., Gershenson, *Phys. Rev. Lett.*, **95,** 226601 (2005).

14) J. Takeya, J. Kato, K. Hara, M. Yamagishi, R. Hirahara, K. Yamada, Y. Nakazawa, S. Ikehata, K. Tsukagoshi, Y. Aoyagi, T, Takenobu, and Y. Iwasa, *Phys. Rev. Lett.*, **98**, 196804 (2007).

15) X. Zeng, L. Wang, L. Duan, and Y. Qiu, *Crystal Growth & Design.,* **8**, 1617 (2008).

16) R.A. Laudise, C. Kloc, P. G. Simpkins, and T. Siegrist, *J. Cryst. Growth.*, **187**, 449 (1998).

17) J. Takeya, M. Yamagishi, Y. Tominari, R. Hirahara, Y. Nakazawa, T. Nishikawa, T. Kawase, T. Shimoda and S. Ogawa, *Appl. Phys. Lett.*, **90,** 1021120 (2007).

18) K. Noda, A. Sugawara, T. Watahiki, K. Okamoto, T. Kiyosu, K. Matsushige, and Y. Wada, *IEEJ Trans. EIS.*, **9**, 132 1398 (2012).

19) M. E. Helou, O. Medenbach, and G. Witte, *Crystal Growth & Design.,* **10**, 3496 (2010).

20) R. Chwang, B. J. Smith, and C. R. Crowell, *Solid-State Electron.* **17**, 1217 (1974).

21) J. Endo, T. Matsumoto, and J. Kido, *Jpn. J. Appl. Phys.*, **41**, 358 (2002).

22) Y. Shinmura, Y. Yamashina, T. Kaji, and M. Hiramoto, *Appl. Phys. Lett.*, **105**, 183306 (2014).

23) R. Kiriyama, Structural Inorganic Chemistry I, published by Kyoritsu Shuppan, Chapter 10 (1952).

24) M. Izaki, T. Saito, T. Ohata, K, Murata, B. M. Fariza, J. Sasano, T. Shinagawa, and S. Watase, *ACS Appl. Mater.*, **4**, 3558 (2012).

25) K. Takagi, S. Abe, T. Nagase, T. Kobayash, H. Naito, *J Mater Sci Mater Electron.*,

26, 4463 (2015).

26) Y. Chen, H. T. Yi, and V. Podzorov, *Phys. Rev. Applied.*, **5**, 034008 (2016).

Chapter 4:

Field-Effect Mobility of Doped Organic Single Crystals

"Field-Effect Mobility of Doped Organic Single Crystals", Chika Ohashi, Seiichiro Izawa, Yusuke Shinmura, and Masahiro Hiramoto, in preparation.

Abstract

The doping effects on carrier transport for organic single crystals were clarified by measuring the field-effect mobility. The field-effect mobility was revealed to be dominated by hole traps. The activation energy and the concentration of hole traps increased with increasing the acceptor dopant concentration. Formation of dopant-induced traps decreased the observed ionization rate of doping. Dopant-induced traps should be removed to obtain the substantial doping efficiency in organic single crystals.

4.1. Introduction

Doping is an essential requirement for organic semiconductor devices such as photovoltaic cells[1-4], field-effect transistors[5-7]. In the case of field-effect transistor (FET), the enhancements of FET performances such as a threshold voltage (V_{th}) and an on-off ratio with doping have been reported.[5,6] In addition, the effects of ultralow doping of vacuum deposited organic semiconductor films have also been reported.[8-10]

In chapter 4, we have reported on the doping single crystal rubrene at the 1 ppm level using an ultra-slow co-deposition technique with a deposition rate of 10^{-9} nm s^{-1}.[11] Moreover, we made the first ever systematic measurements of the hole concentration per unit volume (N, cm^{-3}) and the Hall mobility (μ_H) of doped rubrene single crystal using the Hall effect. We believe that by doping organic single crystals, i.e. those containing no grain boundaries, we can, potentially, clarify the nature of the doping effects. However, the doping effects on carrier transport for organic single crystals have not been reported. Based on the consideration, we attempted to measure the FET mobility for doped rubrene single crystals. For the typical device structure, we adopted a bottom-gate/top-contact type FET device (Fig. 4.3.1(a)).

In this chapter, we report on the FET mobility (μ_{FET}) of the doped rubrene single crystals. The doped rubrene single crystals were fabricated by the homoepitaxial growth on rubrene single crystal substrates. Iron chloride ($FeCl_3$) was used as the acceptor dopant. In order to reveal the doping effects, we systematically measured the doping concentration and the temperature dependences of μ_{FET} in the doped rubrene single crystals.

4.2. Experimental

Rubrene (Tokyo Chemical Industry) single crystals were grown by physical vapor transport in N_2 (0.1 atm) by using train sublimation apparatus (EpiTech Inc.).[12,13] Typical thickness of rubrene single crystals were around 5 μm. An iron chloride ($FeCl_3$) (Sigma-Aldrich, 99.99%)[14,15] was used for acceptor dopant. In order to grow the homoepitaxial rubrene single crystal films on rubrene single crystal substrate, rubrene was deposited at a low evaporation rate of 3.3 x 10^{-3} nm s^{-1} at room temperature[16] using an oil-free vacuum evaporator (EpiTech Inc., ETVP-VG 100-SP) housed in a glove box (EpiTech Inc., 12ET12007). The typical thickness was 20 nm. Figs. 4.3.1(a) and (b) shows the structure and photograph of FET of the $FeCl_3$-doped rubrene single crystals. Homoepitaxial side of rubrene single crystal were stuck together on the heavily doped n^+-Si substrates with a 300 nm thick SiO_2 layer acting as the gate dielectrics. Source-drain Au electrodes were vacuum deposited on the back side of rubrene substrate. In order to make ohmic contacts, 10 nm-thick heavily $FeCl_3$-doped (10000 ppm) p^+-rubrene layers were inserted between the Au electrodes and rubrene substrate (Fig. 4.3.1(a)). The channel width (W) and length (L) were 0.2 mm and 50 μm, respectively.

A 'Two component co-evaporation' technique was employed to dope the rubrene homoepitaxial layers. Concentration of $FeCl_3$ acting as acceptor dopant was systematically varied, i.e., 0, 1, 10, 100, and 500 ppm. Precise monitoring of the deposition rate using a quartz crystal microbalance equipped with a computer monitoring system (ULVAC, CRTM-9000G/Depoview) allowed us to introduce dopants down to the very low concentration of 500 ppm by volume, which corresponds to a $FeCl_3$ deposition rate of 1.7 x 10^{-6} nm s^{-1}. Doping concentrations of 100, 10, and 1

ppm were realized by reducing the dopant evaporation rate equivalent to 1000 ppm (3.3 x 10^{-6} nm s^{-1}) using rotating disks with slits with aperture ratios of 1:10, 1:100 and 1:1000, respectively. The doping concentration of 1 ppm corresponds to a molecular doping ratio (MR) of 8.1 x 10^{-6}.

Both the transfer and output characteristics of the FET devices were measured using a semiconductor characterization system (Keithley, 4200-SCS). These FET characteristics were measured at various temperatures (25, 35, 40, 45 and 50 ^{o}C) by heating the devices on a hotplate (Asone, CHPS-170DN). All the measurements were performed in the dark. The doped homoepitaxial rubrene single crystal was prevented from exposure to air at any time, both during fabrication and the FET measurements.

4.3. Results and Discussion

4.3.1. FET Characteristics

Figs. 4.3.1(c) and (d) show the transfer (I_{DS}-V_{GS}) and the output (I_{DS}-V_{DS}) characteristics for the 500 ppm $FeCl_3$-doped homoepitaxial rubrene single crystal at room temperature (25°C). All the FET devices exhibited the clear *p*-type characteristics. In the linear regime (Fig. 1(c)), the FET mobility (μ_{FET}) can be calculated based on the following equation (4.3.1).

$$I_{DS} = (\mu_{FET} W C_i / L) \{(V_{GS}-V_{th})V_{DS} - V_{DS}^2/2\} \quad (4.3.1)$$

where I_{DS}, C_i, V_{GS}, V_{DS}, and V_{th} are the drain-source current, the capacitance per unit area of the SiO_2 gate dielectric layer (12 nF cm^{-2}), the gate-source voltage, the drain-source voltage, and the threshold voltage, respectively. For example, at 500 ppm, μ_{FET} was calculated to be 2.3 x 10^{-3} $cm^2V^{-1}s^{-1}$. The dependence of μ_{FET} on the $FeCl_3$ doping concentration is shown in Fig. 4.3.2(c) (blue curve). Since the source–drain current (I_{DS}) flows through the organic layer neighboring the SiO_2 dielectric, the observed FET characteristics represent the properties of the doped homoepitaxial single crystal layers.

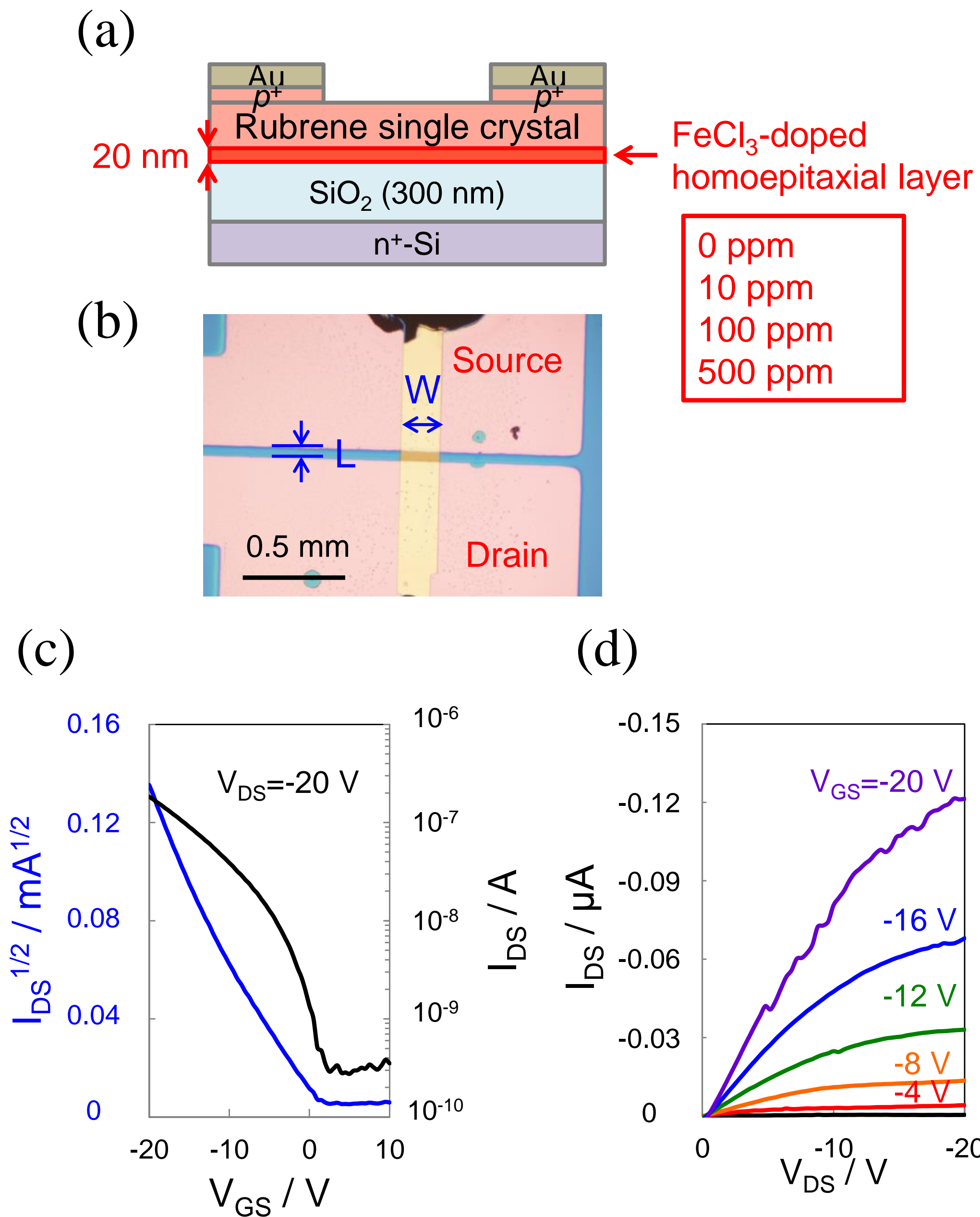

Fig. 4.3.1 (a) Structure and (b) photograph of a FET device using the $FeCl_3$-doped rubrene single crystals. (c) Transfer (I_{DS}-V_{GS}) and (d) output (I_{DS}-V_{DS}) characteristics for the 500 ppm $FeCl_3$-doped homoepitaxial rubrene single crystal at room temperature.

4.3.2. Activation Energy of Hole Traps

Fig. 4.3.2(a) shows the temperature dependence of the square root of the source-drain current ($I_{SD}^{1/2}$) for the 100 ppm-doped single crystal. The magnitude of $I_{SD}^{1/2}$ increases by a factor of 1.4 by elevating the temperature from 25 to 50 ^{o}C. This means that μ_{FET} increases with increasing temperature. The values of μ_{FET} obtained using equation (4.1) were 0.064, 0.090, 0.10, 0.11, 0.12 $cm^2V^{-1}s^{-1}$ at 25, 35, 40, 45, and 50 ^{o}C (black, red, orange, green and blue solid curves), respectively. Clearly, the FET mobility is dominated by a thermally activated process with an activation energy (E_a).

The values of FET mobility (μ_{FET}) (Fig. 4.3.2(c)) were significantly smaller compared to those of Hall mobility (μ_H) (Chapter 3, Fig. 3.3.3(c)). μ_H can be regarded as the intrinsic mobility, which is free from trapping process. μ_{FET} can be regarded as the drift mobility (μ_D), which contains the trapping process. Thus, we concluded that the observed μ_{FET} values are dominated by traps for holes. In order to determine the activation energy of traps (E_a), the observed μ_{FET} values for 0, 10, 100 ppm-doped single crystals are plotted for the reciprocal temperature (1/T) (Fig. 4.3.2(b)) since the drift mobility (μ_D) can be expressed by the following Arrhenius equation (4.3.2).

$$\mu_D \approx \mu_0 \exp(-E_a/kT) \qquad (4.3.2)$$

where μ_0, and k are the intrinsic mobility and the Boltzmann constant, respectively. Fig. 4.3.2(c) shows the dependences of E_a and μ_{FET} on the doping concentration. E_a increases from 0.11 to 0.37 eV (black solid line) while μ_{FET} decreases from 0.68 to 2.3 x 10^{-3} $cm^2V^{-1}s^{-1}$ (blue solid line) with increasing the doping concentration from 0 to 500 ppm. Since the observed E_a values are considerably deeper than 0.1 eV, which is far

greater than the thermal energy of room temperature ($kT = 0.026$ eV), eventually all the holes created through doping are captured by hole traps at room temperature.

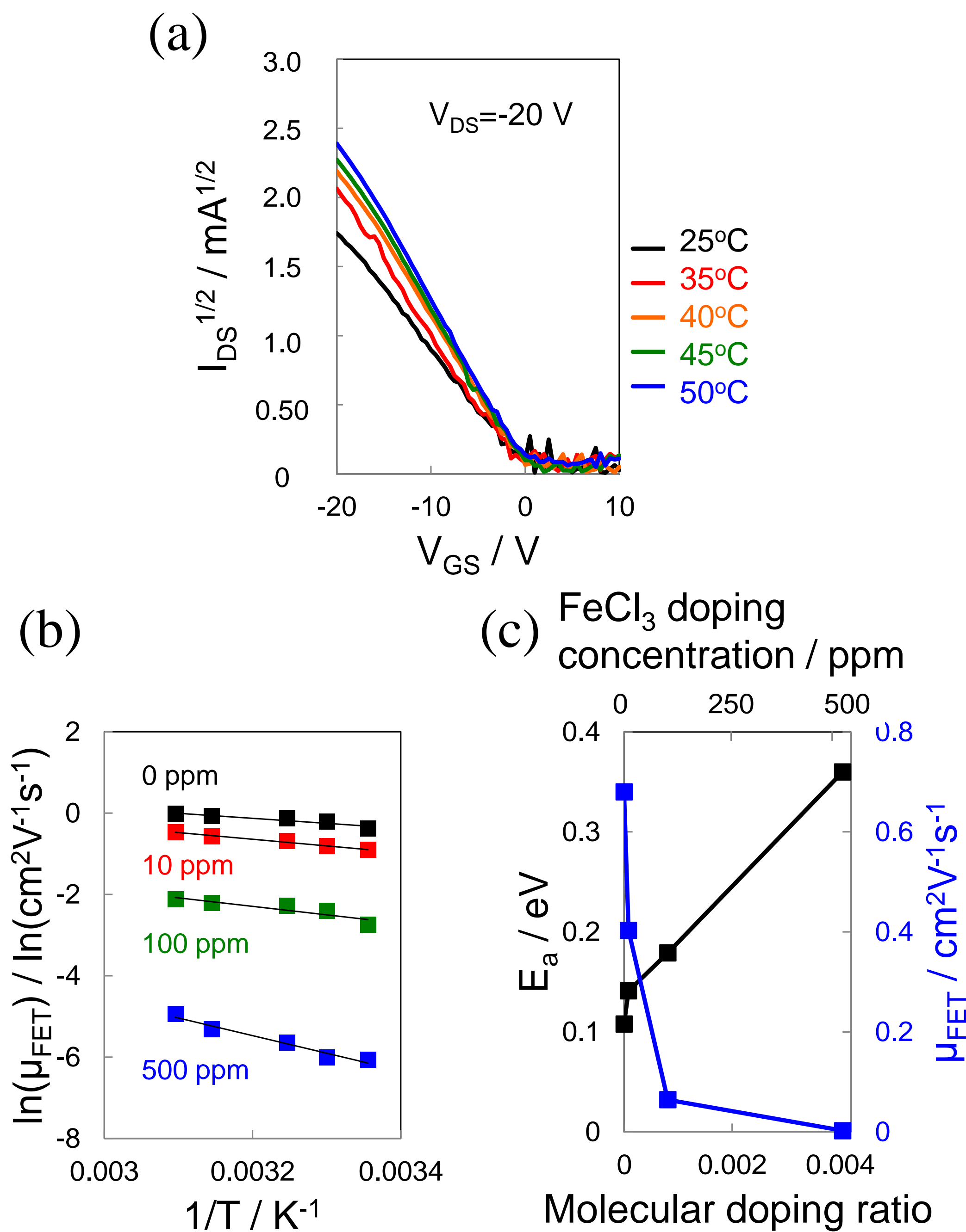

Fig. 4.3.2 (a) Temperature dependence of the square root of the source-drain current ($I_{SD}^{1/2}$) for the 100 ppm-doped single crystal. (b) Reciprocal temperature (1/T) dependence of μ_{FET} for 0, 10, 100 and 500 ppm-doped single crystals. (c) Dependences of E_a and μ_{FET} on $FeCl_3$ doping concentration.

4.3.3. Concentration of Hole traps

Figs. 4.3.3.1(a) and (b) show the dependence of hole concentration ($N_{free\ hole}$) and the ionization rate of acceptor dopant (I_{obs}) on $FeCl_3$ doping concentration, which were measured by Hall effect (Chapter 3). Strong suppression of $N_{free\ hole}$ increase above 100 ppm (Fig. 3(a)) suggests that there is a strong influence of traps capturing the created holes. Observed ionization rate (I_{obs}) obviously influenced by the concentration of traps (N_{trap}). Here, we introduce the substantial ionization rate (I_{sub}) under the condition that there are no traps. Obviously, the substantial ionization rate (I_{sub}) should be larger than the observed ionization rate (I_{obs}) under the condition existing traps (24% at 100 ppm). The binding energy of a hole around a negatively ionized acceptor ($Fe_2Cl_6^-$) (ΔE_A) can be calculated based on the equation (4.3.3).

$$I_{sub} = \exp(-\Delta E_A/2kT) \qquad (4.3.3.1)$$

As the minimum value of I_{sub}, we used 0.24 and ΔE_A of 0.072 eV was obtained.

Figs. 4.3.3.2(a) and (b) show the schematic energetic structures at the doping concentration of 100 and 500 ppm, respectively. Activation energies of hole trap both for 100 ppm (E_a = 0.18 eV) (Fig. 4.3.3.2(a)) and for 500 ppm (E_a = 0.37 eV) are larger than the binding energy of ionized acceptor (ΔE_A = 0.072 eV). For 100 ppm (Fig. 4.3.3.2(a)), since the concentration of hole trap (N_{trap}) is considerably lower compared to that of acceptor dopant, most of the created holes are free although a part of holes are captured. Thus, relatively high ionization rate (I_{obs}) of 24% was observed. For 500 ppm (Fig. 4.3.3.2(b)), since the concentration of hole trap (N_{trap}) becomes considerably higher compared to that of acceptor dopant, most of the created holes are captured by

hole traps. Thus, very low ionization rate (I_{obs}) of 3.6% was observed.

In order to estimate the trap concentration (N_{trap}), we assume I_{sub} = 1.0 for simplification. In this case, the number of dopant molecules ($N_{acceptor}$) and the number of holes created ($N_{acceptor} I_{sub}$) are the same. Since the value of E_a is significantly larger compared the thermal energy of room temperature, eventually all the traps are occupied by holes, i.e., all the traps are filled. In other words, the traps capture the free holes until all of them are filled. Under this condition, the number of traps (N_{trap}) equals to the number of trapped holes ($N_{trapped\ hole}$). Moreover, the sum of the number of free holes ($N_{free\ hole}$) and that of the trapped holes ($N_{trapped\ hole}$) equals that of all the holes created by doping ($N_{acceptor} I_{sub}$).

$$N_{acceptor} I_{sub} = N_{free\ hole} + N_{trapped\ hole} \qquad (4.3.3.2)$$

The number of free holes ($N_{free\ hole}$) equals to that of the number of free holes created by doping ($N_{acceptor} I_{obs}$) using the observed ionization rate (I_{obs}).

$$N_{acceptor} I_{obs} = N_{free\ hole} \qquad (4.3.3.3)$$

Since the acceptor molecule (iron chloride) has the structure of $Cl_2(Fe)Cl_2(Fe)Cl_2$ (Fe_2Cl_6), I_{obs} was calculated as the ratio of the number of free holes ($N_{free\ hole}$) created to that of the Fe_2Cl_6 molecule ($N_{acceptor}$).[17)] Here, we introduce the trap formation factor (F_{trap}), which can be expressed as the ratio of the number of traps to the number of dopant molecules.

$$F_{trap} = N_{trap} / N_{acceptor} \qquad (4.3.3.4)$$

At 100 ppm, $N_{acceptor}$, $N_{free\ hole}$, and I_{obs} are 1.1 x 10^{18} cm^{-3}, 2.6 x 10^{17} cm^{-3}, and 0.24. N_{trap} (= $N_{trapped\ hole}$) and F_{trap} are calculated to be 8.5 x 10^{17} cm^{-3} and 0.76. The dependences of N_{trap} and F_{trap} on the doping concentration are shown in Figs. 4.3.3.1(c) and (d), respectively. By increasing the doping concentration from 100 to 500 ppm, the number of traps (N_{trap}) increased from 8.5 x 10^{17} to 5.1 x 10^{18} cm^{-3} (Fig. 4.3.3.1(c)). Simultaneously, the trap formation ratio (F_{trap}) increased and reached near unity (94%) at 500 ppm (Fig. 4.3.3.1(d)). This suggests that the doping of one acceptor molecule creates one defect neighboring the doped molecule, which acts as trap. Therefore, we concluded that the dopant-induced defect formation caused the decrease of observed ionization rate (I_{obs}). As the dopant-induced defects, one can think many kinds of the disturbances of molecular stacking in rubrene single crystal, such as the dopant-induced vacancy, etc.

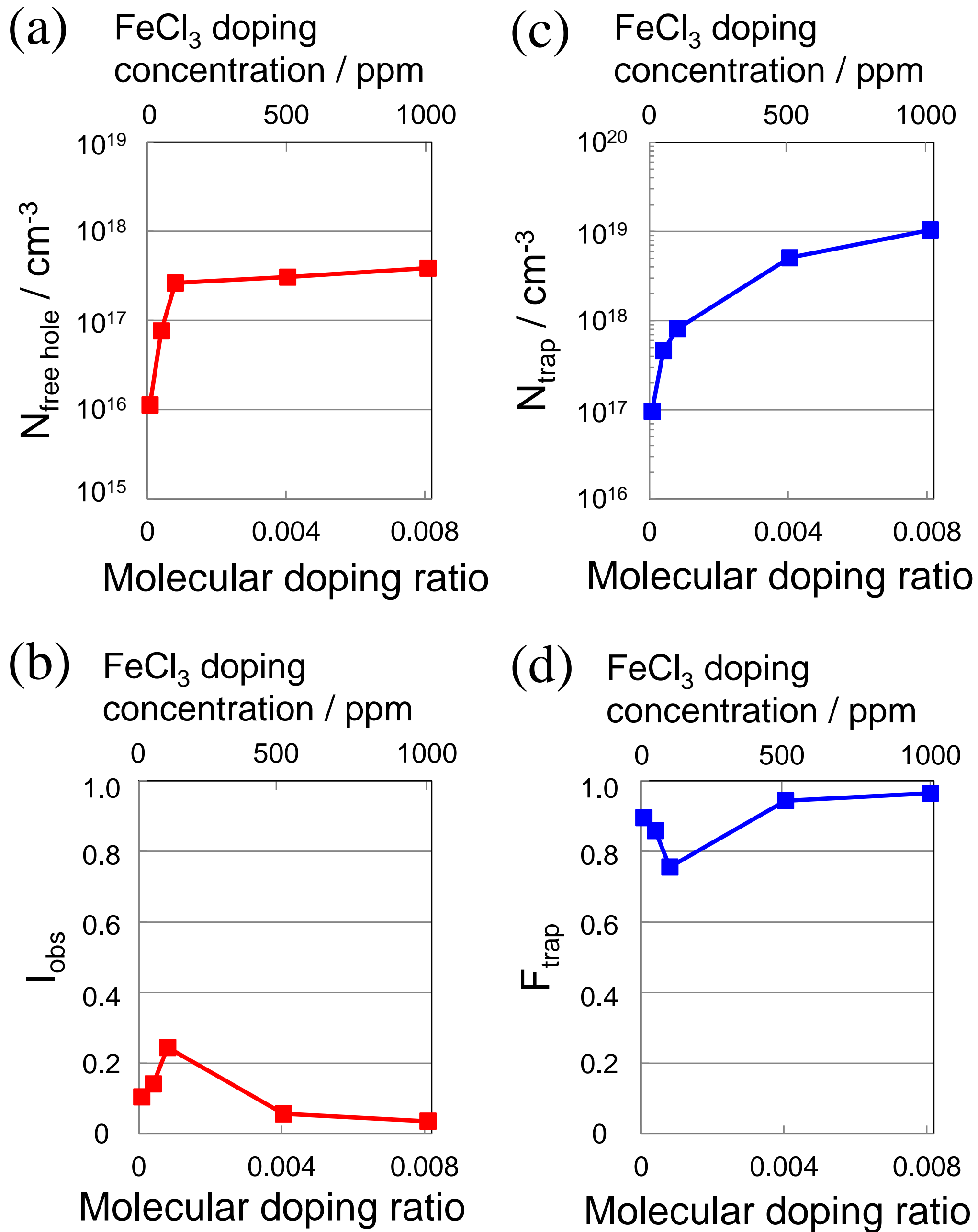

Fig. 4.3.3.1 Dependences of (a) the hole concentration ($N_{free\ hole}$), (b) the ionization rate (I_{obs}), (c) the trap concentration (N_{trap}), and (d) the trap formation factor (F_{trap}) on the molecular doping ratio (MR) and the $FeCl_3$ doping concentration.

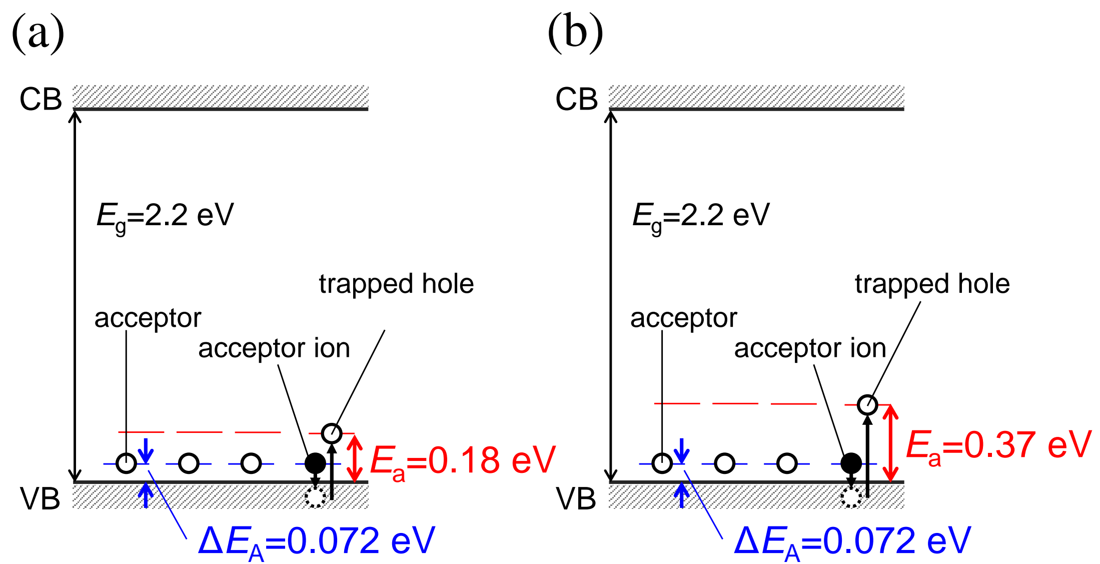

Fig. 4.3.3.2 Energetic structures at the doping concentration of (a) 100 and (b) 500 ppm.

4.4. Conclusion

In conclusion, the activation energy and the concentration of hole traps increased with increasing the acceptor dopant concentration for $FeCl_3$-doped rubrene single crystals. Formation of dopant-induced defects in the single crystal, which act as traps, revealed to suppress the observed ionization rate of dopant. The present result suggests that the fabrication process like annealing need to be introduced in order to remove the dopant-induced traps in organic single crystals to attain the maximum doping effects.

4.5. References

1) E. S. Henze, V. G. Lyssenko, J. Fischer, M. Tietze, R. Brueckner, T. Menke, K. Leo, and M. Riede, *Org. Electron.*, **15**, 563 (2014).

2) Y. Zhang, H. Zhou, J. Seifter, L. Ying, A. Mikhailovsky, A. J. Heerger, G. C. Bazan, and T. Q. Nguyen, *Adv. Mater.*, **25**, 7038 (2013).

3) Z. Shang, T. Heumueller, R. Prasanna, G. F. Burkhard, B. D. Naab, Z. Bao, M. D. McGehee, A. Salleo, *Adv. Energy Mater.*, 1601149 (2016).

4) M. Hiramoto, M. Kubo, Y. Shinmura, N. Ishiyama, T. Kaji, K. Sakai, T. Ohno, and M. Izaki, *Electronics.*, **3**, 351 (2014).

5) B. Lussem, M. L. Tietze, H. Kleemann, C. Hobach, J. W. Bartha, A. Zakhidov, and K. Leo, *Nat. Commun.*, **4**, 2775 (2013).

6) X. Liu, D. Kasemann, and K. Leo, *Appl. Phys. Lett.*, **106,** 103301 (2015).

7) B. D. Naab, S. Himmelberger, Y. Diao, K. Vandewal, P. Wei, B. Lussem, A. Salleo, and Z. Bao, *Adv. Mater.*, **25**, 4663 (2013).

8) S. Olthof, S. Mehraeen, S. K. Mohapatra, S. Barlow, V. Coropceanu, J. L. Bredas, S. R. Marder, and A. Kahn, *Phys. Rev. Lett.*, **109**, 176601 (2012).

9) M. L. Tietze, L. Burtone, M. Riede, B. Lussem, and K. Leo, *Phys. Rev. B.*, **86**, 035320 (2012).

10) M. L. Tietze, P. Pahner, K. Schmidt, K. Leo, and B. Lussem, *Adv. Funct. Mater.,* **25,** 2701 (2015).

11) C. Ohashi, Y. Shinmura, S. Watase, M. Izaki, H. Naito, S. Izawa, and M. Hiramoto, *Adv. Mater.,* revised re-submitted.

12) J. Takeya, M. Yamagishi, Y. Tominari, R. Hirahara, Y. Nakazawa, T. Nishikawa, T. Kawase, T. Shimoda and S. Ogawa, *Appl. Phys. Lett.*, **90,** 1021120 (2007).

13) R.A. Laudise, C. Kloc, P. G. Simpkins, and T. Siegrist, *J. Cryst. Growth.*, **187**, 449 (1998).

14) J. Endo, T. Matsumoto, and J. Kido, *Jpn. J. Appl. Phys.*, **41**, 358 (2002).

15) Y. Shinmura, Y. Yamashina, T. Kaji, and M. Hiramoto, *Appl. Phys. Lett.*, **105**, 183306 (2014).

16) X. Zeng, L. Wang, L. Duan, and Y. Qiu, *Crystal Growth & Design.,* **8**, 1617 (2008).

17) D. L. Price, M. L. Saboungi, and Y. S. Badyal, *Phys. Rev. B.*, **57**, 10496 (1998).

Chapter 5:

Effects of Impurity Doping in Simple $n^{+}p$-Homojunction Organic Photovoltaic Cells

"Effects of Doping at the ppm level in Simple $n^{+}p$-Homojunction Organic Photovoltaic Cells", Chika Ohashi, Yusuke Shinmura, Masayuki Kubo, and Masahiro Hiramoto, *Org. Electron.*, **27**, 151 (2015).

Abstract

The effects of doping at concentrations at the ppm level in organic photovoltaic cells were clarified using simple $n^{+}p$-homojunctions. With doping from 0 to 10 ppm, the fill factor increased due to the appearance of majority carriers. From 10 to 100 ppm, the photocurrent density increased due to an increase in the built-in potential, i.e., the formation of an $n^{+}p$-homojunction. The photocurrent was increased by a factor of 1.3 by directly doping the photoactive co-deposited layer with acceptor molecules at a concentration of 100 ppm.

5.1. Introduction

For small molecule type organic photovoltaic cells,[1-8] controlling the energy band structure by doping[7, 9-12] in order to create a built-in potential is a significant challenge, as it is for inorganic ones.[13] We think that co-deposited films should be doped since blended films consisting of organic semiconductor acting as a donor and that acting as an acceptor are used for efficient photocarrier generation in the present organic solar cells. We have previously reported on the complete *pn*-control of C_{60}:6T (α-sexithiophene)[14] and C_{60}:H_2Pc (metal-free phthalocyanine)[15,16] co-deposited films. Recently, we reported on the fabrication of p^+in^+-homojunction cells in C_{60}:6T co-deposited films by the use of doping only.[17] In those cells, the photocurrent is generated in the undoped co-deposited layer, i.e., the *i*-layer. However, we believe that direct doping of the photoactive co-deposited layer where the generation and transport of photocarriers occurs provides us with the potential to enhance the efficiency of these organic solar cells. Based on this consideration, we attempted to introduce a *pn*-homojunction into a C_{60}:6T co-deposited film. For the simplest cell, we adopted a n^+p-homojunction that has a one-sided abrupt junction (Fig. 5.1(a)).[18] The acceptor doping concentration in the *p*-layer was varied from the extremely low concentration of 1 ppm up to 1,000 ppm.

In this chapter, we report on the effects of doping at these levels in organic photovoltaic cells. An increase in photocurrent by a factor of 1.3 by directly doping the photoactive organic co-deposited layer with acceptor molecules at a concentration of 100 ppm was demonstrated.

5.2. Experimental

6T (Tokyo Chemical Industry) and C_{60} (Frontier Carbon, nanom purple TL) were purified by single-crystal sublimation.[7,19) $FeCl_3$ (Sigma-Aldrich, 99.99%)[20,21) and Cs_2CO_3 (Sigma-Aldrich, 99.995%)[7,15-17) were used for the acceptor and donor dopants, respectively. Fig. 5.1(a) shows the structure of the n^+p-homojunction cell. The cells were fabricated on indium tin oxide (ITO) substrates at 10^{-5} Pa in an oil-free vacuum evaporator (EpiTech Inc., ETVP-VG 100-SP) housed in a glove box (EpiTech Inc., 12ET12007). The evaporation rates of C_{60} and 6T were 0.1 and 0.01 nm s^{-1}, respectively. We chose the ratio of 10:1 (C_{60}:6T) because the optimum value of V_{oc} (0.8 V) was achieved with this ratio, larger than the value (0.4 V) achieved with the usual ratio of 1:1.[22) The thicknesses of the n^+- and p-layers were 10 and 100 nm, respectively. A 'Three component co-evaporation' technique was employed to dope the co-deposited films. The Cs_2CO_3 doping concentration for the n^+-layer was kept constant at 10,000 ppm. The $FeCl_3$ doping concentration for the p-layer was varied, i.e., 0, 1, 10, 100, and 1,000 ppm. Precise monitoring of the deposition rate using a quartz crystal microbalance equipped with a computer monitoring system (ULVAC, CRTM-9000G/Depoview) allowed us to introduce dopants down to the very low concentration of 100 ppm by volume, which corresponds to a $FeCl_3$ deposition rate of 1.1×10^{-5} nm s^{-1}. Doping concentrations of 10 and 1 ppm were realized by reducing the dopant evaporation rate using rotating disks with slits with aperture ratios of 1:10 and 1:100, respectively. The doping concentration of 1 ppm corresponds to a molecular ratio (MR) of 3.7×10^{-6}.

The current-voltage (J-V) characteristics were obtained under simulated solar light (AM 1.5G, 100 mWcm^{-2}). The position of the Fermi level (E_F) was determined

using a Kelvin probe (Riken-Keiki, FAC-1). Level bending in doped organic semiconductors can be measured by using photoelectron spectroscopy[23)] or by using Kelvin probes. We chose Kelvin probes to map the level bending profiles in the cells.[24)] The films and cells were prevented from exposure to air at all times during both fabrication and measurement.

5.3. Results and Discussion

5.3.1. Formation of n^+p-homojunction

Fig. 5.3.1(b) shows the energy band diagram of the C_{60}:6T co-deposited film. The bandgap in this film is determined by the conduction band of C_{60} (CB_{C60}) and the valence band of 6T (VB_{6T}). In order to fabricate an n^+-layer, heavy doping with Cs_2CO_3 (10,000 ppm) was performed. For the *p*-type layers formed on the n^+-layer, $FeCl_3$ doping concentrations of 10, 100, and 1,000 ppm caused E_F to shift towards VB_{6T} (5.50 eV) with more positive values of 5.01, 5.15, and 5.21 eV, respectively.[25)] These observations suggest that an n^+p-homojunction is expected to form as the $FeCl_3$ concentration is gradually increased.

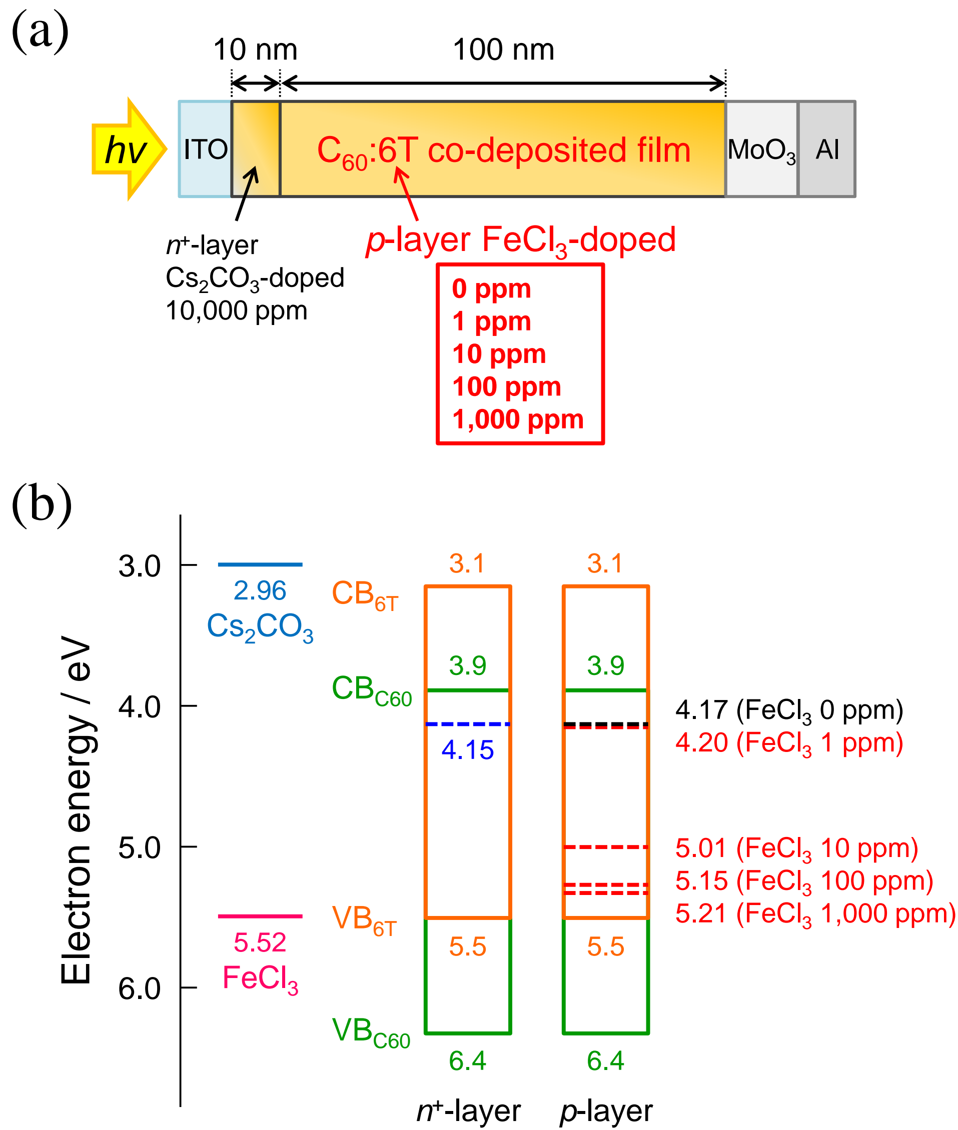

Fig. 5.3.1 (a) Structure of n^+p-homojunction cell with a one-sided abrupt junction. (b) Energy band diagram of n^+-C_{60}:6T co-deposited films doped with Cs_2CO_3 (10,000 ppm) and that of p-C_{60}:6T doped with $FeCl_3$ (1, 10, 100, 1,000 ppm) on an n^+-layer. The positions of E_F are shown by the broken lines. The work functions of Cs_2CO_3 and $FeCl_3$ are also shown.

5.3.2. Photovoltaic Characteristics

Fig. 5.3.2 shows the current-voltage characteristics for n^+p-homojunction cells with *p*-layer doping concentrations of 0, 1, 10, 100, and 1,000 ppm (Fig. 5.3.1(a)). The magnitude of the short-circuit photocurrent density (J_{sc}) increases progressively with the $FeCl_3$ doping of the photoactive C_{60}:6T layer as follows; 3.51 for 0 ppm (black solid curve), 4.02 for 10 ppm (orange solid curve), and 4.48 $mAcm^{-2}$ for 100 ppm (red solid curve). Simultaneously, there is a progressive increase in the magnitude of the forward current density (black, green, and red broken curves). That is, the cell resistance (R_s) decreases systematically with $FeCl_3$ doping and the minimum R_s of 2.35 Ωcm^2 is obtained at 100 ppm (see Fig. 5.3.4(b)). J_{sc} increases by a factor of 1.3 and the maximum efficiency of 1.51% is at 100 ppm. However J_{sc} decreases and R_s increases with a further increase in doping concentration to 1,000 ppm (blue curves). This confirms that the photocurrent can be increased significantly by directly doping the photoactive co-deposited layer with extremely low concentrations at the ppm level.

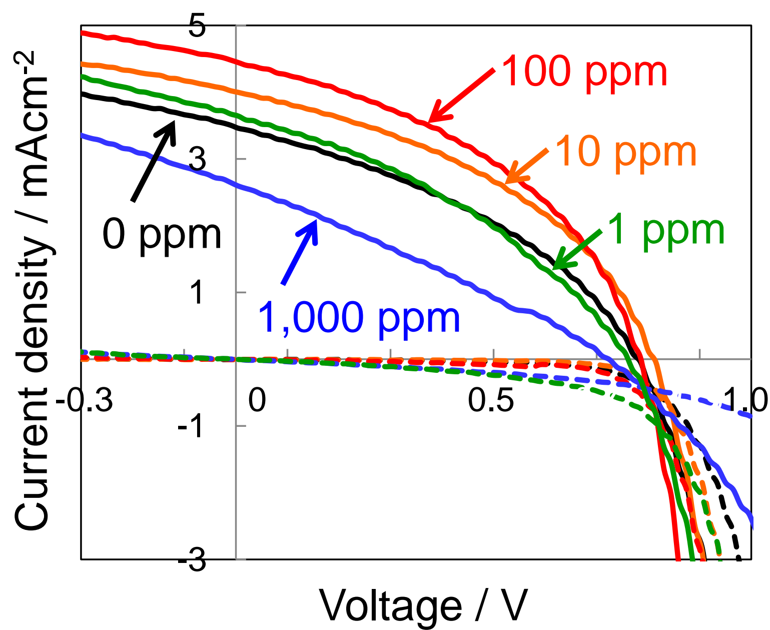

Fig. 5.3.2 Current-voltage characteristics for the n^+p-homojunction cells with p-layer doping concentrations of 0 (black curves), 1 (green curves), 10 (orange curves), 100 (red curves), and 1,000 ppm (blue curves). The photo and dark currents are shown by the solid and broken curves, respectively. The maximum efficiency was observed at 100 ppm [J_{sc}: 4.48 mA/cm^2, V_{oc}: 0.80 V, FF: 0.42, Efficiency: 1.51%].

5.3.3. Energy Structures

Level bending occurs only on the *p*-side of the n^+p-homojunction since the n^+-layer is heavily doped (10,000 ppm). Therefore, the width of the depletion layer (W_{dep}) formed in the *p*-type layer depends on the $FeCl_3$ doping concentration in the layer. Level bending in the *p*-type layer is accompanied by bending of the vacuum level since the Fermi levels (E_F) are aligned. Thus, we can measure the value of the work function, which is defined as the difference between the vacuum level and E_F, using a Kelvin probe, and we can measure the variation of this with the thickness of the film. Fig. 5.3.3(a) shows the dependence of the work function on the *p*-type layer thickness for various doping concentrations. In the cases of 0 (black dots) and 1 ppm (green dots), the observed work function has a constant value of 4.20 eV, which is the same as the Fermi level in the n^+-layer, i.e., no level bending was observed. This shows that layers with these doping levels act as intrinsic layers. The absence of any change in work function at the extremely low doping concentration of 1 ppm (Fig. 5.3(a), green dots) may be attributed to trap filling, i.e., doping induced carriers are captured by traps.[26)] In the cases of 10 (orange dots), 100 (red dots), and 1,000 ppm (blue dots), level bending was observed. This clearly shows that layers doped at these levels act as *p*-type layers. The width of the depletion layer (W_{dep}) and the built-in potential (V_{bi}) can be determined from the points (shown by arrows) at which the level bending ends. For example, W_{dep} = 50 nm and V_{bi} = 1.0 V at a doping concentration of 100 ppm. Moreover, the hole concentration (N_h) can be calculated using equation (5.3.3).

$$N_h = 2\varepsilon\varepsilon_0 V_{bi}/eW_{dep}^2 \qquad (5.3.3)$$

At 100 ppm, N_h was calculated to be 1.8 x 10^{17} cm^{-3}. The dependences of W_{dep},V_{bi}, and N_h on doping concentration are shown in Figs. 5.3.3(b), 5.3.4(c), and 5.3.4(d), respectively. The energy band diagrams of the n^+p-homojunction cells (Fig. 5.3.3(b)) can be found by turning the curves in Fig. 5.3.3(a) upside down.[27)]

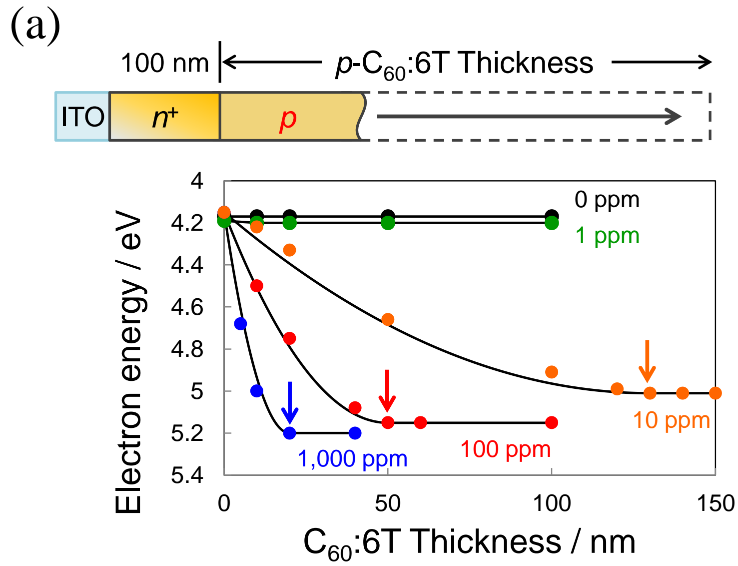

Fig. 5.3.3 (a) The dependence of the work function on the *p*-layer thickness for various doping concentrations. The *p*-layers were formed on n^+-layers.

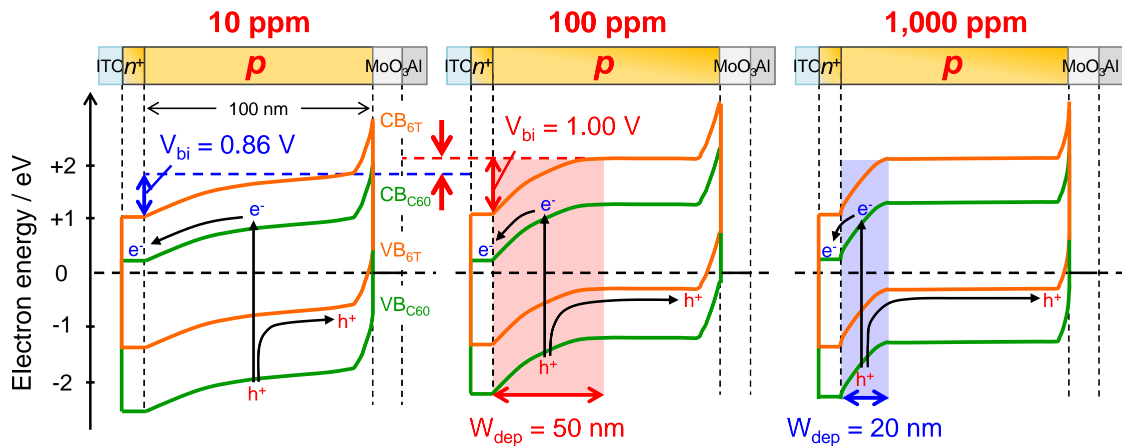

Fig. 5.3.3 (b) Energy band diagrams of n^+p-homojunction cells with 10, 100 and 1,000 ppm $FeCl_3$-doped *p*-layers.

5.3.4. Doping Concentration Dependence of Photovoltaic Characteristics

Fig. 5.3.4(a) shows the dependences of J_{sc} and the fill factor (FF) on doping concentration. The doping effects can be divided into three regions. From 0 to 10 ppm, both FF and J_{sc} increase rapidly. From 10 to 100 ppm, J_{sc} still increases while FF maintains a constant value. From 100 to 1,000 ppm, both J_{sc} and FF decrease.

Fig. 5.3.4(b) shows the dependences of the fill factor (FF) and the cell resistance (R_s) on doping concentration from 0 to 100 ppm. Clearly, R_s decreases and FF increases from 0 to 10 ppm. Once acceptor doping is performed, holes and electrons inevitably act as majority and minority carriers, respectively. At 10 ppm, the number (N_h) of majority carriers (holes) is 2.3 x 10^{16} cm^{-3}. Thus, we conclude that the increase in FF at 10 ppm doping is due to the appearance of majority carriers in the *p*-layer.

Fig. 5.3.4(c) shows the dependences of J_{sc} and the built-in potential (V_{bi}) on doping concentration from 0 to 1,000 ppm. Clearly, there is a close relationship between J_{sc} and V_{bi}. In particular, there are simultaneous increases in J_{sc} and V_{bi} at the relatively low doping concentrations of 10 and 100 ppm. The increase in V_{bi} is also shown in the energy band diagrams for 10 and 100 ppm in Fig. 5.3.3(b) and one can see that J_{sc} increases with increasing V_{bi}. Based on these considerations, we conclude that the increase in J_{sc} is due to the increase in V_{bi}, that is, the formation of an n^+p-homojunction.

From 100 to 1,000 ppm, both FF and J_{sc} decrease (Fig. 5.3.4(a)). Simultaneously, R_s increases considerably from 2.35 to 50 Ωcm^2. The mobility of the majority carriers (holes), μ_h, can be calculated from equation (5.3.4).

$$\sigma_h = eN_h\mu_h \qquad (5.3.4)$$

Here, N_h and σ_h are the hole concentration, which is obtained by Kelvin band mapping (Fig. 5.3.3(a)), and the hole conductivity, which is obtained from the cell resistance ($\sigma_h = LR_s^{-1}$; L: cell thickness) determined from the forward dark current for the n^+p-homojunction cells (n^+-C_{60}:6T/p-C_{60}:6T/MoO_3) (Fig. 5.3.2, broken curves), respectively. The mobility, μ_h, was calculated to be 1.5 x 10^{-4} and 1.1 x 10^{-6} $cm^2V^{-1}s^{-1}$ at 100 and 1,000 ppm, respectively.[28] Fig. 5.3.4(d) shows the dependences of the hole concentration (N_h) and the hole mobility (μ_h) on doping concentration from 10 to 1,000 ppm. μ_h decreases at concentrations from 100 to 1,000 ppm (blue solid curve). We think that this is due to the disturbance of the hopping transport of holes by negatively ionized and neutral acceptor dopants although there still remains the possibility that it may be due to a nanoscopic change in morphology. Harada et al.[29, 30] reported a decrease in mobility for higher doping concentrations of C_{60} films. The decrease in μ_h dominates the cell resistance (R_s) in spite of the increase in N_h, causing R_s to increase and, as a result, FF to decrease. Thus, we conclude that the decrease in FF is due to the decrease in hole mobility (μ_h). As shown in Fig. 5.3.3(b), the width of the depletion layer (W_{dep}) reduces from 50 to 20 nm as the doping concentration is increased from 100 to 1,000 ppm. As a result, we conclude that the decrease in J_{sc} is due to the decrease in W_{dep}, which is the width of the photoactive layer.[31]

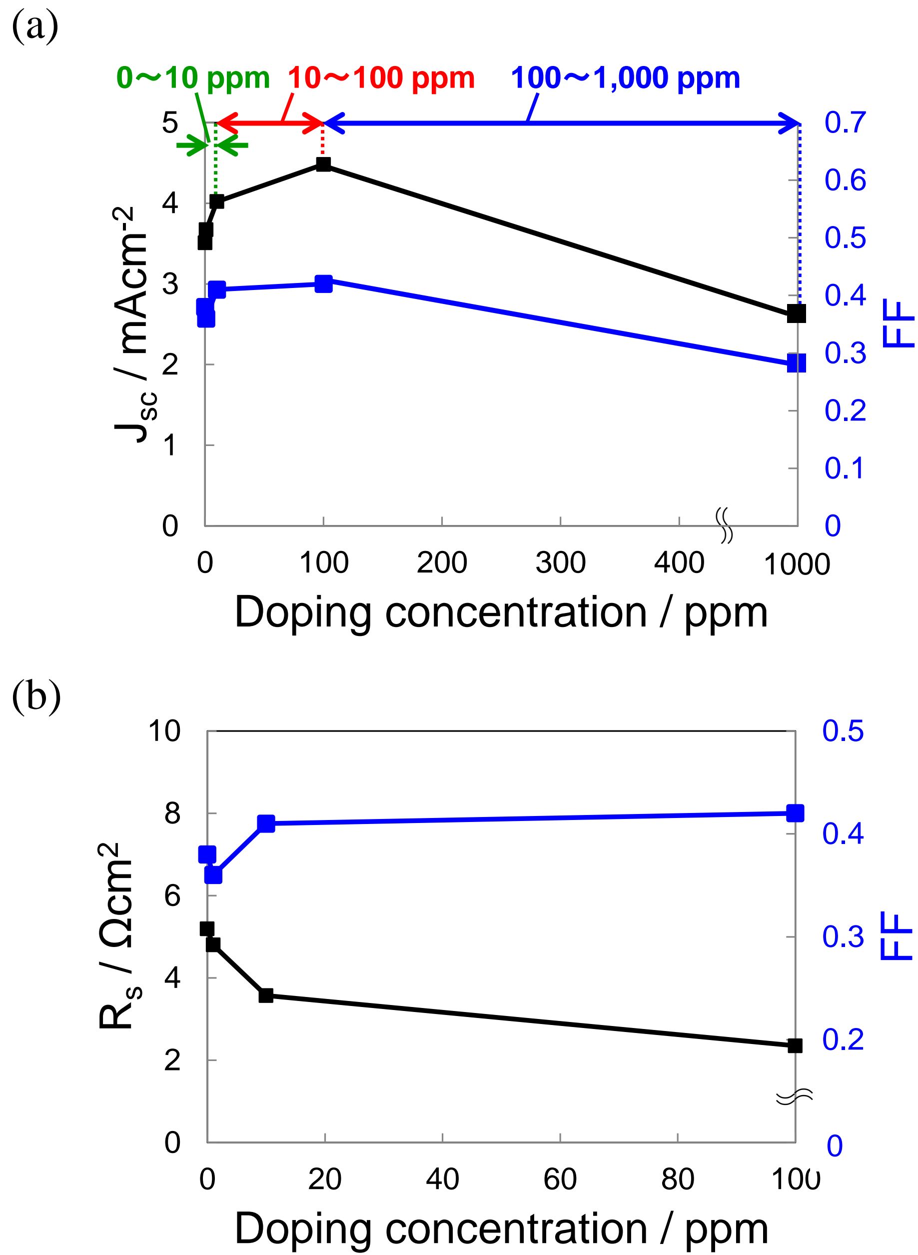

Fig. 5.3.4 (a) Dependences of J_{sc} and the fill factor (FF) on doping concentration. (b) Dependences of the fill factor (FF) and the cell resistance (R_s) on doping concentration.

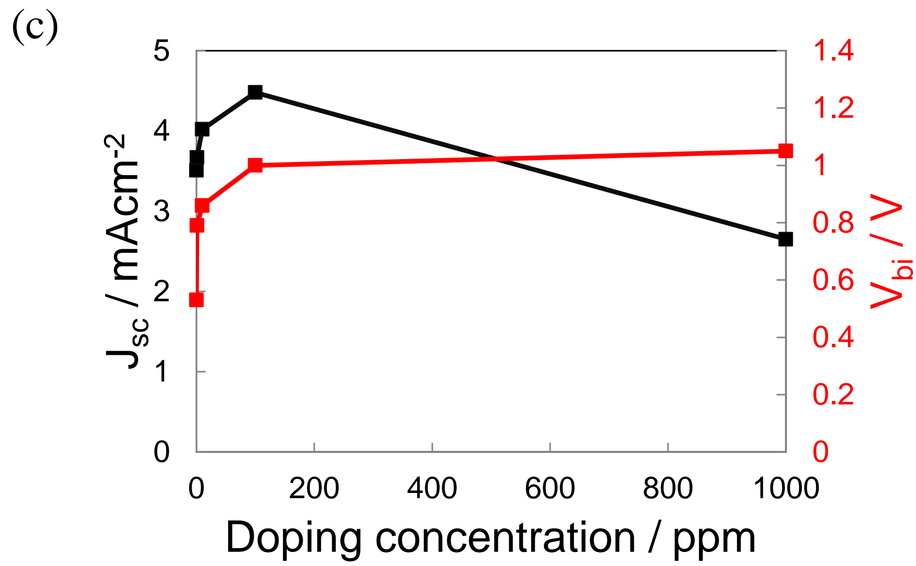

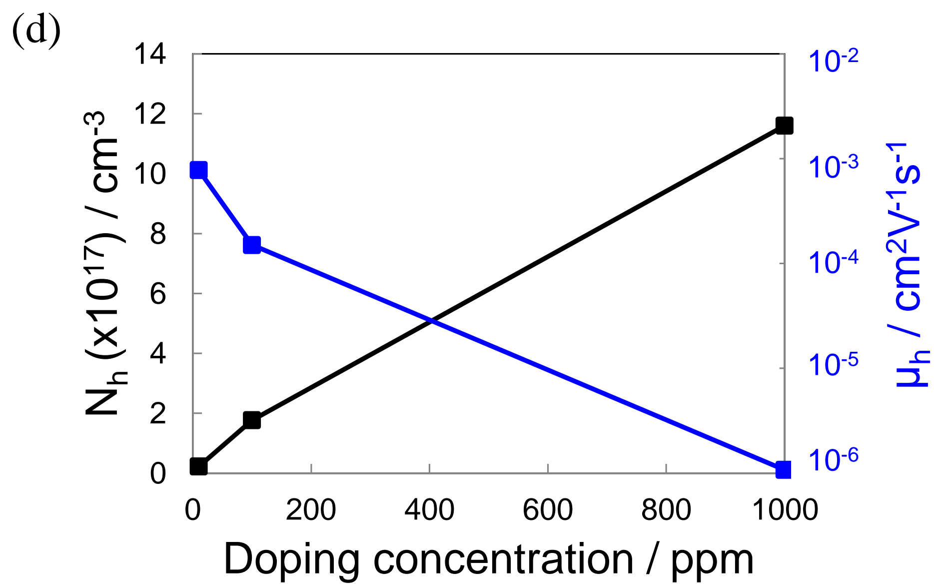

Fig. 5.3.4 (c) Dependences of J_{sc} and the built-in potential (V_{bi}) on doping concentration. (d) Dependences of the hole concentration (N_h) and hole mobility (μ_h) on doping concentration.

5.4. Conclusion

In this chapter, by directly doping a photoactive co-deposited layer at the ppm level, we were able to increase both the photocurrent and the fill factor. The increases in FF and J_{sc} from 0 to 100 ppm are due to the decrease in R_s following the introduction of majority carriers and the increase in V_{bi}, respectively. The decreases in FF and J_{sc} from 100 to 1,000 ppm doping are caused by the decrease in mobility of the majority carriers as a result of the disturbance of hopping transport by dopant molecules and by the decrease in W_{dep}, respectively. The most important technical significance of the doping is the intentional design of built-in potentials in the cells. We believe that a new design concept that includes the doping technology needs to be developed in order to realize a high-performance cell.

5.5. References

1) Organic photovoltaics, Mechanisms, Materials and Devices, edited by S. S. Sun and N. S. Sariciftci, published by CRC Press, New York, March (2005).
2) H. Spanggaard and F. C. Krebs, *Sol. Energy Mater. Sol. Cells*, **83**, 125 (2004).
3) H. Hoppe and N. S. Sariciftci, *J. Mater. Res*., **19**, 1924 (2004).
4) Stability and Degradation of Organic and Polymer Solar Cells, edited by F. C. Krebs, published by John Wiley & Sons, Ltd (2012).
5) C. W. Tang, *Appl. Phys. Lett.*, **48**, 183 (1986).
6) M. Hiramoto, H. Fujiwara, and M. Yokoyama, *Appl. Phys. Lett.,* **58**, 1062 (1991).
7) M. Hiramoto, M. Kubo, Y. Shinmura, N. Ishiyama, T. Kaji, K. Sakai, T. Ohno, and M. Izaki, *Electronics.*, **3**, 351 (2014).
8) T. Kaji, M. Zhang, S. Nakao, K. Iketaki, K. Yokoyama, C. W. Tang, and M. Hiramoto, *Adv. Mater.*, **23**, 3320 (2011).
9) K. Walzer, B. Maennig, M. Pfeiffer, and K. Leo, *Chem. Rev.*, **107**, 1233 (2007).
10) G. Li, R. Zhu, and Y. Yang, *Nature Photon*., **6**, 153 (2012).
11) M. Hiramoto, K. Ihara, and M. Yokoyama, *Jpn. J. Appl. Phys*., **34**, 3803 (1995).
12) S. Hamwi, T. Riedl, and W. Kowalsky, *Appl. Phys. Lett*., **99**, 053301 (2011).
13) W. E. Spear and P. E. Lecomber, *Solid State Commun.*, **17**, 1193 (1975).
14) N. Ishiyama, M. Kubo, T. Kaji, and M. Hiramoto, *Appl. Phys. Lett.*, **99**, 133301 (2011).
15) M. Kubo, Y. Shinmura, N. Ishiyama, T. Kaji, and M. Hiramoto, *Mol. Cryst. Liq. Cryst.*, **581**, 13 (2013).
16) M. Kubo, T. Kaji, and M. Hiramoto, *Appl. Phys. Lett.*, **103**, 263303 (2013).
17) N. Ishiyama, M. Kubo, T. Kaji, and M. Hiramoto, *Org. Electron*., **14**, 1793 (2013).

18) Physics of Semiconductor Devices, S. M. Sze, published by WILEY-INTERSCEINCE, Chapter 3 (1969).

19) R.A. Laudise, Ch. Kloc, P.G. Simpkins, T. Siegrist, *J. Cryst. Growth.*, **187**, 449 (1998).

20) J. Endo, T. Matsumoto, and J. Kido, *Jpn. J. Appl. Phys.*, **41**, 358 (2002).

21) Y. Shinmura, Y. Yamashina, T. Kaji, and M. Hiramoto, *Appl. Phys. Lett.*, **105**, 183306 (2014).

22) J. Sakai, T. Taima, and K. Satio, *Organic Electronics*, **9**, 582 (2008).

23) J. Blochwitz, T. Fritz, M. Pfeiffer, K. Leo, D.M. Alloway, P.A. Lee, and N.R. Armstrong, *Org. Electron.*, **2**, 97 (2001).

24) Y. Shinmura, T. Yoshioka, T. Kaji, and M. Hiramoto, *Appl. Phys Express.*, **7**, 071601 (2014).

25) Undoped (0 ppm) and the extremely low doping concentration of 1 ppm showed no level bending (Fig. 3(a)). This means that with extremely low doping concentrations of less than 1 ppm there is no possibility of the bands bending and the observed E_Fs for 0 and 1 ppm were determined by the E_F of the n^+-layer.

26) M. Tietze, P. Pahner, K. Schmidt, K. Leo, and B. Lussem, *Adv. Funct. Mater.,* **25** 2701 (2015).

27) The energy band diagrams of the back contacts, which consist of the ohmic contacts at the interfaces between p-C_{60}:6T and MoO_3, were measured by Kelvin band mapping and are illustrated in Fig. 3(b).

28) R_s can be obtained from the resistance of the hole-only device configuration (p^+-C_{60}:6T/p-C_{60}:6T/p^+-C_{60}:6T). At 100 ppm, the values of R_s and μ_h were determined to be 3.2 Ωcm^2 and 1.1 x 10^{-4} $cm^2V^{-1}s^{-1}$, respectively. These values

almost concur with those obtained from the n^+p-homojunction cell.

29) K. Harada, F. Li, B. Maennig, M. Pfeiffer, and K. Leo, *Appl. Phys. Lett.*, **91**, 092118 (2007).

30) K. Harada, M. Sumino, C. Adachi, S. Tanaka, and K. Miyazaki, *Appl. Phys. Lett.*, **96**, 253304 (2010).

31) By analyzing the shapes of the action spectra, the photoactive layer thicknesses were suggested to be about 60 and 20 nm at the doping concentrations of 100 and 1,000 ppm, respectively, which are close to the values of the thicknesses of the space charge layers of 50 and 20 nm, respectively. We think that the diffusion length of minority carriers outside the space charge layer is less than 10 nm although the excitons dissociate in the whole of the co-deposited film.

Chapter 6:

Summary and Future Prospects

In this chapter, the conclusion to this thesis and prospects for the future are presented. The following summarizes the achievements made in this work.

1) ppm-level doped homoepitaxial rubrene single crystal was successfully fabricated by means of an ultra-slow co-deposition technique with a deposition rate as low as 10^{-9} nm s^{-1}.
2) Hall effect in doped rubrene single crystal was systematically measured for the first time.
3) A relatively high doping efficiency, reaching 24%, and a decrease in μ_H due to scattering effects owing to lattice disturbances were observed in the doped rubrene single crystal.
4) Enhancement of the photovoltaic performance with an extremely low doping concentration of 1 ppm was confirmed.

The author believes that the work described in this thesis will lead to the following future developments.

1) The detailed doping mechanism in doped organic single crystals, such as the state of the dopants, the doping induced lattice disturbances, such as vacancies, interstitials, etc., will be clarified.
2) New types of organic device using doped organic single crystals will be fabricated.

List of Publications

All papers are included in this doctoral thesis.

1) Effects of Doping at the ppm level in Simple n^+p-Homojunction Organic Photovoltaic Cells

   Chika Ohashi, Yusuke Shinmura, Masayuki Kubo, and Masahiro Hiramoto

   Org. Electron., **27**, 151 (2015).

2) Hall effects in Doped Organic Single Crystals

   Chika Ohashi, Yusuke Shinmura, Seiji Watase, Masanobu Izaki, Hiroyoshi Naito, Seiichiro Izawa, and Masahiro Hiramoto

   Adv. Mater., DOI: 10.1002/adma.201605619.

3) Field-Effect Mobility of Doped Organic Single Crystals

   Chika Ohashi, Seiichiro Izawa, Yusuke Shinmura, and Masahiro Hiramoto

   in preparation.

Poster Presentations in International Conferences

1) 100 ppm Doping Induced Photocurrent Enhancement in Photoactive Organic Co-deposited Layer

   Chika Ohashi, Yusuke Shinmura, Masayuki Kubo, and Masahiro Hiramoto

   2015 E-MRS Spring Meeting,

   Lille Grand Palais, Lille, France, 11th May 2015.

2) ppm-Doping Effects in the Simplest n^+p-Homojunction Organic Photovoltaic Cells

   Chika Ohashi, Yusuke Shinmura, Masayuki Kubo, and Masahiro Hiramoto

   2015 MRS Fall Meeting & Exhibit,

   Hynes Convention Center, Boston, USA, 30th November 2015.

3) ppm-Doping Effects in the Simplest n^+p-Homojunction Organic Photovoltaic Cells

   Chika Ohashi, Yusuke Shinmura, Masayuki Kubo, and Masahiro Hiramoto

   The 3rd Workshop on Physics in Organic Optoelectronics,

   Institute for Molecular Science, Aichi, Japan, 10th December 2015.

4) Effects of Doping at the ppm level in Simple n^+p-Homojunction Organic Photovoltaic Cells

   Chika Ohashi, Yusuke Shinmura, Masayuki Kubo, and Masahiro Hiramoto

   KJF-ICOMEP 2016,

   ACROS Fukuoka, Fukuoka, Japan, 5th September 2016

Oral Presentations in Conferences (in Japanese)

1) 100 ppm Doping Induced Photocurrent Enhancement in Photoactive Organic Co-deposited Layer

   <u>Chika Ohashi</u>, Yusuke Shinmura, Masayuki Kubo, and Masahiro Hiramoto

   The 62th Spring Meeting 2015 (The Japan Society of Applied Physics),

   Tokai University, Kanagawa, 11th March 2015.

2) Hall effects for doped homoepitaxial rubrene single crystals

   <u>Chika Ohashi</u>, Yusuke Shinmura, Seiji Watase, Masanobu Izaki, Hiroyoshi Naito, and Masahiro Hiramoto

   The 63th Spring Meeting 2016 (The Japan Society of Applied Physics),

   Tokyo Institute of Technology, Tokyo, 21th March 2016.

3) Doping efficiency for rubrene homoepitaxial single crystal and amorphous film

   <u>Chika Ohashi</u>, Yusuke Shinmura, Seiichiro Izawa, and Masahiro Hiramoto

   The 77th Autumn Meeting 2016 (The Japan Society of Applied Physics),

   Toki Messe, Niigata, 13th September 2016.

Poster Presentations in Conferences (in Japanese)

1) Doping Effect to Co-deposited Active Layer in Organic Photovoltaic Cells

   Chika Ohashi, Yusuke Shinmura, Toshihiko Kaji, and Masahiro Hiramoto

   The 75th Autumn Meeting 2014 (The Japan Society of Applied Physics),

   Hokkaido University, Hokkaido, 17th September 2014.

2) ppm-Doping Effects in the Simplest n^+p-Homojunction Organic Photovoltaic Cells

   Chika Ohashi, Yusuke Shinmura, Masayuki Kubo, and Masahiro Hiramoto

   NAIST Workshop on Study of Organic Solar Cells,

   NAIST, Nara, 28th November 2015.

Acknowledgements

I would like to thank Professor Masahiro Hiramoto of the Graduate University for Advanced Studies (SOKENDAI), Institute for Molecular Science (IMS), for significant guidance during this thesis.

I would also like to thank Prof. Satoshi Kera, Prof. Hiroshi Yamamoto, Associate Prof. Toshiyasu Suzuki of IMS and Prof. Hiroyoshi Naito of Osaka Prefecture University, for their reviews of this thesis.

I'm thankful to Prof. Masanobu Izaki of Toyohashi University of Technology, Associate Prof. Toshihiko Kaji of Tokyo University of Agriculture and Technology, Assistance Prof. Seiichiro Izawa of IMS for helpful discussions.

I'm also thankful to the co-authors of the papers and all the members of Professor Hiramoto group; Dr. Yusuke Shinmura, Dr. Masayuki Kubo, Dr. Norihiro Ishiyama, Mr. Mitsuru Kikuchi, Mr. Yohei Yamashina, Mr. Mikimasa Katayama, Mr. Masaki Hirota, Mr. Naoto Shintaku, Ms. Thidarat Kunawong, Ms. Hidemi Sugihara, and Ms. Megumi Kobayashi. I thank all these for much advice and assistance.

I appreciate the financial support from the Japanese Society for the Promotion of Science (JSPS) through their Research Fellowships for Young Scientists program, the Japanese Science and Technology Agency (JST) for their Core Research for Evolutional and Technology (CREST) program and the New Energy and Industrial Technology Development Organization (NEDO).

Finally, I would like to thank my parents and family for supporting and encouraging me and I am deeply grateful for their support and help during my time as a Ph.D. student.

Chika Ohashi